

Purdue University
Purdue e-Pubs

Department of Electrical and Computer
Engineering Technical Reports

Department of Electrical and Computer
Engineering

7-12-2016

Fault Detection in Surface PMSM with Applications to Heavy Hybrid Vehicles

Scott Johnson

Electrical and Computer Engineering, Purdue University, johns924@purdue.edu

Richard T. Meyer

Western Michigan University, richard.meyer@wmich.edu

Raymond A. DeCarlo

Purdue University, decarlo@purdue.edu

Steve Pekarek

Purdue University, spekarek@purdue.edu

Follow this and additional works at: <http://docs.lib.purdue.edu/ecetr>

Johnson, Scott; Meyer, Richard T.; DeCarlo, Raymond A.; and Pekarek, Steve, "Fault Detection in Surface PMSM with Applications to Heavy Hybrid Vehicles" (2016). *Department of Electrical and Computer Engineering Technical Reports*. Paper 472.
<http://docs.lib.purdue.edu/ecetr/472>

This document has been made available through Purdue e-Pubs, a service of the Purdue University Libraries. Please contact epubs@purdue.edu for additional information.

Fault Detection in Surface PMSM with Applications to Heavy Hybrid Vehicles

Scott Johnson, Richard T. Meyer, Raymond A. DeCarlo, Steve Pekarek

July 12, 2016

Abstract

This report explores detecting inter-turn short circuit (ITSC) faults in surface permanent magnet synchronous machines (SPMSM). ITSC faults are caused by electrical insulation failures in the stator windings and can lead to shorts to ground and even fires. This report proposes methods for detecting these faults using a moving horizon observer (MHO) to reduce the chance of electrical shocks and fires. Specifically, this report constructs a MHO for ITSC fault detection in SPMSM.

ITSC fault tolerant control is investigated for a 2004 Toyota Prius hybrid vehicle having a traction SPMSM. Once the supervisory-level powertrain power flow control becomes aware of the presence of a fault and its degree from the MHO, the control (i) reduces the maximum possible vehicle speed to ensure SPMSM thermal constraints are not violated and (ii) switches to a traction motor input-output power efficiency appropriate for the degree of fault. These steps are taken during a fault rather than shutting down the traction motor to provide a “limp home” capability. The traction motor cannot simply be turned off because its rotation is not independent of drive wheel rotation. The control is demonstrated by simulating the Prius over a 40 s drive velocity profile with faults levels of 0.5%, 1%, 2%, and 5% detected at the midpoint of the profile. For comparison, the Prius is also simulated without a traction motor fault. Results show that the control reduced vehicle velocity upon detection of a fault to appropriate safe values. Further, the challenges of ITSC fault tolerant control for heavy hybrid vehicles are examined.

This work is partially supported by the Department of Energy, Award No. DE-EE0005568.

The authors would like to acknowledge the support of Greg Shaver and the Hoosier Heavy Hybrid Center of Excellence.

S. Johnson, R. DeCarlo, and S. Pekarek are with the Department of Electrical and Computer Engineering at Purdue University, 610 Purdue Mall, West Lafayette, IN 47907 (email: johns924@purdue.edu, decarlo@ecn.purdue.edu, spekarek@purdue.edu).

R. Meyer is with the Department of Mechanical and Aerospace Engineering at Western Michigan University, 1903 West Michigan Avenue, Kalamazoo, MI 49008 (email: richard.meyer@purdue.edu).

I. INTRODUCTION AND MOTIVATION

A. *Faults in a Permanent Magnet Synchronous Machine*

The widespread need for conservation of diminishing fossil fuels, the economic benefits of more efficient fuel usage, and reduced environmental impact has motivated the development of heavy hybrid and heavy electric vehicles such as the Deere 644k Hybrid Wheel Loader and the Caterpillar D7E Dozer. An electric motor often utilized in these vehicles is the Permanent Magnet Synchronous Machine (PMSM). PMSMs are popular in such vehicles because of their higher torque density compared to induction and switched reluctance electric motors [1]. There are two types of the PMSM, interior mount and surface mount. The surface mount PMSM, denoted SPMSM herein, has permanent magnets attached to the surface of the rotor. Typically, these magnets are made of rare-earth materials such as neodymium iron boron (NeFeB) which produce a relatively high maximum energy product BH for a given size and weight. Only the SPMSM is considered in this report.

The stator of a SPMSM contains windings associated with each phase of a 3-phase machine. See Figures 1 and 2. These windings are spaced according to a particular geometric design. The windings associated with the same electrical phase can be in close proximity within winding bundles on the stator. Due to high temperature heating from I^2R losses in the windings, vibrations, and materials aging, the stator coils are prone to shorts. According to SKF Electric Motor Condition Monitoring Company, 30% of motor failures are due to stator winding failures [2]. The aforementioned bundles are common places for shorts, and are termed inter-turn short-circuit (ITSC) faults. A General Electric study, cited in [2], reports that 80% of motor failures begin as turn-to-turn insulation failures, i.e. ITSC faults. This is partly because machine vibrations can cause the bundles to rub against a sharp edge of the stator often causing an insulation failure in two of the bundle wires resulting in an ITSC fault. A “tooth” of the stator (around which a coil is wound) is another possible location for an ITSC fault. Here, two insulation failures on wires on the same tooth can lead to the an ITSC fault using the metal in the tooth to complete the short circuit.

When an ITSC fault occurs in the stator windings, a closed loop of wire is effectively created within the windings of the phase containing the fault. This closed loop of wire is coupled magnetically to the changing magnetic fields created by the remaining healthy phase windings and the rotating magnets. The

magnetic flux through the closed loop of wire creates an eddy current which circulates within the wire. If left undetected, the ITSC fault can lead to further insulation failures risking a short to ground and potentially a fire. A short-to-ground event can cause damage to the electric machine and other electrical equipment.

B. Report Objectives

This report investigates the fault-modeling and fault-detection of a 3-phase SPMSM using an observer strategy. The (ITSC fault) observer must detect an ITSC fault before such can cause unsafe operating conditions. According to the recent survey paper [3], diverse researchers have considered several methods for detecting ITSC faults in a PMSM. One such technique, termed motor current signature analysis (MCSA), detects changes in the frequency content of the current and voltage waveforms using filtering techniques based upon Fast Fourier Transform and Discrete Wavelet Transform algorithms [2]–[4]. Other proposed techniques for fault detection include finite element models and artificial intelligence algorithms. However, these techniques require considerable machine-specific tuning and analysis [3].

In order to avoid considerable machine-specific tuning and analysis, the observer structure utilized herein builds on an analytical model (having known parameters) of the stator windings as a function of the degree of fault. As with all observers, sensor measurements of the system inputs and outputs drive an algorithm (dependent on the analytic model) that produces state estimates, fault level estimates, and associated output estimates over some interval of time. The error between the estimated outputs and the actual sensor driven outputs determines, according to some metric, whether or not an ITSC fault has occurred as well as its severity. Finally, in order to determine safe or unsafe continued motor operation due to thermal heating maximums, the observer herein additionally estimates the eddy loop current denoted i_{fs} whose magnitude can cause excessive heating. Of course, stator winding faults are not restricted to ITSC faults and include shorts to ground and open circuit faults. Although these faults do occur in practice, the focus of this report is ITSC faults which cause the majority of motor failures [2].

Building around the moving horizon observer (MHO) of [5], we re-pose the observer problem as a dynamic model-based optimization problem. Conditions for the observer to converge are given therein. Further details are given in Section IV.

Another objective of this research is to develop fault mitigation controller strategies that allow the hybrid vehicle (of which the SPMSM is an integral part) to continue to function albeit at a substantially reduced operational level. In the case of a large earth mover, this might allow the vehicle to limp back to its truck hauler for delivery to the service center. In the case of a small hybrid vehicle like a Toyota Prius, the vehicle could drive slowly to a service center or other destination.

A so-called supervisory level controller along the lines set forth in [6], [7], and [8] coordinates vehicle control by determining optimized power flows to the individual subsystems. For example, for a diverse set of situations, the supervisory level controller would determine how best to utilize the electric motor vs. the internal combustion engine (ICE) or recover energy with regenerative braking. For efficient and feasible optimization strategies, the supervisory level models are power flow based and utilize efficiency maps pertinent to the individual subsystems. In the case of the SPMSM, such an efficiency map depends on whether or not the motor has a fault as well as on the degree of fault.

When faults in the windings exceed a level of 10-20% or more, safety may dictate a shut down of the vehicle. The permanent magnets of the traction PMSM (one of two PMSM in the powertrain) are attached to the powertrain output shaft, i.e. the output shaft is the PMSM rotor; thus as long as the shaft turns, the permanent magnets will cause an eddy current to flow in the shorted stator coils. As will be seen, such eddy currents can be extremely large causing high temperatures in the motor coils that exceed the maximum allowable operating temperature and thus unsafe operation. For fault levels at 10-20% or below, it may be possible to limp the motor and vehicle along.

In summary, our fault tolerant controller at the supervisory level uses the MHO ITSC fault observer as a component of the SPMSM which determines the “mode” or fault level of its operation. The supervisory controller can then determine a possible fault tolerant or fault mitigating power flow control strategy. In addition, the observer estimates the eddy loop current i_{fs} in order to determine approximate thermal losses so as to determine safe or unsafe operation when a fault has occurred.

C. Recasting the Observer Problem in a Switched System Observability Setting

It is convenient at the supervisory level to consider a finite set of possible fault levels between 0 (non-fault case) and 10-20%. In the case of the Prius, we consider a maximum fault level of 10% based

on experimental evidence for reasonable vehicle operation. Each different fault level induces a different linear state model of the SPMSM. As such, each of the fault levels can be viewed as a mode associated with a specific linear dynamical state model. The ability to distinguish and identify the modes and mode switching times then reduces to the so-called switched observability problem discussed in the subsection below. The details of the SPMSM stator model with and without fault are developed in Sections II and III. However, in general, for each degree of fault σ the state model has the form

$$\begin{aligned} E(\sigma)\dot{x} &= A(\sigma)x + B(\sigma)u \\ y &= C(\sigma)x + D(\sigma)u, \end{aligned} \tag{1}$$

where $x \in \mathbb{R}^n$ will represent the stator currents and eddy current, $u \in \mathbb{R}^m$ represents the voltage inputs and back electromotive forces, $y \in \mathbb{R}^p$ represents the current and voltage measurements, $E(\sigma) \in \mathbb{R}^{n \times n}$ is an inductance matrix, and $A(\sigma)$, $B(\sigma)$, $C(\sigma)$, and $D(\sigma)$ are real matrices of appropriate dimension. Equation 1 is valid for every degree of fault $\sigma \in [0, 1]$, i.e. the matrices change as a function of σ . We remark again that for each such fault level, mode, there is an associated efficiency map that must be used by the supervisory level controller to determine reasonable operation of the vehicle and how best to limp the vehicle along if the fault level is sufficiently low.

Determining feasibility of reconstructing the degree of fault σ requires proving distinguishability of each LTI system associated with the degrees of fault $\sigma_1 \neq \sigma_2 \in [0, 1]$. However, we shall see that distinguishability between one pair of degrees of fault (σ_1, σ_2) will imply that almost all degrees of fault are distinguishable. This allows for the application of the switched linear system observability results ([9], [10]) to the ITSC fault detection problem. We now review the relevant switched system observability results.

D. Review of Switched System Observability Results

The results surveyed in this section use a mode signal v to represent the set of finite modes of operation so as to distinguish it from the fault severity level σ . A switched linear system has the form

$$\begin{aligned} \dot{x} &= A_v x + B_v u \\ y &= C_v x + D_v u, \end{aligned} \tag{2}$$

where $v \in \{1, 2, \dots, n_{modes}\}$ is the unknown switching sequence, $A_i \in \mathbb{R}^{n \times n}$, $B_i \in \mathbb{R}^{n \times m}$, $C_i \in \mathbb{R}^{p \times n}$, $D_i \in \mathbb{R}^{p \times m}$ for $i = 1, 2, \dots, n_{modes}$, and u is the measurable control input. Given a piecewise continuous mode sequence v , piecewise continuous input u , and initial condition $x_0 \in \mathbb{R}^n$, the differential equation (2) has a unique solution $x(t)$. Consequently, the output sequence corresponding to the state sequence $x(t)$ is unique. Given that the input u and output y are measured, the switched system observability problem is to determine the initial state x_0 and mode sequence $v(t)$ from the given measurements. Conditions for solvability are first addressed.

In the case of no input, $u \equiv 0$, it is proven in [9] that the switching sequence $v(t)$ and initial state x_0 is observable given output measurements y if and only if for each pair of modes $i \neq j \in \{1, 2, \dots, n_{modes}\}$ the extended linear system

$$\begin{aligned}\tilde{x} &= A_{i,j}\tilde{x} \\ \tilde{y} &= C_{i,j}\tilde{x}\end{aligned}$$

with system matrices

$$A_{i,j} = \begin{bmatrix} A_i & 0 \\ 0 & A_j \end{bmatrix}, \quad C_{i,j} = \begin{bmatrix} C_i & C_j \end{bmatrix},$$

is observable (in the classical sense). The addition of a smooth input u is considered in [11]. Therein, it is proven that the switching sequence $v(t)$ and initial state x_0 is reconstructable given input and output measurements for almost every smooth input if each pair (A_i, C_i) , $i \in \{1, 2, \dots, n_{modes}\}$, is observable (in the classical sense) and there is a nonzero difference in the Toeplitz matrices, $\Gamma_{2n}(A_i, B_i, C_i, D_i) - \Gamma_{2n}(A_j, B_j, C_j, D_j) \neq 0$, for each $i \neq j \in \{1, 2, \dots, n_{modes}\}$, where

$$\Gamma_{2n}(A, B, C, D) = \begin{bmatrix} D & 0 & 0 & \dots & 0 & 0 \\ CB & D & 0 & \dots & 0 & 0 \\ CAB & CB & D & \dots & 0 & 0 \\ CA^2B & CAB & CB & \ddots & 0 & 0 \\ \vdots & \ddots & \ddots & \ddots & \ddots & \vdots \\ CA^{2n-1}B & CA^{2n-2}B & CA^{2n-3}B & \dots & CB & D \end{bmatrix}. \quad (3)$$

These observability results are extended in [12] for nonsmooth inputs, but this is beyond the scope of this review.

E. Application to ITSC Fault Observability

Let $\sigma_1 \neq \sigma_2 \in [0, 1]$ be two degrees of fault. Are these two degrees of fault distinguishable? To verify this, one can construct LTI systems for each degree of fault. Using the notation in (2), define $A_{\sigma_i} = E^\dagger(\sigma_i)A(\sigma_i)$, $B_{\sigma_i} = E^\dagger(\sigma_i)B(\sigma_i)$, $C_{\sigma_i} = C(\sigma_i)$, and $D_{\sigma_i} = C(\sigma_i)$ for $i = 1, 2$. LTI systems $(A_{\sigma_1}, B_{\sigma_1}, C_{\sigma_1}, D_{\sigma_1})$ and $(A_{\sigma_2}, B_{\sigma_2}, C_{\sigma_2}, D_{\sigma_2})$ are distinguishable for almost all inputs if

$$\|\Gamma_{2n}(A_{\sigma_1}, B_{\sigma_1}, C_{\sigma_1}, D_{\sigma_1}) - \Gamma_{2n}(A_{\sigma_2}, B_{\sigma_2}, C_{\sigma_2}, D_{\sigma_2})\|_F^2 \neq 0. \quad (4)$$

Treating σ_1 and σ_2 as variables, the norm defined in (4) is a polynomial in σ_1 and σ_2 . If (4) is nonzero for some pair (σ_1, σ_2) , then the set of indistinguishable degrees of fault is an algebraic variety of lower dimension intersected with the interval $[0, 1]$, i.e., almost all degrees of fault are distinguishable.

In summary, the ITSC fault detection problem can be viewed as a switched system with unknown switching sequence $\sigma(t)$. The objective is to estimate the switching sequence $\sigma(t)$ and fault current i_{fs} using a modified form of the MHO introduced in [5]. In Section IV, if certain nonlinear observability conditions are satisfied (highly difficult to verify) the modified MHO observer can be proven to converge. Alternatively, the switched system observability conditions in (4) are easily verified and sufficient to guarantee that distinguishability between almost all degrees of ITSC fault, provided there exists a pair (σ_1, σ_2) which are distinguishable. When σ_1 and σ_2 are sufficiently close, there is, of course, a level of distinguishability based on how close (4) is to zero. Practically speaking, this is inconsequential for the MHO since the degree of fault is approximated with a nonlinear optimization rather than “distinguishing” between two adjacent levels of fault.

Section II introduces a model for the SPMSM without fault. Section III introduces the ITSC fault model for an SPMSM. Sections IV and V develop the ITSC fault detection observer. The developed observer is simulated in Section VI. Applications to fault-tolerant supervisory vehicle control and heavy hybrid vehicles are explored in Sections VII and VIII, respectively.

II. SURFACE PMSM WITHOUT A FAULT

Figure 1 illustrates the positioning of the permanent magnets on the rotor. The permanent magnets are positioned on the surface of the rotor to provide the largest magnetic flux variation in the stator windings

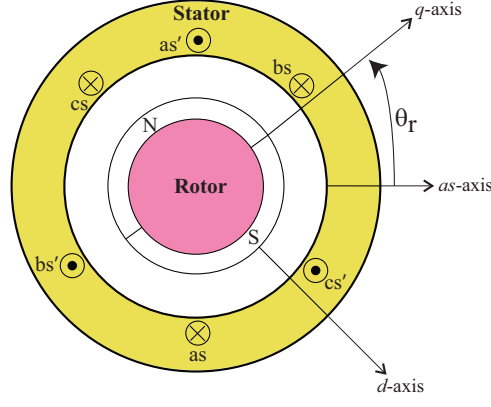


Fig. 1. This figure is a cross-sectional illustration of the SPMSM. The SPMSM has permanent magnets on the surface of the rotor and coils wound into the stator. Typically, SPMSM have more than two permanent magnets fixed to the rotor surface, unlike the two shown for illustrative purposes.

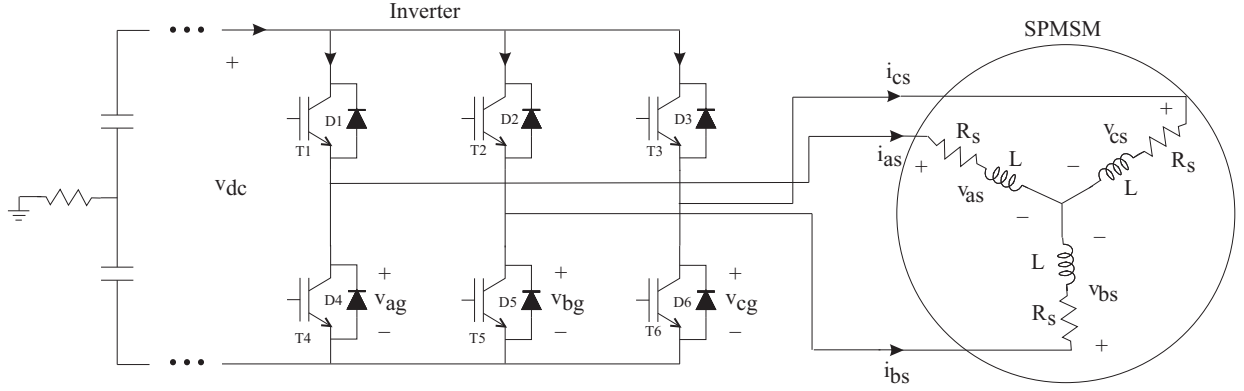


Fig. 2. The SPMSM stator connected to the DC-AC inverter. The wye configuration of the SPMSM stator winding is wound with a neutral point as shown on the right. As illustrated on the far left, the negative rail may not be connected to ground directly.

for a given magnet strength. Nearly all of the rotor surface is magnetically hard, i.e. the rotor surface is covered by permanent magnets which maintain polarity under normal operation [1]. Motor torque is produced through the interaction of the magnetic fields produced by the rotor and those of the stator windings. The SPMSM is powered by a DC-AC inverter as illustrated in Figure 2. The wye configuration of the SPMSM stator is common in electric machines [1] and is the only configuration considered in this work.

For the unfaulted case, the voltages of the three-phase SPMSM using the phase specific voltages and

currents is given by ([1] and [13])

$$\begin{bmatrix} v_{as} \\ v_{bs} \\ v_{cs} \end{bmatrix} = \begin{bmatrix} R_s & 0 & 0 \\ 0 & R_s & 0 \\ 0 & 0 & R_s \end{bmatrix} \begin{bmatrix} i_{as} \\ i_{bs} \\ i_{cs} \end{bmatrix} + \begin{bmatrix} L & M & M \\ M & L & M \\ M & M & L \end{bmatrix} \frac{d}{dt} \begin{bmatrix} i_{as} \\ i_{bs} \\ i_{cs} \end{bmatrix} + \begin{bmatrix} e_a \\ e_b \\ e_c \end{bmatrix}, \quad (5)$$

where $v_{\zeta s}$ and $i_{\zeta s}$ denote the stator voltage and current in phase $\zeta = a, b, c$, respectively; R_s is the stator coil resistance in each phase; L and M denote the self and mutual inductance, respectively; and e_{ζ} is the back electromotive force (emf) in phase $\zeta = a, b, c$. Note, that Kirchoff's current law imposes the constraint $i_{as} + i_{bs} + i_{cs} = 0$, can be used to construct a reduced-order state model. Prior to an ITSC fault, the back emf is

$$\begin{bmatrix} e_a \\ e_b \\ e_c \end{bmatrix} = \omega_r \lambda_m \begin{bmatrix} \cos(\theta_r) \\ \cos(\theta_r - 2\pi/3) \\ \cos(\theta_r + 2\pi/3) \end{bmatrix}, \quad (6)$$

where ω_r and θ_r are the electrical rotor speed and position, respectively, and λ_m is the flux linkage. For almost all nonzero values of L and M , the coefficient matrix of the derivative of the phase currents is nonsingular. Hence (5) can be converted to a time-varying affine state model due to the time-varying back electromotive force voltage vector of (6).

The electromagnetic torque couples the electrical and mechanical components of the SPMSM. Without fault, the electromagnetic torque T_e and mechanical load torque T_L are related by a conservation of power equation

$$T_e \omega_{rm} = e_a i_{as} + e_b i_{bs} + e_c i_{cs} = J \omega_{rm} \dot{\omega}_{rm} + B \omega_{rm}^2 + T_L \omega_{rm}, \quad (7)$$

with mechanical angular speed $\omega_{rm} = \frac{d\theta_{rm}}{dt} = \omega_r / n_p$ where the rotor has $n_p/2$ magnetic pole pairs, moment of inertia J , and viscous friction coefficient B , as illustrated in Figure 3.

A. Extensions to supervisory powerflow modeling

For supervisory level control, each component of the powertrain is minimally modeled as a power transfer device, to be described in detail later in this report. To develop a power flow model for the SPMSM, we relate the power transferred from the inverter in each phase $\zeta = a, b, c$, denoted $P_{inv,\zeta} = v_{\zeta s} i_{\zeta s}$,

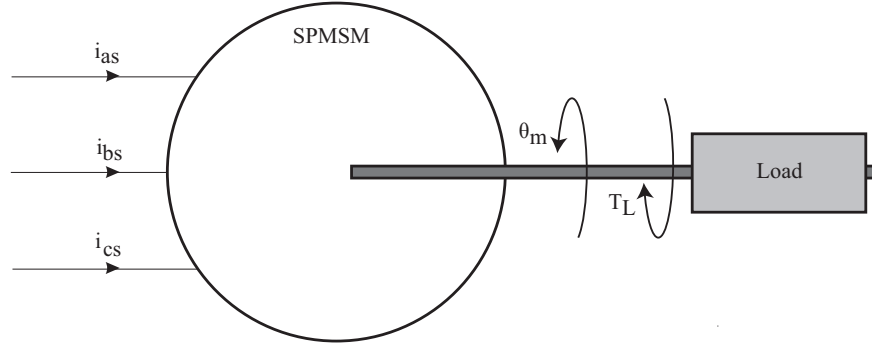


Fig. 3. SPMSM rotor connected to mechanical load. The rotor position is denoted θ_{rm} and load torque T_L .

to the rotor via electromagnetic power contributed in each phase $\zeta = a, b, c$, denoted $P_\zeta = e_\zeta i_{\zeta s}$. The relationship between the inverter-supplied power and electromagnetic power can be expressed in matrix form by premultiplying both sides of (5) by $\text{diag}(i_{as}, i_{bs}, i_{cs})$ to obtain

$$\begin{bmatrix} P_{inv,a} \\ P_{inv,b} \\ P_{inv,c} \end{bmatrix} = \begin{bmatrix} R_s & 0 & 0 \\ 0 & R_s & 0 \\ 0 & 0 & R_s \end{bmatrix} \begin{bmatrix} i_{as}^2 \\ i_{bs}^2 \\ i_{cs}^2 \end{bmatrix} + \begin{bmatrix} i_{as} & 0 & 0 \\ 0 & i_{bs} & 0 \\ 0 & 0 & i_{cs} \end{bmatrix} \begin{bmatrix} L & M & M \\ M & L & M \\ M & M & L \end{bmatrix} \frac{d}{dt} \begin{bmatrix} i_{as} \\ i_{bs} \\ i_{cs} \end{bmatrix} + \begin{bmatrix} P_a \\ P_b \\ P_c \end{bmatrix}. \quad (8)$$

The total power supplied by the inverter is $P_{inv} \triangleq P_{inv,a} + P_{inv,b} + P_{inv,c}$. Hence by conservation of power,

$$P_{inv} = R_s i_{as}^2 + R_s i_{bs}^2 + R_s i_{cs}^2 + \frac{d}{dt} \Upsilon + P_a + P_b + P_c, \quad (9)$$

where the quantity

$$\Upsilon = \frac{1}{2} \begin{bmatrix} i_{as} & i_{bs} & i_{cs} \end{bmatrix} \begin{bmatrix} L & M & M \\ M & L & M \\ M & M & L \end{bmatrix} \begin{bmatrix} i_{as} \\ i_{bs} \\ i_{cs} \end{bmatrix} \quad (10)$$

is a Lyapunov-like energy function.

By using the quantity Υ it is possible to avoid certain kinds of singularities when optimizing the powerflow equations. Clearly, the terms $R_s i_{as}^2$, $R_s i_{bs}^2$, and $R_s i_{cs}^2$ represent winding losses while P_a , P_b , and P_c are back electro-motive powers. Hence, the analog of (7) in the supervisory power flow context is

$$P_a + P_b + P_c = J\omega_{rm}\dot{\omega}_m + B\omega_{rm}^2 + P_L, \quad (11)$$

where P_L is the power delivered to the load. These equations are ultimately used to develop efficiency maps that relate the input and output powers as functions of the mechanical rotor speed ω_{rm} and desired output power P_L . Note, the winding losses are a function of the commanded current signals i_{as} , i_{bs} , and i_{cs} . The efficiency maps will be constructed by computing an optimal current control, which satisfies the physical operating constraints of the motor.

III. EXTENDED MATRIX EQUATIONS: MODELING ITSC FAULT IN SURFACE PMSM

In this section we extend the model for the SPMSM developed in the previous section to include a single ITSC fault. The fault model will include a degree or level of fault via the parameter $\sigma \in [0, 1]$. In the special no-fault-case when $\sigma = 0$, the fault model reduces to the model in (5)-(11).

A. ITSC fault equation description

As discussed in [13], an ITSC fault causes imbalance or loss of symmetry between the variables of the three phases of the stator windings. This imbalance makes the conventional dq0-model [1] much less convenient for analysis of the SPMSM. Consequently, we construct the ITSC fault model using phase variables. For notation, let i_{fs} denote the shorted coil's eddy current induced by the nearby time-varying magnetic fields. Let $\sigma = N_f/N_T$ denote the fraction of faulted turns N_f among the total N_T turns in the faulted phase. Based on [13], this shorted coil has resistance σR_s , flux linkage $\sigma \lambda_m$, self inductance $\sigma^2 L$, and mutual inductance σM between the remaining healthy phases. The phase containing the ITSC fault has $(N_T - N_f)$ unfaulted turns reducing the resistance to $(1 - \sigma)R_s$, flux linkage to $(1 - \sigma)\lambda_m$, self inductance to $(1 - \sigma)^2 L$, and mutual inductance between the other healthy phases to $(1 - \sigma)M$. The shorted coil and the phase containing the ITSC fault are also inductively coupled. Since the shorted coil is wound on the same stator tooth as the remaining healthy turns in that phase, the shorted coil and loop containing the shorted coil have a mutual inductance $\sigma(1 - \sigma)L$.¹ For simplicity, we will assume that the fault occurs in phase-a. It is a straightforward extension to model the fault in phase-b or phase-c. If there are faults in two phases simultaneously, two eddy currents will be present as per the models developed in the appendix.

¹This equation differs from those in [13] to ensure that the mutual inductances are physically realizable.

The stator voltage equations with a single ITSC fault in phase-a, suitably modified from those appearing in [13], are given by

$$\begin{bmatrix} v_{as} \\ v_{bs} \\ v_{cs} \\ 0 \end{bmatrix} = \begin{bmatrix} (1-\sigma)R_s & 0 & 0 & 0 \\ 0 & R_s & 0 & 0 \\ 0 & 0 & R_s & 0 \\ 0 & 0 & 0 & \sigma R_s \end{bmatrix} i_{abcf} + L_f(\sigma) \frac{d}{dt} i_{abcf} + \begin{bmatrix} e_a \\ e_b \\ e_c \\ e_f \end{bmatrix}, \quad (12)$$

where $i_{abcf} \triangleq [i_{as}, i_{bs}, i_{cs}, i_{fs}]^T$ and

$$L_f(\sigma) = \begin{bmatrix} (1-\sigma)^2 L & (1-\sigma)M & (1-\sigma)M & \sigma(1-\sigma)L \\ (1-\sigma)M & L & M & \sigma M \\ (1-\sigma)M & M & L & \sigma M \\ \sigma(1-\sigma)L & \sigma M & \sigma M & \sigma^2 L \end{bmatrix}. \quad (13)$$

The back emf terms are given by

$$\begin{bmatrix} e_a \\ e_b \\ e_c \\ e_f \end{bmatrix} = \omega_r \lambda_m \begin{bmatrix} (1-\sigma) \cos(\theta_r) \\ \cos(\theta_r - 2\pi/3) \\ \cos(\theta_r + 2\pi/3) \\ \sigma \cos(\theta_r) \end{bmatrix}. \quad (14)$$

Note that the fault loop has back emf e_f which has the same phase angle as the back emf in phase-a where the fault occurs. We can also observe that when there are no faults (i.e. $\sigma = 0$) equations (12)-(14) reduce to the unfaulted model in (8)-(11).

B. Extensions to supervisory powerflow modeling: fault case

The above fault-dependent equation descriptions can be extended to explore the power relationship between the inverter, stator, and rotor post ITSC fault. The electromechanical power couples the electrical and mechanical components of the SPMSM as per the following conservation of power equation

$$T_e \omega_{rm} = P_a + P_b + P_c + P_f = J \omega_{rm} \dot{\omega}_{rm} + B \omega_{rm}^2 + T_L \omega_{rm}, \quad (15)$$

where $P_\zeta = e_\zeta i_{\zeta s}$ for $\zeta = a, b, c, f$ Equation (15) which is the analog of (7). Note that P_f may appear to increase the total electromagnetic power in (15), but according to Lenz's Law the power P_f will always

oppose the changing magnetic field. When the inverter-supplied power P_{inv} is zero, then P_f will oppose rotor movement similar to a frictional loss. When P_{inv} is nonzero, then P_f will reduce the combined change in magnetic field due to the mutual inductance from the remaining healthy coils and the rotor movement.

By pre-multiplying (12) by the vector of phase and fault currents, the power flows between the inverter and stator (analogous to (8)) are related by

$$\begin{bmatrix} P_{inv,a} \\ P_{inv,b} \\ P_{inv,c} \\ 0 \end{bmatrix} = \begin{bmatrix} (1-\sigma)R_s & 0 & 0 & 0 \\ 0 & R_s & 0 & 0 \\ 0 & 0 & R_s & 0 \\ 0 & 0 & 0 & \sigma R_s \end{bmatrix} \begin{bmatrix} i_{as}^2 \\ i_{bs}^2 \\ i_{cs}^2 \\ i_{fs}^2 \end{bmatrix} + \begin{bmatrix} i_{as} & 0 & 0 & 0 \\ 0 & i_{bs} & 0 & 0 \\ 0 & 0 & i_{cs} & 0 \\ 0 & 0 & 0 & i_{fs} \end{bmatrix} L_f(\sigma) \frac{d}{dt} \begin{bmatrix} i_{as} \\ i_{bs} \\ i_{cs} \\ i_{fs} \end{bmatrix} + \begin{bmatrix} P_a \\ P_b \\ P_c \\ P_f \end{bmatrix}. \quad (16)$$

Finally, the total inverter power for the faulted case, $P_{inv} = P_{inv,a} + P_{inv,b} + P_{inv,c}$, satisfies the conservation of power equation

$$P_{inv} = (1-\sigma)R_s i_{as}^2 + R_s i_{bs}^2 + R_s i_{cs}^2 + \sigma R_s i_{fs}^2 + \frac{d}{dt} \Upsilon_f(\sigma) + P_a + P_b + P_c + P_f, \quad (17)$$

where the new Lyapunov-like energy function Υ_f is

$$\Upsilon_f(\sigma) = \begin{bmatrix} i_{as} & i_{bs} & i_{cs} & i_{fs} \end{bmatrix} L_f(\sigma) \begin{bmatrix} i_{as} \\ i_{bs} \\ i_{cs} \\ i_{fs} \end{bmatrix}. \quad (18)$$

As expected, when $\sigma = 0$, equations (15) and (16) reduce to the equivalent unfaulted equations given in (7) and (8), respectively.

C. Fault Current Simulation

In Section VI, an SPMSM is simulated at a constant rotor speed of $\omega_{rm} = 700$ rpm with controlled currents given in (50) for parameter values given in Table I. To develop some qualitative understanding and to demonstrate how an ITSC fault affects the motor, we simulate the fault model (12) subject to an ITSC fault in phase-a occurring at 0.5s. Given the controlled currents as in (50), after the fault occurs

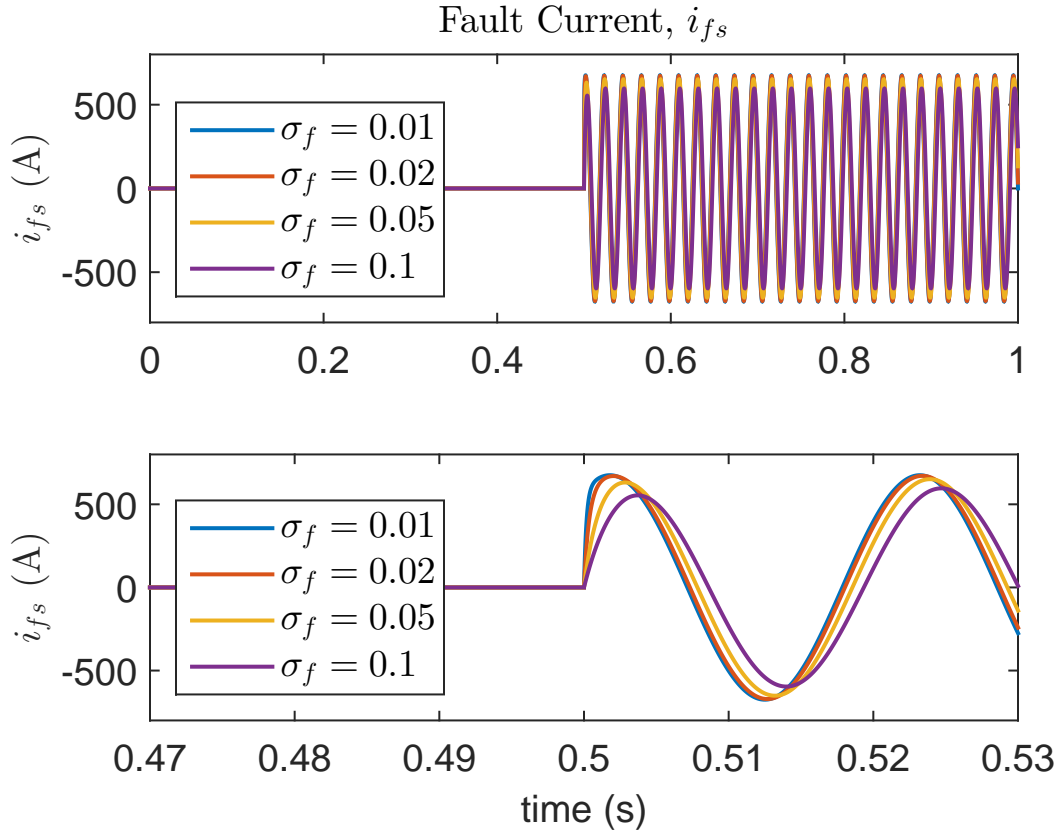


Fig. 4. Fault current for various degrees of fault. The fault of severity σ_f occurs at 0.5s. The lower figure zooms in on the interval surrounding 0.5s to see the difference between each level of fault severity.

the eddy current, i_{fs} , is excited, as illustrated in Figure 4. To demonstrate how the fault severity affects the fault current, i_{fs} is simulated for four fault severity levels, $\sigma_f = 1\%, 2\%, 5\%, 10\%$, again shown in Figure 4. When the ITSC fault occurs, the fault current, i_{fs} , is excited to roughly ten times the magnitude of 50A for the controlled current specified in (50). As long as the rotor is turning, the permanent magnets mounted thereon, will induce a large eddy current in the faulted coil. The eddy current generates heat that can become a safety hazard by causing further electrical insulation failures.

To maintain the desired stator current waveforms in (50), the commanded stator voltages v_{as} , v_{bs} , and v_{cs} will also change based on the degree of fault, as shown in Figure 5. Note, the simulation illustrated in Figures 4 and 5 presumes that the controlled voltages maintain the desired stator currents “instantaneously”. This is why the stator voltages jump at 0.5s. Usually current control is implemented via a closed loop current controller. In practice, the current control loop is less responsive, but will have a reasonably fast time constant. One observes that the transient behavior in this simulation quickly dies away (about 5ms).

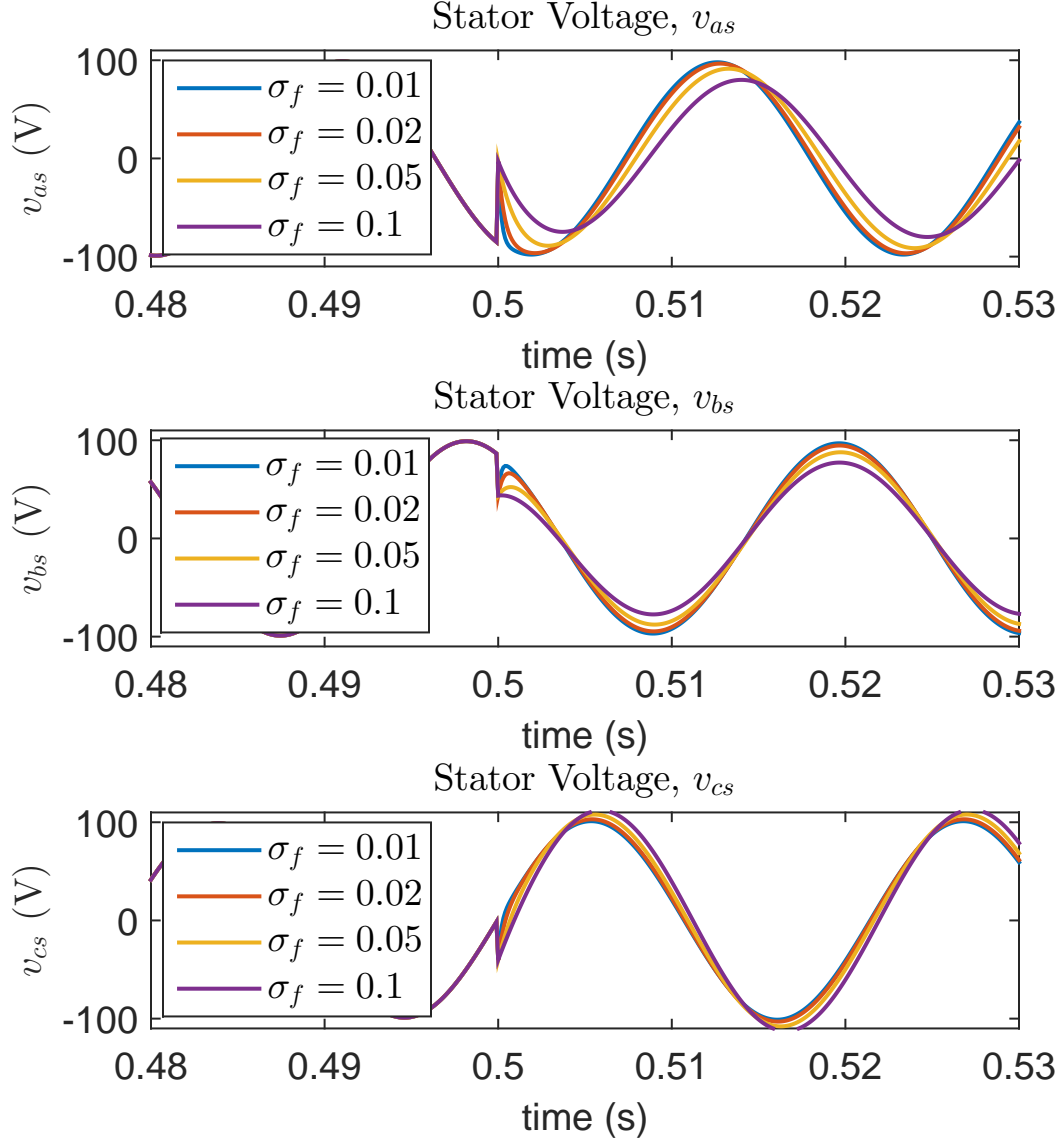


Fig. 5. Stator voltages for various degrees of fault. The fault of severity σ_f occurs at 0.5s. The stator voltage is assumed to be chosen to maintain stator currents given in (50).

The simulation in Section VI is concerned primarily with the steady-state behavior so the simplifying assumption that the current loop is more or less instantaneous will have little effect.

Although the fault current i_{fs} is excited to over ten times the magnitude of the controlled stator currents, the amount of energy dissipated via heat in the shorted coil depends on the faulted coil resistance $\sigma_f R_s$. Figure 6 plots the instantaneous inverter-supplied power P_{inv} and electro-motive power P_{abcf} . When the

ITSC fault occurs at 0.5s, both the inverter-supplied power and the electro-motive power exhibit oscillatory behavior due to the imbalance between the power transfer of the three phases. To show how the magnitude of the power flows are affected by the ITSC fault, Figure 7 plots the average inverter-supplied power \bar{P}_{inv} and the average electro-motive power \bar{P}_{abcf} for each degree of fault, $\sigma_f = 1\%, 2\%, 5\%, 10\%$. The averages \bar{P}_{inv} and \bar{P}_{abcf} are computed at time t by averaging the instantaneous power over the window $[t - T_{period}, t]$ where $T_{period} = \frac{2\pi}{\omega_r}$ is the electrical period. As Figure 7 illustrates, the electromagnetic output power \bar{P}_{abcf} drops as the degree of fault increases. It is also interesting to note that the inverter supplied power \bar{P}_{inv} also changes slightly as a function of the degree of fault. At 10% fault, the efficiency $100 \times \bar{P}_{abcf} / \bar{P}_{inv}$ drops to about 50%. Since this “lost” energy is converted to heat within the shorted loop, it is safety-critical that the fault is detected quickly.

Is the ITSC fault detectable? From Figure 5, the stator voltages required to maintain the desired stator differ before and after the ITSC fault at 0.5s. However, for a 1% fault, the steady-state voltage signals are only minimally affected. Fortunately, the inverter-supplied power, P_{inv} , provides a far more measurable difference when the fault occurs. As seen in Figure 6, the inverter-supplied power P_{inv} oscillates after the fault occurs. This oscillation is caused by a power contribution imbalance between the faulted and the two unfaulted phase windings. For given commanded currents, the average inverter-supplied power is also affected by the fault as shown in Figure 7. The electromagnetic power P_{abcf} is also plagued by the same oscillatory and average power effects although the electromagnetic power is usually unavailable for direct measurement, see Figures 6 and 7. The measurable differences caused by the ITSC fault demonstrates feasibility of the ITSC fault detection problem. The development of the fault detection method proposed in this report begins in the following section.

IV. NOMINAL FAULT DETECTION OBSERVER

A. ITSC Observer Problem Statement

How can the ITSC fault be detected? In our context, the fault detection observer estimates the degree of fault and fault current consistent with input and output measurements. The fault detection observer is illustrated in Figure 8. The objective of this section is to formalize the ITSC fault detection observer problem. This begins by defining the measured inputs and outputs.

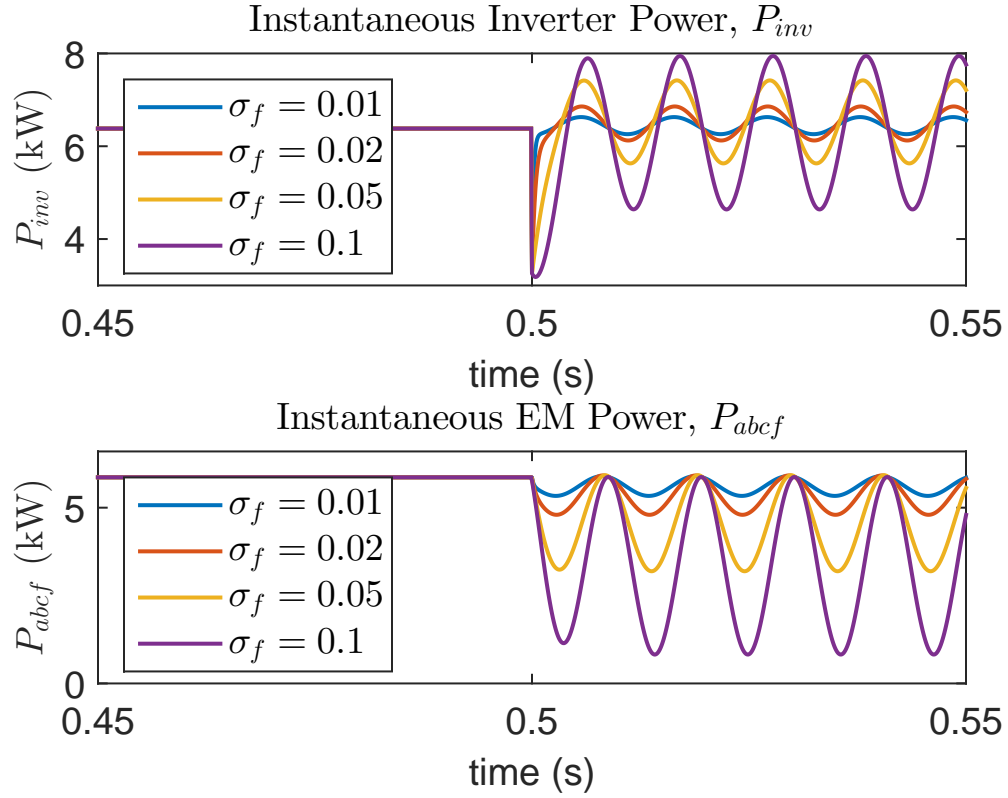


Fig. 6. (top) Plot of the inverter supplied power P_{inv} for various degrees of fault. The fault of severity σ_f occurs at 0.5s. (bottom) Plot of the electromagnetic power P_{abcf} for various degrees of fault.

The currents in the stator of the SPMSM are controlled by the inverter through voltages applied to the stator winding leads relative to the negative rail, denoted v_{ag} , v_{bg} , and v_{cg} . These measurable terminal voltages v_{ag} , v_{bg} , and v_{cg} determine the stator voltages relative to neutral, v_{as} , v_{bs} , and v_{cs} , which in turn drive the stator currents as per (12). Ideally, we would directly measure the stator to neutral voltages $v_{\zeta s}$, $\zeta = a, b, c$. However, electric machine manufacturers rarely provide direct access to neutral making the stator voltages directly unmeasurable or expensive to measure in terms of sensor placement in practice. Sensors for the line to line voltages are more readily available, i.e. measurements of $v_{\zeta w} \triangleq v_{\zeta s} - v_{ws}$ for $\zeta \neq w \in \{a, b, c\}$. The line to line voltages are measurable from the controlled voltages v_{ag} , v_{bg} , and v_{cg} as per

$$\begin{aligned}
 v_{ab}^M &= v_{ag}^M - v_{bg}^M \\
 v_{bc}^M &= v_{bg}^M - v_{cg}^M \\
 v_{ac}^M &= v_{ag}^M - v_{cg}^M,
 \end{aligned} \tag{19}$$

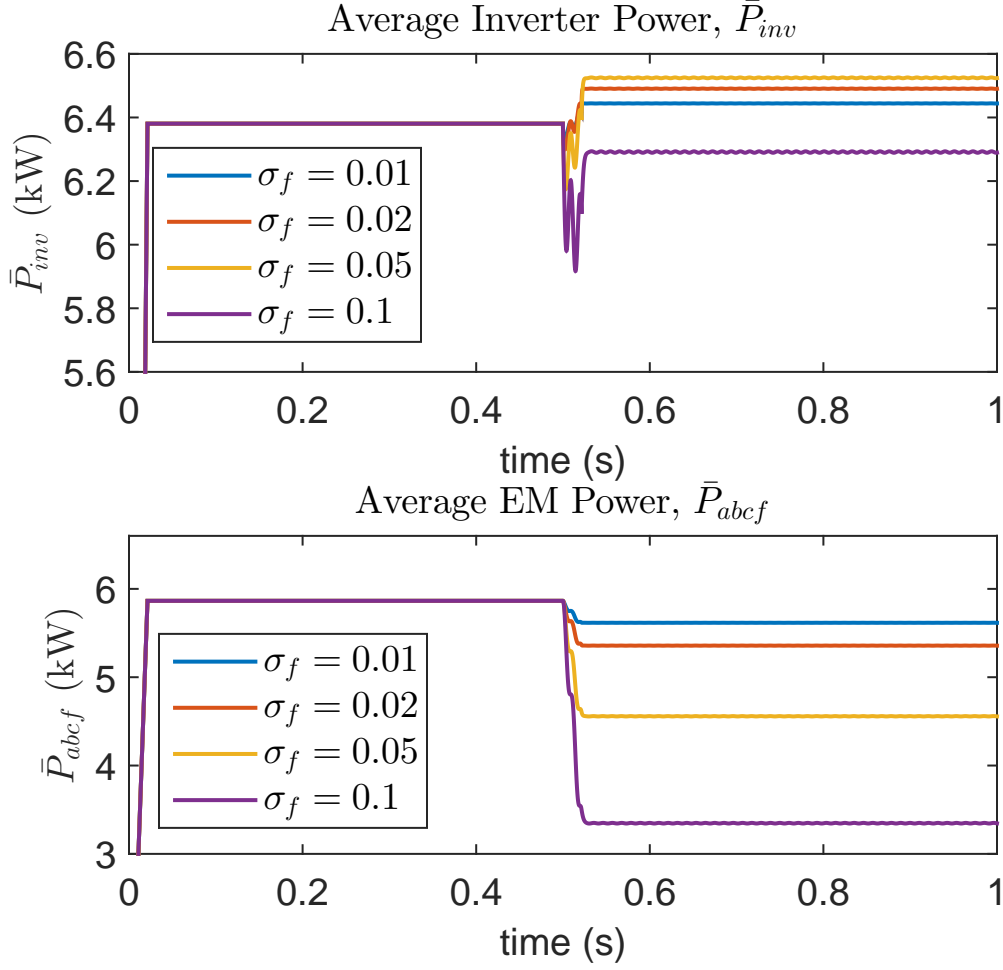


Fig. 7. (top) Plot of the average inverter supplied power \bar{P}_{inv} for various degrees of fault. The average power is computed as the average of the instantaneous power over a window $[t - T_{period}, t]$ for each time t , where $T_{period} = \frac{2\pi}{\omega_r}$ is the period. The fault of severity σ_f occurs at 0.5s. (bottom) Plot of the average electromagnetic power \bar{P}_{abcf} for various degrees of fault. The average electromagnetic power is also computed as an average of the instantaneous power over the window $[t - T_{period}, t]$.

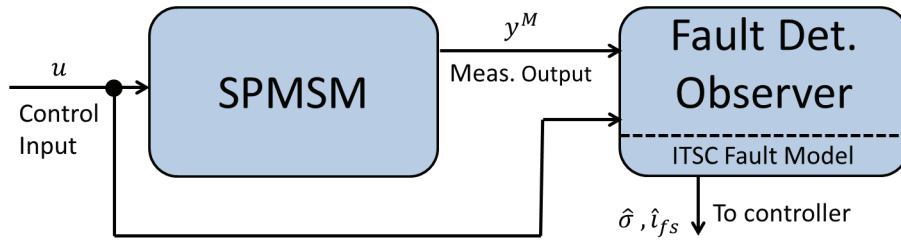


Fig. 8. The fault detection observer uses known control input u , measured output y^M , and the ITSC fault model to produce an estimate for the degree of fault $\hat{\sigma}$ and the fault current \hat{i}_{fs} .

where the superscript M denotes measured signals. We also consider the electrical position θ_r and speed ω_r of the rotor to be measured signals. Using these measurements, the back emf e_{abcf} can be expressed as

$$\begin{bmatrix} e_a \\ e_b \\ e_c \\ e_f \end{bmatrix} = \begin{bmatrix} 1 - \sigma & 0 & 0 \\ 0 & 1 & 0 \\ 0 & 0 & 1 \\ \sigma & 0 & 0 \end{bmatrix} \begin{bmatrix} \omega_r^M \lambda_m \cos(\theta_r^M) \\ \omega_r^M \lambda_m \cos(\theta_r^M - 2\pi/3) \\ \omega_r^M \lambda_m \cos(\theta_r^M + 2\pi/3) \end{bmatrix}. \quad (20)$$

Note that the only unknown in (20) is σ , which is estimated. Thus the rightmost matrix in (20) becomes another measured input.

Since many commercial electric drive systems utilize stator current control, sensors are often available for the stator currents $i_{\zeta s}$, $\zeta = a, b, c$. We assume that each of the stator currents is available for measurement. In practice, we can reduce the number of sensors since the stator currents satisfy Kirchoff's current law, i.e., $i_{as} + i_{bs} + i_{cs} = 0$. One may be able to use a reduced number of sensors, but this reduction is not explored in this report.

When an ITSC fault occurs, the same voltage potential on the phase terminals produces different stator current responses. Essentially, the ITSC fault detection observer matches the given voltage signals to the resulting current measurements to determine the degree of fault σ , the fault current i_{fs} , and the stator currents $i_{\zeta s}$, $\zeta = a, b, c$. We can now pose the ITSC fault observer problem.

ITSC Observer Problem: Estimate the fault severity σ , fault current i_{fs} , and stator currents $i_{\zeta s}$, $\zeta = a, b, c$, given the ITSC fault model (12), measured signal

$$y^M = \begin{bmatrix} v_{ab}^M & v_{bc}^M & v_{ca}^M & i_{as}^M & i_{bs}^M & i_{cs}^M \end{bmatrix}^\top, \quad (21)$$

and known electrical rotor speed ω_r^M and position θ_r^M where the superscript M denotes measured variables.

ITSC fault detection is a nonlinear observer problem. For each fixed degree of fault σ , the dynamics in (12) are linear with respect to i_{abcf} , but an unknown degree of fault σ introduces a nontrivial nonlinearity. One approach to solving nonlinear observability problems is to use linear observers, such as the classical Luenberger dynamical observer [14]. Linear observers are numerically simple and well understood, but in general perform poorly on highly nonlinear systems. As an alternative, we propose the optimization-based approach developed in [5], known as a moving horizon estimator or moving horizon observer (MHO).

B. Moving Horizon Observer

As mentioned in the introduction, the MHO re-poses the estimation problem as an optimization problem. Consider the following nonlinear system

$$\begin{aligned}\dot{x} &= f(x, u^M) \\ y^M &= g(x, u^M),\end{aligned}\tag{22}$$

where $x \in \mathbb{R}^n$ is the state, $y^M \in \mathbb{R}^p$ is the measured output, $u^M : \mathbb{R} \rightarrow \mathbb{R}^m$ is the bounded measurable input, and $f : \mathbb{R}^n \times \mathbb{R}^m \rightarrow \mathbb{R}^n$ and $g : \mathbb{R}^n \times \mathbb{R}^m \rightarrow \mathbb{R}^p$ are known, locally Lipschitz functions with respect to both x and u^M . Recall that for \mathcal{A}, \mathcal{B} metric spaces, $h : \mathcal{A} \rightarrow \mathcal{B}$ is a locally Lipschitz function if for all $a \in \mathcal{A}$ there exists a neighborhood U_a of a and a constant K such that for all $a_1, a_2 \in U_a$, $\|h(a_1) - h(a_2)\|_A \leq K\|a_1 - a_2\|_B$, where $\|\cdot\|_A$ and $\|\cdot\|_B$ denote the metric in \mathcal{A} and \mathcal{B} , respectively.

The MHO developed in [5] is based on solving the optimization problem

$$\min_{\hat{x}_0 \in \mathbb{R}^n} \int_{t-T}^t \|y^M(t) - \hat{y}(t)\|^2 dt\tag{23}$$

subject to:

$$\dot{\hat{x}}(t) = f(\hat{x}(t), u^M(t)), \quad \hat{x}(t-T) = \hat{x}_0\tag{24}$$

$$\hat{y}(t) = g(\hat{x}(t), u^M(t)).\tag{25}$$

where T is the finite horizon and $\hat{y}(t)$ is the estimated output driven by the state trajectory $\hat{x}(t)$ which satisfies the underlying differential equation with the estimated initial condition \hat{x}_0 . The specific approach in [5] is not to solve (23) at each time t but rather to sequentially solve the optimization over successive horizon windows $[t_k - T, t_k]$ where $t_1 < t_2 < t_3 < \dots$. However, our approach is not to achieve the absolute minimum over $[t_k - T, t_k]$, but rather to impose a cost reduction by a factor of $\beta \in (0, 1)$ from one window to the next. So if at time t_k , the norm in (23) is equal to K_k , then over the next horizon $[t_{k+1} - T, t_{k+1}]$ the minimization in (23) is iterated until the norm is less than $K_{k+1} = \beta K_k$. This would continue until the norm in (23) is in a sufficiently small neighborhood of zero, in which case $y^M(t) - \hat{y}(t; \hat{x}_0) \approx 0$. Given the presence of modeling errors, sensor noise, and numerical round-off, reaching the “perfect minimum” of zero is unlikely. The benefit of this approach is that the observer/estimate convergence improves incrementally over successive horizons in contrast to the larger computational effort needed to achieve the minimum of (23) over each horizon.

To guarantee solvability of the observer problem, it is assumed that for each initial condition $x_0, x'_0 \in \mathbb{R}^n$, the corresponding output trajectories $y(x(t), u(t))$ and $y(x'(t), u(t))$ satisfy

$$\int_{t-T}^t \|y(x(t), u(t)) - y(x'(t), u(t))\|^2 dt \geq \gamma \|x_0 - x'_0\|^2, \quad (26)$$

for some fixed $\gamma > 0$. This uniform observability condition reduces to the classical observability Gramian in the case of time-varying linear systems and time-invariant linear systems as shown in Appendix B. The uniform observability condition in (26) is difficult to verify for nonlinear systems. As mentioned earlier, for the ITSC fault detection problem we will presume that the unfaulted state model is observable, which is easily verified for the parameter values of a typical SPMSM and available sensor measurements. Further as asserted earlier, the faulted model is observable for almost all fault levels $\sigma \in [0, 1]$ if observable for at least one fault level σ_1 . Hence, the structure of the SPMSM model allows us to assert generic observability of the system without having to verify the condition of (26).

In general, the MHO is a versatile observer often used to solve nonlinear observability problems [5], [15], [16]. Thus it is well suited for the ITSC fault detection problem. For linear state models, the MHO can be seen as a dual problem to the linear quadratic regulator (LQR) problem and thus enjoys a similar historical success [17], [18].

C. ITSC Observability

Recall that for the ITSC fault detection problem, the variables to be estimated are the stator currents i_{ws} , $w = a, b, c, f$, and the degree of fault σ . First we validate that the observability problem is feasible, i.e., different fault levels are distinguishable and the stator currents i_{ws} are observable.

To analyze the distinguishability of two degrees of fault $\sigma_1 \neq \sigma_2 \in [0, 1]$, we first need to construct a switched linear time-invariant (SLTI) model that incorporates the measured signals in (21) and then verify distinguishability with (4). Unfortunately, only the line-to-line voltages v_{ab} , v_{bc} , and v_{ca} are measurable whereas the stator voltages v_{as} , v_{bs} , and v_{cs} , that appear in the state dynamics of (12) are not. Another problem with (12) is that Kirchoff's current law (KCL) disallows arbitrary initial conditions, because in the wye configuration $i_{as} + i_{bs} + i_{cs} = 0$. This means that (12) contains redundant information and a lower dimensional state model can capture all the relevant dynamical information.

To construct the lower dimensional state model (4^{th} order to 3^{rd} order) that utilizes the measured signals in (21), we do the following:

- 1) using KCL, substitute $i_{cs} = -i_{as} - i_{bs}$ in (12), i.e., for $i_{abf} \triangleq [i_{as}, i_{bs}, i_{fs}]^\top$

$$i_{abcf} = \begin{bmatrix} 1 & 0 & 0 \\ 0 & 1 & 0 \\ -1 & -1 & 0 \\ 0 & 0 & 1 \end{bmatrix} i_{abf} \triangleq M_{abf} i_{abf} \quad (27)$$

- 2) premultiply both sides of (12) by

$$M_v \triangleq \begin{bmatrix} 1 & -1 & 0 & 0 \\ 0 & 1 & -1 & 0 \\ 0 & 0 & 0 & 1 \end{bmatrix} \quad (28)$$

to obtain differential equations as functions of (i) $v_{ab}^M = v_{as} - v_{bs}$ and (ii) $v_{bc}^M = v_{bs} - v_{cs}$.

This results in the reduced-order equivalent state and output model:

$$\tilde{L}_f(\sigma) \frac{d}{dt} i_{abf} = -\tilde{R}_f(\sigma) i_{abf} + \tilde{Q}(\sigma) u^M, \quad (29)$$

$$\tilde{y}^M = \begin{bmatrix} 1 & 0 & 0 \\ 0 & 1 & 0 \end{bmatrix} i_{abf} \triangleq \tilde{C}(\sigma) i_{abf}, \quad (30)$$

where $i_{abf} \triangleq [i_{as}, i_{bs}, i_{fs}]^\top$ is the reduced state vector. The measured input vector is

$$u^M = \begin{bmatrix} \lambda_m \omega_r^M \cos(\theta_r^M) & \lambda_m \omega_r^M \cos(\theta_r^M - 2\pi/3) & \lambda_m \omega_r^M \cos(\theta_r^M + 2\pi/3) & v_{ab}^M & v_{bc}^M \end{bmatrix}^\top, \quad (31)$$

and the measured output is $\tilde{y}^M = [i_{as}, i_{bs}]^\top$. The new linear system matrices in (29) are

$$\begin{aligned} \tilde{L}_f(\sigma) &= M_v L_f(\sigma) M_{abf}, \\ \tilde{R}_f(\sigma) &= M_v \begin{bmatrix} (1-\sigma)R_s & 0 & 0 & 0 \\ 0 & R_s & 0 & 0 \\ 0 & 0 & R_s & 0 \\ 0 & 0 & 0 & \sigma R_s \end{bmatrix} M_{abf}, \\ \tilde{Q}(\sigma) &= \begin{bmatrix} -(1-\sigma) & 1 & 0 & 1 & 0 \\ 0 & -1 & 1 & 0 & 1 \\ -\sigma & 0 & 0 & 0 & 0 \end{bmatrix}, \end{aligned}$$

where M_{abf} and M_v are defined in (27) and (28), respectively.

To verify the fault distinguishability conditions in (4), a standard LTI system is constructed from (29) for each degree of fault σ_1 via the tuple of linear system matrices

$$(A_{\sigma_1}, B_{\sigma_1}, C_{\sigma_1}, D_{\sigma_1}) = \left(\tilde{L}_f^\dagger(\sigma_1) \tilde{R}_f(\sigma_1), \tilde{L}_f^\dagger(\sigma_1) \tilde{Q}(\sigma_1), \tilde{C}(\sigma_1), 0 \right). \quad (32)$$

If there exists two degrees of fault $\sigma_1 \neq \sigma_2$, for which (4) is satisfied, then (for generic inputs) almost all degrees of fault are distinguishable. For the SPMSM parameterized in Table I with $\sigma_1 = 0$ and $\sigma_2 = 1$, we compute

$$\|\Gamma_{2n}(A_{\sigma_1}, B_{\sigma_1}, C_{\sigma_1}, D_{\sigma_1}) - \Gamma_{2n}(A_{\sigma_2}, B_{\sigma_2}, C_{\sigma_2}, D_{\sigma_2})\|_F^2 = 3.16 \times 10^{20} \neq 0. \quad (33)$$

Thus $\sigma_1 = 0$ and $\sigma_2 = 1$ are distinguishable for almost all inputs, as per [11]. To show that almost all degrees of fault are distinguishable for almost all inputs, we consider the nontrivial polynomial (nontrivial by (33)) in σ_1 and σ_2 defined by (34),

$$\|\Gamma_{2n}(A_{\sigma_1}, B_{\sigma_1}, C_{\sigma_1}, D_{\sigma_1}) - \Gamma_{2n}(A_{\sigma_2}, B_{\sigma_2}, C_{\sigma_2}, D_{\sigma_2})\|_F^2. \quad (34)$$

Hence, the set of pairs (σ_1, σ_2) such that (34) is equal to zero is an algebraic variety of lower dimension, i.e., at worst unions of lines in \mathbb{R}^2 . In addition, this algebraic variety must intersect the square $[0, 1] \times [0, 1]$ for two degrees of fault to be indistinguishable. Thus it is possible that the algebraic variety does not intersect $[0, 1] \times [0, 1]$ for pairs (σ_1, σ_2) with $\sigma_1 \neq \sigma_2$, i.e., that all degrees of fault are distinguishable. Hence for generic inputs it follows that almost all degrees of fault are, in fact, distinguishable.

The next question is whether the state i_{abf} is observable once the correct degree of fault is identified. This is verified using classical observability tests on the pair $(A_{\sigma_i}, C_{\sigma_i})$, such as the rank of the observability matrix. For the SPMSM parametrized in Table I with $\sigma_1 = 0$ and $\sigma_2 = 1$, we obtain

$$\text{rank}[\mathcal{O}_3(A_{\sigma_1}, C_{\sigma_1})] = 2$$

$$\text{rank}[\mathcal{O}_3(A_{\sigma_2}, C_{\sigma_2})] = 3,$$

where $\mathcal{O}_3(A, C)$ is the observability matrix for the pair (A, C) , i.e.,

$$\mathcal{O}_i(A, C) = \begin{bmatrix} C^\top & (CA)^\top & \dots & (CA^{i-1})^\top \end{bmatrix}^\top.$$

The result that $\text{rank}[\mathcal{O}_3(A_{\sigma_1}, C_{\sigma_1})] = 2$ implies that the state i_{abf} is not completely observable. This is understandable since $\sigma_1 = 0$ represents the unfaulted SPMSM and the fault current i_{fs} is unobservable because it is zero prior to an ITSC fault. On the other hand, since $\text{rank}[\mathcal{O}_3(A_{\sigma_2}, C_{\sigma_2})] = 3$, the entire state i_{abf} is observable for $\sigma_2 = 1$. Using the same arguments as in Section I-E, this implies that i_{abf} is observable for almost all degrees of fault. Mathematically, the set of degrees of fault σ for which i_{abf} is unobservable is among a finite set of roots to a polynomial in σ . Any root, say $\sigma_* \notin [0, 1]$ is not a physically realizable degree of fault. Hence, it is again possible that the current i_{abf} is observable for all degrees of fault and in the worst case i_{abf} is unobservable for a finite number of degrees of fault. Thus the ITSC observer problem is feasible for almost all degrees of fault.

D. Nominal ITSC Observer

Although it is possible to build a MHO for the reduced order model of the previous section, from a modeling perspective as well as a more direct utilization of the full order model developed earlier, we simply add the KCL equation as a constraint. There are also numerical advantages due to the sparseness of the larger set of equations.

Since the degree of fault is unknown but takes values in the interval $[0, 1]$, we denote the observer below to be the nominal embedded moving horizon observer (EMHO).² As mentioned earlier, we assume that the ITSC fault occurs in phase-a. Relaxing this assumption is a straightforward extension, but the additional notation is not included for clarity.

In the EMHO framework, the ITSC fault detection problem has mode $\sigma \in [0, 1]$ and state $i_{abcf} \triangleq [i_{as}, i_{bs}, i_{cs}, i_{fs}]^\top$. As described in Section IV-B, we consider a discretized set of final times given by $t_1, t_2, \dots, t_k, \dots$. For simplicity, we consider evenly spaced final times, i.e., $t_{k+1} - t_k = T_{shift}$.

So for a given horizon $[t_k - T, t_k]$ and $0 \leq h \leq T$, the nominal ITSC fault EMHO problem with fault

²This formulation is the dual to the embedded hybrid optimal control problem in that σ can vary continuously in $[0, 1]$ (see [18], [19]).

in phase-a is given by

$$\min_{\substack{\hat{i}_{abcf}(t_k-h) \in \mathbb{R}^4 \\ \hat{\sigma}: [t_k-T, t_k] \rightarrow [0,1]}} \int_{t_k-T}^{t_k} \|y^M(t) - \hat{y}(t)\|^2 dt \quad (35)$$

subject to:

$$\hat{v}_{abcf} = R_f(\hat{\sigma})\hat{i}_{abcf} + L_f(\hat{\sigma})\frac{d}{dt}\hat{i}_{abcf} + e_{abcf}(\hat{\sigma}) \quad (36)$$

$$\hat{y} = [\hat{v}_{as} - \hat{v}_{bs}, \hat{v}_{bs} - \hat{v}_{cs}, \hat{v}_{cs} - \hat{v}_{as}, \hat{i}_{as}, \hat{i}_{bs}, \hat{i}_{cs}]^\top \quad (37)$$

$$= [\hat{v}_{ab}, \hat{v}_{bc}, \hat{v}_{ca}, \hat{i}_{as}, \hat{i}_{bs}, \hat{i}_{cs}]^\top$$

$$0 = \hat{i}_{as} + \hat{i}_{bs} + \hat{i}_{cs}, \quad (38)$$

³ where (38) is a result of KCL,

$$\hat{i}_{abcf} = [\hat{i}_{as}, \hat{i}_{bs}, \hat{i}_{cs}, \hat{i}_{fs}]^\top, \quad (39)$$

$$\hat{v}_{abcf} = [\hat{v}_{as}, \hat{v}_{bs}, \hat{v}_{cs}, 0]^\top, \quad (40)$$

$$R_f(\hat{\sigma}) = \begin{bmatrix} (1-\hat{\sigma})R_s & 0 & 0 & 0 \\ 0 & R_s & 0 & 0 \\ 0 & 0 & R_s & 0 \\ 0 & 0 & 0 & \sigma R_s \end{bmatrix} \quad (41)$$

$$L_f(\hat{\sigma}) = \begin{bmatrix} (1-\hat{\sigma})^2 L & (1-\hat{\sigma})M & (1-\hat{\sigma})M & \hat{\sigma}(1-\hat{\sigma})L \\ (1-\hat{\sigma})M & L & M & \hat{\sigma}M \\ (1-\hat{\sigma})M & M & L & \hat{\sigma}M \\ \hat{\sigma}(1-\hat{\sigma})L & \hat{\sigma}M & \hat{\sigma}M & \hat{\sigma}^2 L \end{bmatrix}, \quad (42)$$

and

$$e_{abcf}(\hat{\sigma}) = \omega_r \lambda_m \begin{bmatrix} (1-\hat{\sigma}) \cos(\theta_r) \\ \cos(\theta_r - 2\pi/3) \\ \cos(\theta_r + 2\pi/3) \\ \hat{\sigma} \cos(\theta_r) \end{bmatrix}. \quad (43)$$

³Kirchoff's current law takes the form of (38) only for ITSC faults, i.e., (38) only applies for shorts between phases and not shorts to ground. Modeling shorts to ground are not considered in this report.

Of course, this problem is solved sequentially for each interval $[t_k - T, t_k]$ for $k = 1, 2, \dots$. It is not necessary that these intervals be disjoint. As we will see in the forthcoming development, there are numerical advantages to having these intervals overlap.

Several aspects of the ITSC EMHO warrant explanation and elaboration. First, the variable h allows for the estimated state $\hat{i}_{abcf}(t_k - h)$ to be anywhere within the interval $[t_k - T, t_k]$. For example, when $h = T$ the EMHO observer reduces to the MHO observer described in Section IV-B, in that one is estimating the initial condition $\hat{i}_{abcf}(t_k - T)$ for the interval $[t_k - T, t_k]$. Another way of saying this is that the state estimate at the beginning of the interval, $\hat{i}_{abcf}(t_k - T)$, is either a delayed estimate of the current state $i_{abcf}(t_k)$ or must be integrated using (12). This value could be sensitive to errors in the estimated initial condition. Clearly, then the choice of h has an effect on the numerical implementation of the EMHO.

Moving the state estimate to the beginning of the interval, h small, has a smaller delay and less integration required to obtain the current estimate. Thus, small h naturally emphasizes the most recent measurements and adapts more quickly to changes in the measured output. However, if $h < T_{shift}$, where $T_{shift} = t_{k+1} - t_k$ for each k , then $t_{k+1} - h$ is not contained in the previous interval $[t_k - T, t_k]$ as illustrated in Figure 9. The practical consequence of selecting $h < T_{shift}$ occurs when integrating the previous estimate $\hat{i}_{abcf}(t_k - h)$ from $t_k - h$ to $t_{k+1} - h$ to hot-start the next estimate $\hat{i}_{abcf}(t_{k+1} - h)$. Namely, the issue is that when computing $\hat{i}_{abcf}(t_k - h)$ and $\hat{\sigma}([t_k - T, t_k])$, no measurements from the interval $[t_k, t_{k+1} - h]$ were utilized. Consequently, one either makes assumptions about the interval $[t_k, t_{k+1} - h]$ to allow for the integration (such as assuming the degree of fault σ does not change) or uses another suboptimal initial guess (such as using $\hat{i}_{abcf}(t_k)$ to hot-start $\hat{i}_{abcf}(t_{k+1} - h)$). As passing the previous estimate forward to the next interval is critical for fast algorithm convergence, we further restrict h to be greater than T_{shift} , i.e., $T_{shift} \leq h \leq T$.

A second point to be made is that if there is a short to ground, then (38) is not valid because a short to ground allows some of the current to circumvent the neutral node in the stator windings. Thus we disallow shorts to ground in this discussion.

Thirdly, the minimization over $\hat{\sigma} : [t_k - T, t_k] \rightarrow [0, 1]$ denotes searching for all functions $\hat{\sigma}$ with domain $[t_k - T, t_k]$ and range in $[0, 1]$. The nominal ITSC EMHO problem requires an optimization of $\hat{i}_{abcf}(t_k - h) \in \mathbb{R}^4$ and $\hat{\sigma}$ over functions with range in $[0, 1]$. What has not been utilized in (35)-(38), is the

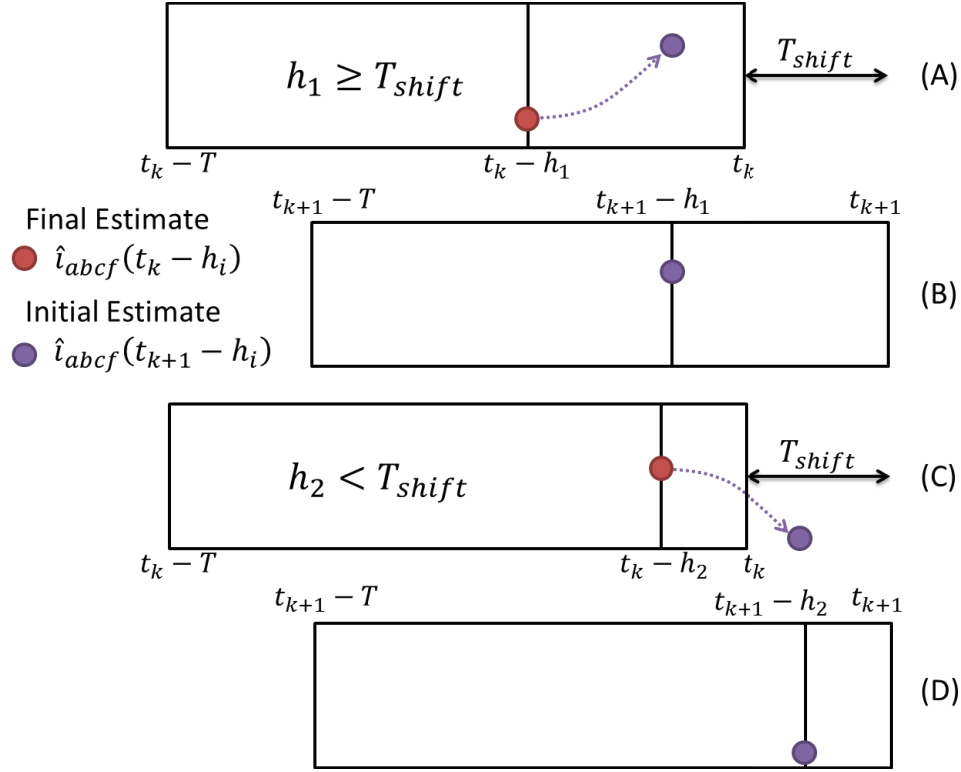


Fig. 9. (A) and (B) illustrate how the previous horizon estimate $\hat{i}_{abcf}(t_k - h_1)$ is integrated forward to hot-start $\hat{i}_{abcf}(t_{k+1} - h_1)$ when $h_1 \geq T_{shift}$. Notice, that the integration is within the interval $[t_k - T, t_k]$. (C) and (D) illustrate when $h_2 < T_{shift}$. Note, that the integration is not contained in $[t_k - T, t_k]$.

steady state behavior inherent in the ITSC observer problem described in Section IV-A. The exploitation of the steady state behavior significantly reduces computation as discussed in the following section.

Finally, if the estimates $\hat{i}_{abcf}(t_k - h) = i_{abcf}(t_k - h)$ and $\hat{\sigma}$ are exact, then the cost function in (35) is zero since both the estimates and actual stator currents would be solutions to the same differential equations and have the same output function. Since (35) is nonnegative, the correct estimates are a minimizing solution to the cost function. If the only solution to (35) is the correct stator current and degree of fault, the observer problem is feasible. Feasibility has been discussed theoretically in Section IV-C and demonstrated through simulation to follow.

V. PRACTICAL OBSERVER IMPLEMENTATION

The time constants associated with the stator currents in the SPMSM are much faster than (i) changes in the mechanical load and (ii) changes in the power command. As a result, our analysis presupposes that the stator currents and voltages are in steady-state. Specifically, the steady-state stator currents and

voltages are assumed to exhibit periodic sinusoidal behavior with frequency ω_r due to the sinusoidal back emf e_{abcf} . Note, this sinusoidal steady-state behavior occurs pre and post ITSC fault since in both cases the back emf e_{abcf} is sinusoidal.

How can we exploit the steady-state periodic sinusoidal behavior of the pre and post fault SPMSM to simplify the optimization problem in (35)? The approach is to explicitly impose the structure that $\hat{i}_{\zeta s}$, $\zeta = a, b, c, f$, are sinusoids with constant magnitudes and phase over subintervals of length t_{part} . The estimation of $\hat{i}_{\zeta s}$ can then be re-posed as estimating gains $\hat{I}_{q\zeta}$ and $\hat{I}_{d\zeta}$, $\zeta = a, b, c, f$, as per the following equations:

$$\hat{i}_{as} = \hat{I}_{qa} \cos(\theta_r) + \hat{I}_{da} \sin(\theta_r) \quad (44a)$$

$$\hat{i}_{bs} = \hat{I}_{qb} \cos(\theta_r - 2\pi/3) + \hat{I}_{db} \sin(\theta_r - 2\pi/3) \quad (44b)$$

$$\hat{i}_{cs} = \hat{I}_{qc} \cos(\theta_r + 2\pi/3) + \hat{I}_{dc} \sin(\theta_r + 2\pi/3) \quad (44c)$$

$$\hat{i}_{fs} = \hat{I}_{qf} \cos(\theta_r) + \hat{I}_{df} \sin(\theta_r). \quad (44d)$$

How does (44) simplify the optimization problem in (35)? The primary simplification is when solving the differential equation in (36). With stator and fault current estimates with the form of (44), the derivatives $\frac{d}{dt}\hat{i}_{\zeta s}$, $\zeta = a, b, c, f$, have the analytic form

$$\frac{d}{dt}\hat{i}_{as} = -\hat{I}_{qa}\omega_r \sin(\theta_r) + \hat{I}_{da}\omega_r \cos(\theta_r) \quad (45a)$$

$$\frac{d}{dt}\hat{i}_{bs} = -\hat{I}_{qb}\omega_r \sin(\theta_r - 2\pi/3) + \hat{I}_{db}\omega_r \cos(\theta_r - 2\pi/3) \quad (45b)$$

$$\frac{d}{dt}\hat{i}_{cs} = -\hat{I}_{qc}\omega_r \sin(\theta_r + 2\pi/3) + \hat{I}_{dc}\omega_r \cos(\theta_r + 2\pi/3) \quad (45c)$$

$$\frac{d}{dt}\hat{i}_{fs} = -\hat{I}_{qf}\omega_r \sin(\theta_r) + \hat{I}_{df}\omega_r \cos(\theta_r). \quad (45d)$$

Hence, the differential equation in (36) can be replaced with an algebraic equation (with respect to estimated variables $\hat{I}_{q\zeta}$ and $\hat{I}_{d\zeta}$, $\zeta = a, b, c, f$). This greatly reduces the complexity and computational time required to compute \hat{y} in the cost function.

To apply the assumption that the stator currents are fixed sinusoids over intervals of length t_{part} , we subdivide each horizon $[t_k - T, t_k]$ into n_{part} partitions of width t_{part} . We assume here that the horizon length T is a scalar multiple of t_{part} . With these partitions, the modified version of the ITSC EMHO estimates gains $\hat{I}_{q\zeta}^{(i)}$ and $\hat{I}_{d\zeta}^{(i)}$, $\zeta = a, b, c, f$, for each partition $i = 1, 2, \dots, n_{part}$ of $[t_k - T, t_k]$.

The partitioning of the interval $[t_k - T, t_k]$ is also used to simplify estimating the degree of fault $\sigma(t)$. From a physical prospective, the ITSC faults occur when there is a electrical short between two locations within a stator winding. This electrical insulation failure happens at specific points and tends to have a binary behavior, i.e., short or no short. Consequently, the degree of fault $\sigma(t)$ is expected to be piecewise constant. This is exploited by considering the estimate $\hat{\sigma}$ to be constant over each partition of the interval $[t_k - T, t_k]$.

Over each partition of $[t_k - T, t_k]$, the last row of (36) becomes an algebraic equality constraint on the fault current estimate with respect to the gains \hat{I}_{qf} and \hat{I}_{df} . This equality constraint is implemented in the simulation using a penalty function approach, i.e., adding a penalty function of the form

$$\int_{t_k-T}^{t_k} w_p \|\hat{v}_{fs}\|^2 dt, \quad (46)$$

to the cost function of (35). Here $w_p \in \mathbb{R}^+$ is a large weight and \hat{v}_{fs} is the last row of (36), i.e.

$$\hat{v}_{fs} = R_s \hat{i}_{fs} + \sigma^2 L \frac{d}{dt} \hat{i}_{fs} + \sigma M \frac{d}{dt} \hat{i}_{bs} + \sigma M \frac{d}{dt} \hat{i}_{cs} + \sigma(1 - \sigma) L \frac{d}{dt} \hat{i}_{as} + e_f, \quad (47)$$

with derivatives given in (45). Note that a feasible estimate for \hat{i}_{fs} will satisfy $\hat{v}_{fs} \equiv 0$. Any nonzero value \hat{v}_{fs} is penalized by the term in (46).

Another adaptation of the cost function in (35) is to add a positive definite weight matrix $Q \in \mathbb{R}^{6 \times 6}$ to weight the output tracking error $y^M - \hat{y}$. With Q , the observer can be tuned to place the largest weight on a set of outputs which most directly affects the observability of the degree of fault σ . The modified cost function then has the form

$$\int_{t_k-T}^{t_k} \left((y^M - \hat{y})^\top Q (y^M - \hat{y}) + w_p \|\hat{v}_{fs}\|^2 \right) dt. \quad (48)$$

Incorporating the above ideas into the cost function over each horizon $[t_k - T, t_k]$, the practical version of the ITSC EMHO is

$$\min_{\substack{\hat{I}_{q\zeta}^{(i)}, \hat{I}_{d\zeta}^{(i)}, \hat{\sigma}^{(i)} \\ \zeta=a,b,c,f \\ i=1, \dots, n_{part}}} \int_{t_k-T}^{t_k} \left((y^M - \hat{y})^\top Q (y^M - \hat{y}) + w_p \|\hat{v}_{fs}\|^2 \right) dt \quad (49)$$

subject to: (36)–(45), (47).

The superscript (i) denotes the i^{th} partition of $[t_k - T, t_k]$. The constraints (36)–(45), and (47) are understood to apply to each partition.

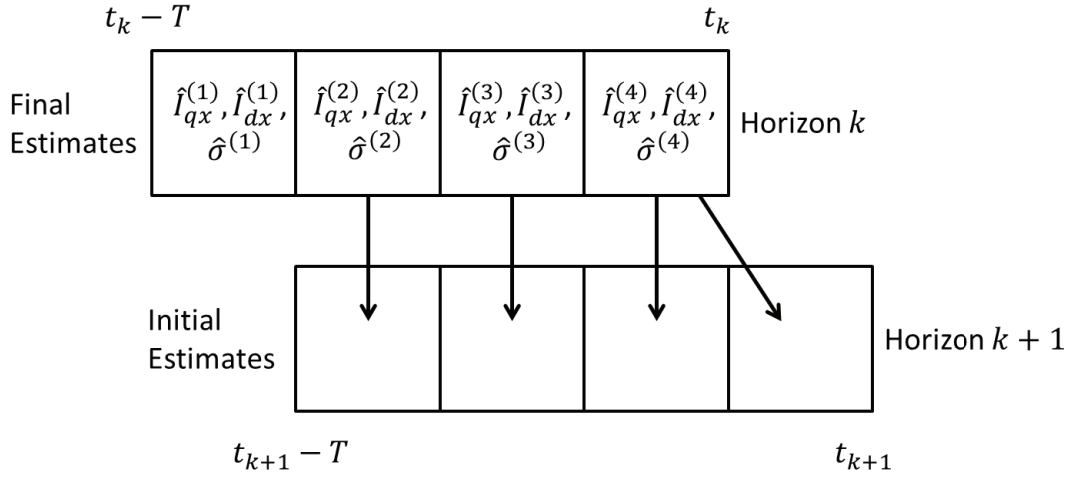


Fig. 10. This figure shows how the final estimates for partitions in the horizon $[t_k - T, t_k]$ are used as initial estimates for the horizon $[t_{k+1} - T, t_{k+1}]$.

Finally, to simplify the transition from one optimization problem to the next, the horizon is always uniformly shifted forward in time by t_{part} , i.e., $t_{k+1} = t_k + t_{part}$. This allows one last important modification to the ITSC EMHO concerning how estimates in preceding horizons are used to initialize or “hot-start” subsequent optimization problems. The scheme is illustrated in Figure 10. The method of partitioning each optimization horizon evenly has the advantage that estimates in some partitions of a previous horizon coincide with estimates of the current horizon. The partition $[t_{k+1} - t_{part}, t_{k+1}]$ does not coincide with the previous partition estimates. Thus, the estimate for $[t_k - t_{part}, t_k]$ is used to initialize the partition $[t_{k+1} - t_{part}, t_{k+1}]$ as shown in Figure 10.

VI. SIMULATION RESULTS

This section demonstrates the effectiveness of the ITSC EMHO. The three-phase SPMSM considered in this simulation has parameters given in Table I. The SPMSM is simulated over $[0, 1]$ according to the following scenario: i) the rotor speed is a constant $\omega_{rm} = 700$ rpm, ii) using current control the stator current (before and after fault) over $[0, 1]$ satisfies (current in Amperes)

$$\begin{aligned}
 i_{as} &= 50 \cos(\theta_r) \\
 i_{bs} &= 50 \cos(\theta_r - 2\pi/3) \\
 i_{cs} &= 50 \cos(\theta_r + 2\pi/3),
 \end{aligned} \tag{50}$$

and iii) a fault of severity σ_f occurs at $t_{fault} = 0.5s$, i.e. $\sigma(t) = 0$ for $t \in [0, 0.5)$ and $\sigma(t) = \sigma_f$ for $t \in [0.5, 1]$. The scenario is simulated in MATLAB R2014b to construct the outputs

$$y^M = \begin{bmatrix} v_{ab}^M & v_{bc}^M & v_{ca}^M & i_{as}^M & i_{bs}^M & i_{cs}^M \end{bmatrix}^\top,$$

where the line to line voltages $v_{ab} = v_{as} - v_{bs}$, $v_{bc} = v_{bs} - v_{cs}$, and $v_{ca} = v_{cs} - v_{as}$ are computed using (12) given that the stator currents satisfy (50). To simulate the fault current i_{fs} , the differential equation in the last line of (12) is integrated using the *ode23t* function in MATLAB with the default integration settings. For EMHO implementation, the output y^M is sampled at a rate of $dt = 0.1ms$.

TABLE I
SIMULATION AND SPMSM PARAMETERS

Variable	Symbol	Value
Self Inductance	L	2.31 mH
Mutual Inductance	M	-1.15 mH
Magnet Strength	λ_m	0.267 V·s
Stator Resistance	R_s	137 mΩ
Poles	n_p	8
Bus Voltage	V_{bus}	500 V
Rotor Speed	ω_{rm}	700 rpm
Fault Time	t_{fault}	0.5 s
Simulation Step Size	dt	0.1 ms

The simulated ITSC EMHO has a horizon $T = 50ms$ and two partitions of equal width, i.e. $t_{part} = 25ms$. The ITSC EMHO parameters are summarized in Table II. To emphasize tracking the line to line voltage equations over stator current tracking, a weighting matrix $Q \in \mathbb{R}^6$ is added to the cost function, i.e. the cost function is given by

$$\int_{t_1-T}^{t_1} (y^M(t) - \hat{y}(t))^\top Q (y^M(t) - \hat{y}(t)) dt, \quad (51)$$

where $Q = \text{diag}(10, 10, 10, 1, 1, 1)$. In addition, to enforce the constraint that \hat{i}_{fs} satisfies the last row of (12), we add to the cost function (51) a penalty function of the form

$$\int_{t_1-T}^{t_1} w_p \|\hat{v}_{fs}\|^2 dt,$$

where $w_p = 1000$ and \hat{v}_{fs} represents the last row on the right-hand side of (12), i.e.

$$\hat{v}_{fs} \triangleq \hat{\sigma} R_s \hat{i}_{fs} + \hat{\sigma}(1 - \hat{\sigma}) L \frac{d}{dt} \hat{i}_{as} + \hat{\sigma} M \frac{d}{dt} \hat{i}_{bs} + \hat{\sigma} M \frac{d}{dt} \hat{i}_{cs} + \hat{\sigma}^2 L \frac{d}{dt} \hat{i}_{fs} + e_f(\hat{\sigma}).$$

If \hat{i}_{abcf} and $\hat{\sigma}$ are consistent with (12), $\hat{v}_{fs} \equiv 0$. As described in Section V, the penalty function is used as an alternative method for enforcing this equality constraint.

TABLE II
ITSC EMHO PARAMETERS

Variable	Symbol	Value
Number of Partitions	n_{part}	2
Horizon Width	T	50ms
Partition Width	t_{part}	25ms

The estimation error for reconstructing the fault current, i.e. $|i_{fs} - \hat{i}_{fs}|$ is shown in Figure 11 for four different degrees of fault $\hat{\sigma}_f = 0.01, 0.02, 0.05, 0.1$. The error $|i_{fs} - \hat{i}_{fs}|$ is scaled by $\max(i_{fs})$ which represents the amplitude of the steady state fault current i_{fs} for each degree of fault $\hat{\sigma}_f$. The estimation error for reconstructing the degree of fault is shown in Figure 12 for each of the four different degrees of fault $\hat{\sigma}_f$. The estimation error for i_{as} , i_{bs} , and i_{cs} are not included since these are also measured variables and hence the estimation error is on the order of 10^{-6} (tolerance of the optimization).

It is clear from Figure 11, that after one partition of 25ms, the fault current estimate \hat{i}_{fs} is within 5% of the actual fault current i_{fs} . Similarly, the degree of fault estimation error is within 0.001 after one partition of 25ms as shown in Figure 12. This “bump” in the estimates right after the fault occurs is caused by an initial guess which is far from the new level of fault. However, the next optimization window improves the estimate of the degree of fault and fault current and converges quickly. The ability to improve on the previous estimates is a consequence of the manner in which estimates from previous partitions are used to “hot-start” subsequent partitions. The reader can recall that the initial states are passed from one partition to hot-start the next as illustrated in Figure 10.

The ITSC EMHO has additional applications beyond fault detection. One such application is fault-tolerant control schemes where the estimate for the degree of fault can be used to determine “safe” operating conditions after a fault has occurred. The next section explores a fault-tolerant power flow control application for a hybrid electric vehicle, such as the Toyota Prius. This fault detection scheme

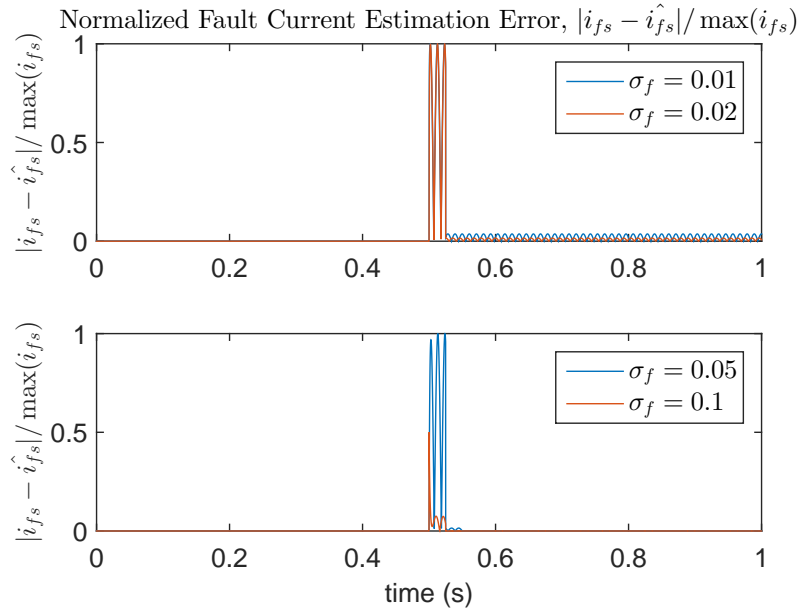


Fig. 11. The fault current reconstruction error $|i_{fs} - \hat{i}_{fs}|$ is simulated for four levels of fault, $\sigma_f = 0.01, 0.02, 0.05$, and 0.1 . The figure is normalized by $\max(i_{fs})$ which represents the magnitude of the steady state fault current i_{fs} for each degree of fault. In each simulation, the fault occurs at 0.5 s.

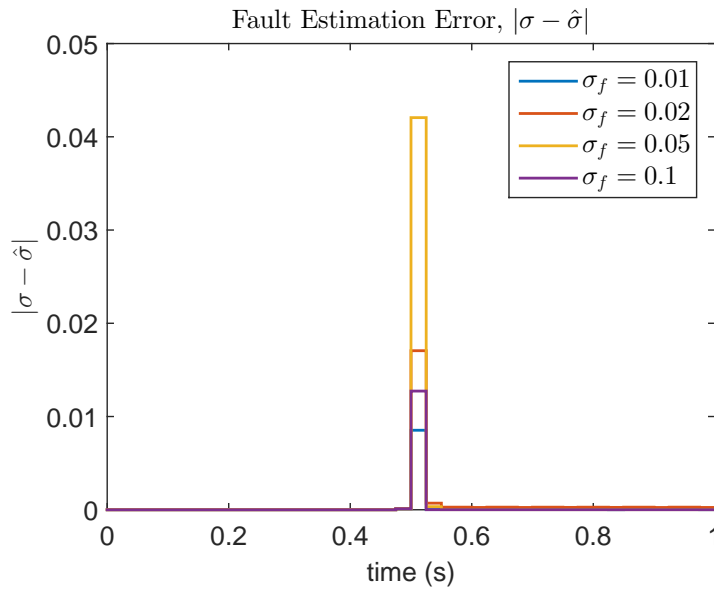


Fig. 12. The degree of fault reconstruction error $|\sigma - \hat{\sigma}|$ is simulated for four levels of fault, $\sigma_f = 0.01, 0.02, 0.05$, and 0.1 . In each simulation, the fault occurs at 0.5 s.

also has applications for both fault detection and fault mitigating control in heavy hybrid vehicles. The application to heavy hybrid vehicles is discussed in Section VIII.

VII. APPLICATION: HIGH LEVEL POWER FLOW OPTIMIZATION

Once a fault and fault level are identified, along with the fault current \hat{i}_{fs} , the next objective is to develop fault mitigation controller strategies that allow the hybrid vehicle (of which the SPMSM is an integral part) to continue to function albeit at a substantially reduced operational level. This section considers fault mitigation strategies for a 2004 Toyota Prius. The strategies set forth herein can be scaled up for large earth movers such as the Deere 644K hybrid wheel loader. Fault mitigation is carried out at the so-called supervisory level. A supervisory level controller coordinates vehicle control by determining optimized power flows to the individual subsystems such as was explored in [6], [7], and [8]. For example, for a diverse set of situations, the supervisory level controller would determine how best to utilize the electric drive system in coordination with the internal combustion engine (ICE) to meet driving objectives. For efficient and feasible numerical optimization strategies, supervisory level subsystem models are power-flow based; specifically, the subsystem models are low granularity power flow component models that utilize efficiency maps as opposed to high granularity models based on the underlying physics. In the case of the SPMSM, such an efficiency map depends on whether or not the motor has a fault as well as on the degree of fault. Another advantage of the “online” supervisory level control is that it can adapt the controls to different fault levels as they occur without requiring an exhaustive library of precomputed controls.

This section will briefly describe i) the hybrid supervisory control problem in the Toyota Prius, ii) constructing efficiency maps and constraints for a SPMSM with ITSC faults and iii) using an embedded optimal controller for high-level power flow control.

A. Prius Supervisory Level Powertrain Description

The hybrid powertrain architecture of the 2004 Toyota Prius is shown in Figure 13. This powertrain has two electric drives: one is for generation and engine starting, labeled “SPMSM1”, with a maximum mechanical power of 30 kW and the other is for traction and regeneration, labeled “SPMSM2”, with a

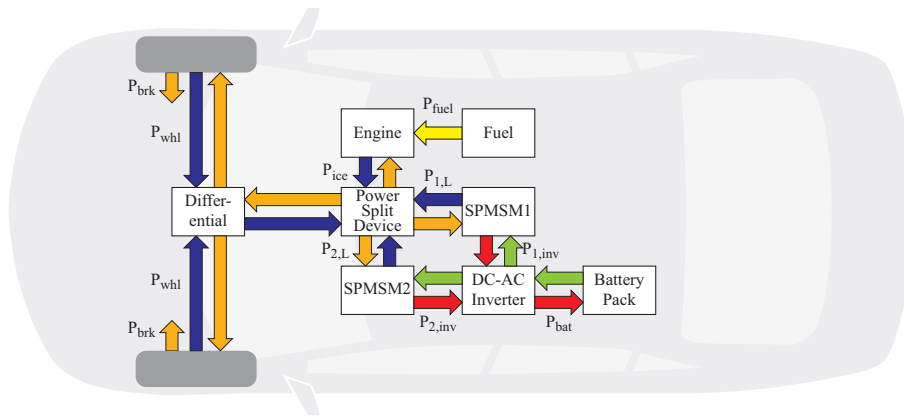


Fig. 13. The Toyota Prius architecture has different modes of operation. The “traction” SPMSM and the “generator” SPMSM can convert electrical energy to mechanical energy, or vice versa. The efficiency maps differ for each of the directions of energy conversion. The combinations of generating and propelling of the SPMSM can be used to construct a finite set of modes of operation. The supervisory power-flow controller determines which mode of operation and which control action is optimal.

maximum mechanical power of 50 kW. The traction and generator SPMSMs⁴ in this architecture are energy conversion devices: mechanical to electrical and vice-versa. The powertrain includes the aforementioned PMSMs, a 57 kW Atkinson-cycle ICE, a 21 kW Nickel Metal Hydride (NiMH) battery pack, and a power split device consisting of a planetary gear system that connects the power flow pathways of the ICE and SPMSMs.

Due to differing efficiency maps for SPMSM propelling and generating, the Prius architecture is modeled as a switched system with a finite set of “modes of operation.” Each mode represents a fixed configuration of power flow directions. Powertrain operation has four modes, denoting the direction of power flow:

- 1) SPMSM1 propelling (ICE start-up)-SPMSM2 propelling-battery discharging-ICE off;
- 2) SPMSM1 generating-SPMSM2 propelling-battery discharging-ICE on;
- 3) SPMSM1 generating-SPMSM2 propelling-battery charging-ICE on;
- 4) SPMSM1 generating-SPMSM2 generating-battery charging-ICE on or off.

Each mode of operation will potentially utilize different efficiency maps and dynamics.

In the remainder of this report, we will consider an ITSC fault only occurring in SPMSM2, i.e., no

⁴The 2004 Toyota Prius uses two interior PMSMs (IPMSM). In this work, we consider SPMSMs with comparable power capabilities. Using SPMSMs allows one to use the developed ITSC fault models. In contrast, the IPMSM has a more complex model, which is beyond the scope of this report. Nevertheless, this report serves as a baseline for any future work which uses IPMSMs.

faults occur in SPMSM1. We begin with SPMSM1 which does not have fault. The supervisory-level power flow model for SPMSM2 before and after an ITSC fault is developed in Section VII-C. Supervisory-level power flow models are constructed for the ICE, battery, vehicle, power split device, and electrical bus in Appendix C. Also, Appendix C describes the interconnection structure and other modeling issues associated with the Prius.

B. Power Flow Model for SPMSM1

Since SPMSM1 is without fault, there are only two modes: propelling and generating. SPMSM1 has parameters listed in Table III. For supervisory control in the propelling mode, we consider the inverter-supplied power P_{inv} to be the input and electromagnetic load power $P_L = P_a + P_b + P_c$ to be the output of the power flow component model for SPMSM1. Implicitly, at the supervisory level SPMSM1 is simply viewed as an algebraic input-output device without regard to specific phase information. Conversely in the generating mode, we consider P_L to be the input and P_{inv} to be output of the power flow component model for SPMSM1. The dynamics of the SPMSM are not included at the supervisory level since the time constants are significantly faster than the associated mechanical components of the vehicle.

TABLE III
SPMSM1 PARAMETERS

Variable	Symbol	Value
Self Inductance	L	0.1899 mH
Mutual Inductance	M	-0.09497 mH
Magnet Strength	λ_m	113 mV·s
Stator Resistance	R_s	39.81 mΩ
Poles	n_p	8

We will focus first on modeling SPMSM1 in the propelling mode as an input-output efficiency map:

$$P_L = \eta_{SPMSM1,prop}(\omega_{rm}, P_{inv})P_{inv} \quad (52)$$

Similarly, in the generating mode SPMSM1 interchanges the inputs and outputs of (52), in which case:

$$P_{inv} = \eta_{SPMSM1,gen}(\omega_{rm}, P_L)P_L \quad (53)$$

The efficiencies in (52) and (53) are approximated using the following pair of quadratic equations:

$$\eta_{SPMSM1,prop} = a_1 + b_1\omega_{sc} + c_1\omega_{sc}^2 + d_1P_{inv,sc} + e_1w_{sc}P_{inv,sc} \quad (54)$$

$$\eta_{SPMSM1,gen} = a_2 + b_2\omega_{sc} + c_2\omega_{sc}^2 + d_2P_{L,sc} + e_2w_{sc}P_{L,sc}, \quad (55)$$

where the ‘sc’ subscript denotes a scaled variable with scaling given by

$$\omega_{sc} = \omega_{rm}/6000 \quad (56)$$

$$P_{inv,sc} = P_{inv}/50000 \quad (57)$$

$$P_{L,sc} = P_L/50000. \quad (58)$$

The optimal coefficients for the computed curve fit is shown in Table IV. The methodology for determining these coefficients will be described in Section VII-B1.

TABLE IV
SPMSM1 CURVE FIT

Parameter	a	b	c	d	e	R-square Error
Propelling	0.9296	0.2191	-0.1648	-0.1969	0.2227	0.9985
Generating	0.941	0.2243	-0.175	0.2759	-0.2843	0.9991

1) *Determination of Efficiency Model Coefficients:* The power conversion and efficiency of the SPMSM in either mode (propelling or generating) depends on the inverter control action and the mechanical rotor speed $\omega_{rm} = \frac{\omega_r}{n_p}$. Specifically, the efficiency of the SPMSM depends on the inverter-supplied voltages v_{ag} , v_{bg} , and v_{cg} which drive the stator currents i_{as} , i_{bs} , and i_{cs} as per (5) included here for convenience in (59) and (60):

$$\begin{bmatrix} v_{as} \\ v_{bs} \\ v_{cs} \end{bmatrix} = \begin{bmatrix} R_s & 0 & 0 \\ 0 & R_s & 0 \\ 0 & 0 & R_s \end{bmatrix} \begin{bmatrix} i_{as} \\ i_{bs} \\ i_{cs} \end{bmatrix} + \begin{bmatrix} L & M & M \\ M & L & M \\ M & M & L \end{bmatrix} \frac{d}{dt} \begin{bmatrix} i_{as} \\ i_{bs} \\ i_{cs} \end{bmatrix} + \begin{bmatrix} e_a \\ e_b \\ e_c \end{bmatrix}, \quad (59)$$

where

$$\begin{bmatrix} e_a \\ e_b \\ e_c \end{bmatrix} = \omega_r \lambda_m \begin{bmatrix} \cos(\theta_r) \\ \cos(\theta_r - 2\pi/3) \\ \cos(\theta_r + 2\pi/3) \end{bmatrix}. \quad (60)$$

Using the steps outlined in Section II, the relationship between the inverter-supplied power and electromagnetic power expressed in matrix form is given by

$$\begin{bmatrix} P_{inv,a} \\ P_{inv,b} \\ P_{inv,c} \end{bmatrix} = \begin{bmatrix} R_s & 0 & 0 \\ 0 & R_s & 0 \\ 0 & 0 & R_s \end{bmatrix} \begin{bmatrix} i_{as}^2 \\ i_{bs}^2 \\ i_{cs}^2 \end{bmatrix} + \begin{bmatrix} i_{as} & 0 & 0 \\ 0 & i_{bs} & 0 \\ 0 & 0 & i_{cs} \end{bmatrix} \begin{bmatrix} L & M & M \\ M & L & M \\ M & M & L \end{bmatrix} \frac{d}{dt} \begin{bmatrix} i_{as} \\ i_{bs} \\ i_{cs} \end{bmatrix} + \begin{bmatrix} P_a \\ P_b \\ P_c \end{bmatrix} \quad (61)$$

where $P_\zeta \triangleq e_\zeta i_{\zeta s}$, $\zeta = a, b, c$. The total power supplied by the inverter is $P_{inv} \triangleq P_{inv,a} + P_{inv,b} + P_{inv,c}$.

Hence by conservation of power,

$$P_{inv} = R_s i_{as}^2 + R_s i_{bs}^2 + R_s i_{cs}^2 + \frac{d}{dt} \Upsilon + P_L, \quad (62)$$

where the quantity

$$\Upsilon = \frac{1}{2} \begin{bmatrix} i_{as} & i_{bs} & i_{cs} \end{bmatrix} \begin{bmatrix} L & M & M \\ M & L & M \\ M & M & L \end{bmatrix} \begin{bmatrix} i_{as} \\ i_{bs} \\ i_{cs} \end{bmatrix} \quad (63)$$

is a Lyapunov-like energy function.

It is clear from (62) that the relationship between P_{inv} and P_L depends on the stator currents $i_{\zeta s}$, $\zeta = a, b, c$. We will consider the local controller to utilize current control, i.e., the stator currents $i_{\zeta s}$ are the controlled inputs. We assume controlled stator currents have the form

$$\begin{aligned} i_{as} &= I_q \cos(\theta_r) + I_d \sin(\theta_r) \\ i_{bs} &= I_q \cos\left(\theta_r - \frac{2\pi}{3}\right) + I_d \sin\left(\theta_r - \frac{2\pi}{3}\right) \\ i_{cs} &= I_q \cos\left(\theta_r + \frac{2\pi}{3}\right) + I_d \sin\left(\theta_r + \frac{2\pi}{3}\right). \end{aligned} \quad (64)$$

For a given speed ω_r , a given set of stator currents $i_{\zeta s}$, $\zeta = a, b, c$, and a given power command (P_L if propelling and P_{inv} if generating) the required stator voltages $v_{\zeta s}$ are determined by (59): these voltages set up the desired stator currents $i_{\zeta s}$ given in (64). In the propelling case, the goal is to find the minimum level of current injection $i_{\zeta s}$ that meets the required output power and similarly in the generating case. This is equivalent to maximum torque per amp control strategies [1], [20], [21]. Given the form of (64), this is further equivalent to choosing the appropriate levels for I_d and I_q .

To compute the optimal I_q and I_d levels, we pose a constrained optimization problem. The physical constraints for feasible controls include i) the thermal/current constraint on each phase $P_{therm} = R_s I_{max}^2 \geq$

$R_s(I_q^2 + I_d^2)$, ii) the line to line voltage constraints $|v_{\zeta s} - v_{\eta s}| \leq V_{dc}$ for $\zeta \neq \eta \in \{a, b, c\}$, and iii) the voltage constraint $|v_{\zeta s}| \leq \frac{2}{3}V_{dc}$ where V_{dc} is the DC link voltage. For reference these constraints are restated below.

$$P_{therm} = R_s I_{max}^2 \geq R_s (I_q^2 + I_d^2) \quad (65)$$

$$|v_{\zeta s} - v_{\eta s}| \leq V_{dc} \text{ for } \zeta \neq \eta \in \{a, b, c\} \quad (66)$$

$$|v_{\zeta s}| \leq \frac{2}{3}V_{dc} \text{ for } \zeta \in \{a, b, c\}. \quad (67)$$

Note, we assume that the maximum current I_{max} in each phase is what determines the maximum thermal constraint on the stator windings as per (65). We can now pose the aforementioned optimization problem to determine an optimal feasible control for each speed ω_{rm} and commanded power (P_L if propelling and P_{inv} if generating):

$$\begin{aligned} & \min_{I_d, I_q \in \mathbb{R}} I_d^2 + I_q^2 \\ & \text{subject to: (59)-(67), and} \end{aligned} \quad (68)$$

$$P_L \geq P_L^* \text{ if propelling or}$$

$$P_{inv} \leq P_{inv}^* < 0 \text{ if generating}$$

The optimization in (68) is solved in MATLAB R2014b using the *fmincon* constrained optimization program.

Given the optimal I_d and I_q for each speed ω_{rm} and power command (P_L or P_{inv}), the efficiencies are computed as per

$$\eta_{SPMSM1,prop} = P_L / P_{inv} \quad (69)$$

and

$$\eta_{SPMSM1,gen} = P_{inv} / P_L \quad (70)$$

The computed efficiency of SPMSM1 in propelling and generating modes are shown in Figures 14 and 15, respectively.

The last step is to construct curve fits to the efficiency maps in Figures 14 and 15 for use at the supervisory level when determining power flow control strategies. The approach is to select a representative subset of data points from Figures 14 and 15. These representative points are distributed in order to evenly

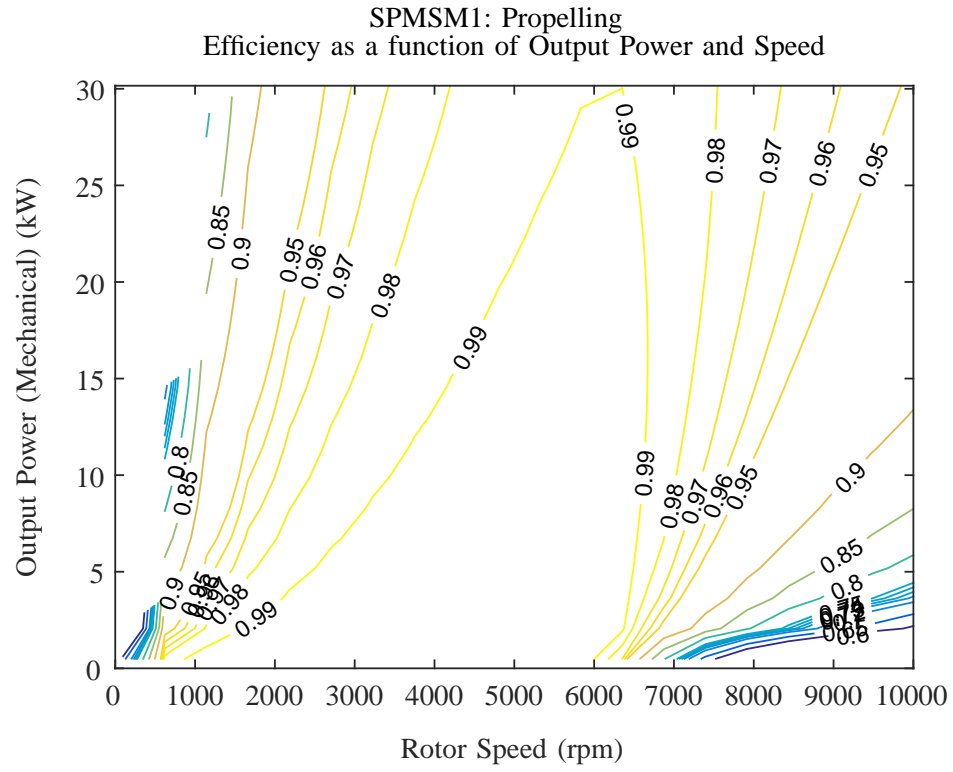


Fig. 14. Efficiency plot for the unfaulted SPMSM1 in propelling mode with parameters in Table III.

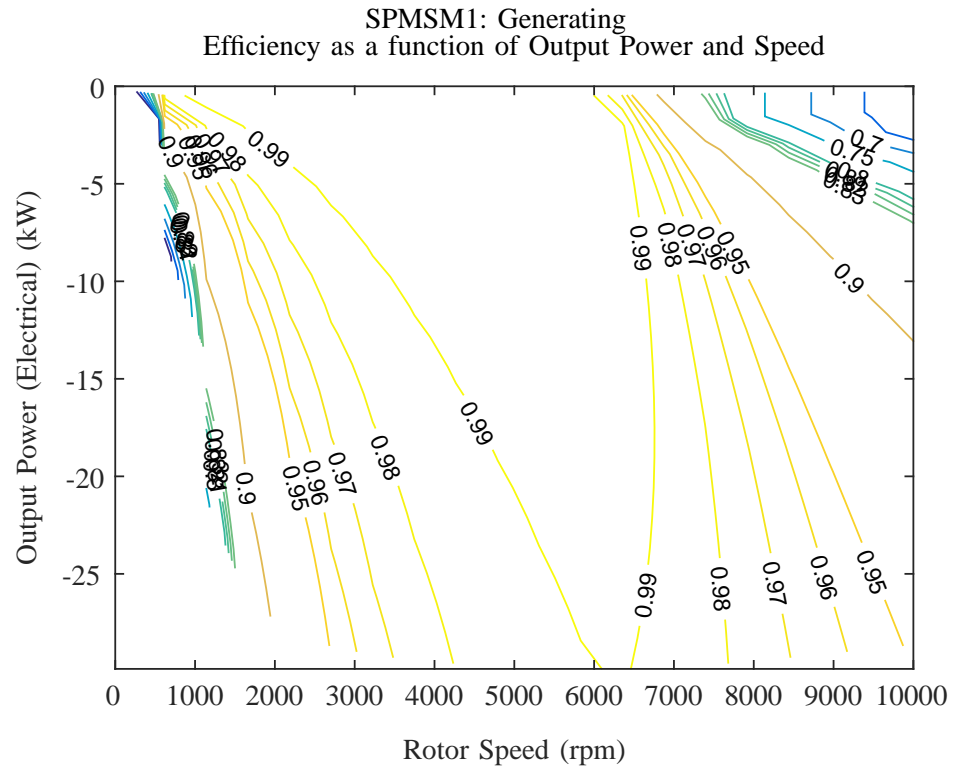


Fig. 15. Efficiency plot for the unfaulted SPMSM1 in generating mode with parameters in Table III.

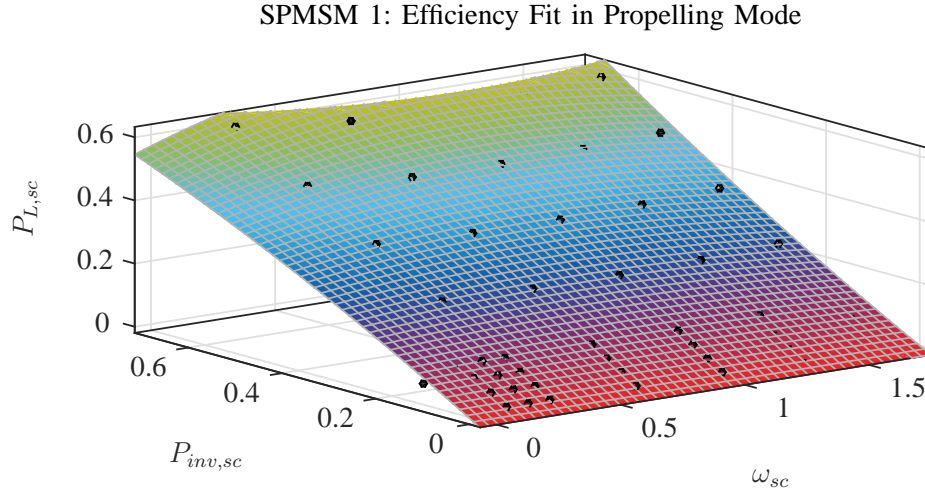


Fig. 16. Surface fit for SPMSM1 in propelling mode. The black dots represent simulated tuples $(\omega_{sc}, P_{inv,sc}, P_{L,sc})$. The curve fit has the form $P_{L,sc} = \eta_{SPMSM1,prop} P_{inv,sc}$, where the efficiency $\eta_{SPMSM1,prop}$ has the form in (54).

balance the fit accuracy over the operating region, i.e., for regions of greater curvature more sample points are needed. Given the chosen approximating functions in (54) and (55), we perform an optimization problem with respect to the coefficients $(a_i, b_i, c_i, d_i, e_i)$ to minimize the least-squares error between the fits and the two sets of data points (one for propelling and one for generating). The curve fit was computed using the Curve Fitting Toolbox in MATLAB R2014b. The fit for SPMSM1 in propelling mode is shown in Figure 16. The resulting optimal coefficients are included in Table IV. These efficiency functions are part of the supervisory level power flow model.

C. Power Flow Model for SPMSM2: With and Without ITSC Fault

SPMSM2 is the primary traction motor in the Toyota Prius. The parameters for SPMSM2 are given in Table V. Since SPMSM2 is subject to an ITSC fault, the efficiency maps in both the propelling and generating modes are also functions of the degree of fault σ . Specifically, the efficiency maps in the propelling and generating modes for each degree of fault σ are assumed to have the form

$$\eta_{SPMSM2,prop}(\omega_{sc}, P_{inv,sc}, \sigma) = P_L / P_{inv} \quad (71)$$

$$\cong a_1(\sigma) + b_1(\sigma)\omega_{sc} + c_1(\sigma)\omega_{sc}^2 + d_1(\sigma)P_{inv,sc} + e_1(\sigma)\omega_{sc}P_{inv,sc} \quad (72)$$

$$\eta_{SPMSM2,gen}(\omega_{sc}, P_{L,sc}, \sigma) = P_{inv} / P_L \quad (73)$$

$$\cong a_2(\sigma) + b_2(\sigma)\omega_{sc} + c_2(\sigma)\omega_{sc}^2 + d_2(\sigma)P_{L,sc} + e_2(\sigma)\omega_{sc}P_{L,sc}, \quad (74)$$

where the ‘sc’ subscript denotes a scaled variable with scaling given by

$$\omega_{sc} = \omega_{rm}/6000 \quad (75)$$

$$P_{inv,sc} = P_{inv}/50000 \quad (76)$$

$$P_{L,sc} = P_L/50000. \quad (77)$$

As described in the preceding subsection, computing the optimal efficiency for a given speed ω_{rm} and power command (P_L in propelling and P_{inv} in generating) depends on the local level control. Optimal local level controls⁵ and the associated efficiency maps for a set of degrees of fault $\sigma \in \{0, 0.005, 0.01, 0.02, 0.05\}$ are computed. This set of degrees of fault is chosen as a representative sample of the range of degrees of fault for which fault-tolerant control is both feasible and safe. The optimal coefficient values for the fits in (72) and (74) are given in Table VI.

TABLE V
SPMSM2 PARAMETERS

Variable	Symbol	Value
Self Inductance	L	0.21407 mH
Mutual Inductance	M	-0.10703 mH
Magnet Strength	λ_m	184 mV·s
Stator Resistance	R_s	30.5 mΩ
Poles	n_p	8

1) Determination of Efficiency Model Coefficients: When no ITSC fault is present in SPMSM2, the optimization problem in (68) can be used to generate efficiency maps for both the propelling and generating modes. The associated efficiency maps without ITSC fault are shown in Figures 17 and 18.

As mentioned previously, we will construct efficiency maps for a select number of degrees of fault, i.e., $\sigma \in \{0, 0.005, 0.01, 0.02, 0.05\}$. The presence of an ITSC fault represents an uncontrolled or autonomous switch within the supervisory control model. When an ITSC fault is detected by the ITSC EMHO described in Sections IV and V, the supervisory controller is alerted to the new mode for the supervisory control model. The estimated degree of fault is used to determine which efficiency map is applicable at the supervisory level. As mentioned in Section VII-B, with these efficiency maps for each degree of fault,

⁵Pre-fault this is maximum torque per amp control and post-fault minimizes commanded current losses.

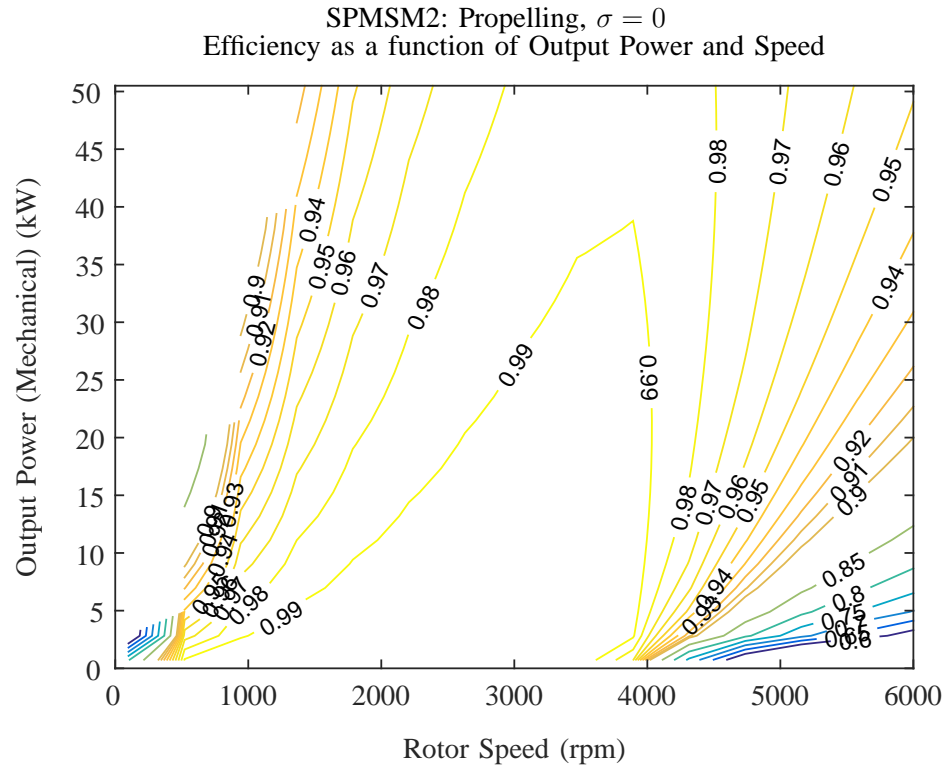


Fig. 17. Efficiency plot for the unfaulted SPMSM2 in propelling mode with parameters in Table V.

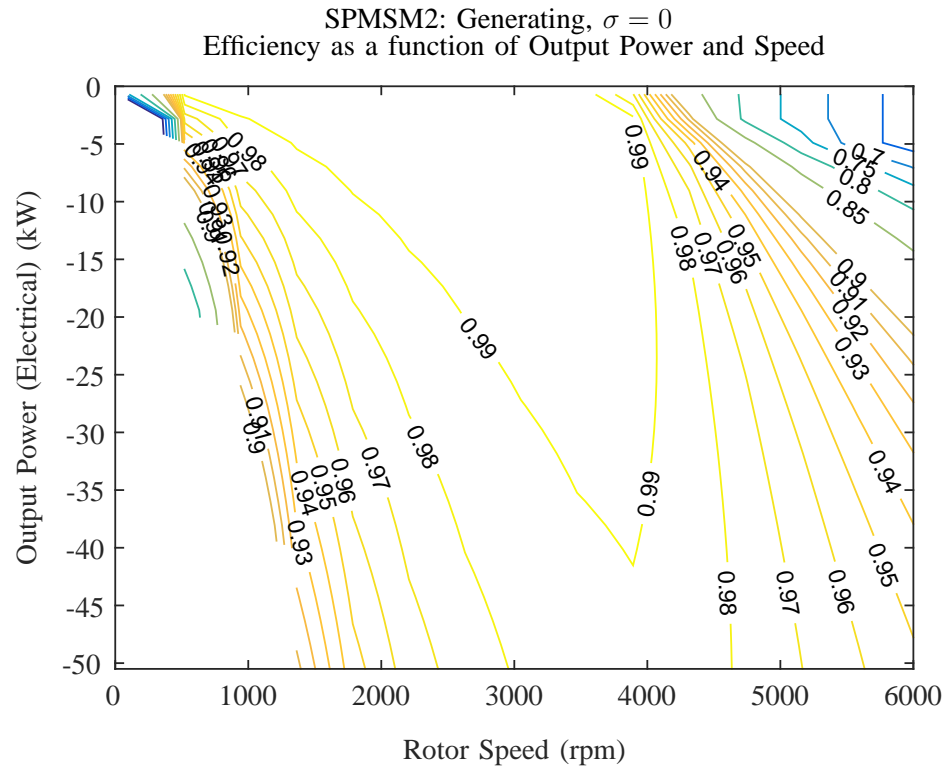


Fig. 18. Efficiency plot for the unfaulted SPMSM2 in generating mode with parameters in Table V.

TABLE VI
SPMSM2 CURVE FIT

Parameter	Deg of fault σ	a	b	c	d	e	R-square Error
Propelling	0	0.8903	0.4123	-0.4701	-0.0906	0.2086	0.9985
	0.005	0.6983	3.411	-11.05	-0.337	1.476	0.9985
	0.01	0.7917	3.624	-28.67	-1.894	23.13	0.9964
	0.02	0.9296	0.2191	-0.1648	-0.1969	0.2227	0.9985
	0.05	0.5619	14.44	-158.4	-2.412	33.52	0.9976
Generating	0	0.9215	0.3676	-0.4195	0.1217	-0.2032	0.9995
	0.005	0.5709	5.475	-18.56	0.7304	-3.514	0.9963
	0.01	0.7302	4.732	-26.14	1.771	-13.57	0.9942
	0.02	0.3138	18.33	-123	3.585	-37.28	0.9961
	0.05	0.3327	26.34	-323.5	9.353	-154.9	0.9865

there is a feasible and safe local control action stored in a lookup table. We first discuss how these efficiency maps and local control actions can be constructed.

When an ITSC fault is detected within the stator winding, stopping the vehicle immediately can be the safest course of action. However, it is possible to operate the vehicle in a reduced capacity if the degree of ITSC fault is sufficiently small. Given an estimate of the degree of fault $\hat{\sigma}$, we need to determine admissible control actions and efficiency curves so the supervisory controller can safely operate the vehicle.

From (17) we can relate inverter supplied power P_{inv} to the load power $P_L \triangleq P_a + P_b + P_c + P_f$ as

$$P_{inv} = (1 - \sigma)R_s i_{as}^2 + R_s i_{bs}^2 + R_s i_{cs}^2 + \sigma R_s i_{fs}^2 + \frac{d}{dt} \Upsilon_f(\sigma) + P_L \quad (78)$$

where $\Upsilon(\sigma)$ is defined in (17). Resistive losses are the primary source of energy loss. The approach to computing the efficiency curves and constraints is to solve a constrained optimization problem.

After an ITSC fault we will still consider balanced three-phase current control because traditional PMSM motor design does not have a tap to neutral which would allow independent phase current control. Controlling the current in each phase independently would allow for a larger family of fault mitigating

control actions. Specifically, balanced current control has the form

$$\begin{aligned} i_{as} &= I_q \cos(\theta_r) + I_d \sin(\theta_r) \\ i_{bs} &= I_q \cos\left(\theta_r - \frac{2\pi}{3}\right) + I_d \sin\left(\theta_r - \frac{2\pi}{3}\right) \\ i_{cs} &= I_q \cos\left(\theta_r + \frac{2\pi}{3}\right) + I_d \sin\left(\theta_r + \frac{2\pi}{3}\right). \end{aligned} \quad (79)$$

The control problem with balanced three-phase current is to find the gains I_q and I_d that optimize efficiency, satisfy physical constraints, and achieve a desired power load (P_L for the motor and P_{inv} for the generator) at a fixed speed $\omega_{rm} = \omega_r/n_p$ and degree of fault σ . There are several physical constraints we must include in the optimization to determine feasible post-fault controls: i) thermal cooling limits for each phase, P_{therm} , ii) inverter voltage constraints, iii) maximum stator current limits I_{max} , and iv) conservation laws such Kirchoff's current law. These constraints can be expressed as

$$P_{therm} \geq (1 - \sigma)R_s i_{as}^2 + \sigma R_s i_{fs}^2 \quad (80)$$

$$|v_{xs} - v_{ys}| \leq V_{dc}, \quad x \neq y \in \{a, b, c\} \quad (81)$$

$$|v_{xs}| \leq \frac{2}{3}V_{dc}, \quad x \in \{a, b, c\} \quad (82)$$

$$I_{max}^2 \geq I_q^2 + I_d^2 \quad (83)$$

$$0 = i_{as} + i_{bs} + i_{cs}. \quad (84)$$

Note, the thermal constraint $P_{therm} \geq (1 - \sigma)R_s i_{as}^2 + \sigma R_s i_{fs}^2$ only applies to the faulted phase as the current constraint $I_{max}^2 \geq I_q^2 + I_d^2$ will guarantee thermal constraints are satisfied in the other healthy phases. In addition, the thermal constraint (80) assumes that the stator will uniformly distribute the heat generated by phase-a and the eddy loop, i.e., we assume that even if the eddy loop generates more heat in a small area, the maximum thermal power dissipated, P_{therm} , still applies. This simplification is not a precise representation of the physics, but will provide a simplified model for precomputing fault-tolerant control.

The additional constraint on the optimization problem is for the commanded output power (P_L or P_{inv}) to equal to the desired output power (P_L^* or P_{inv}^*); it will be equivalent to satisfy $P_L \geq P_L^*$ or $P_{inv} \leq P_{inv}^* < 0$. For each mechanical rotor speed ω_{rm} , each commanded power P_L^* , and degree of fault

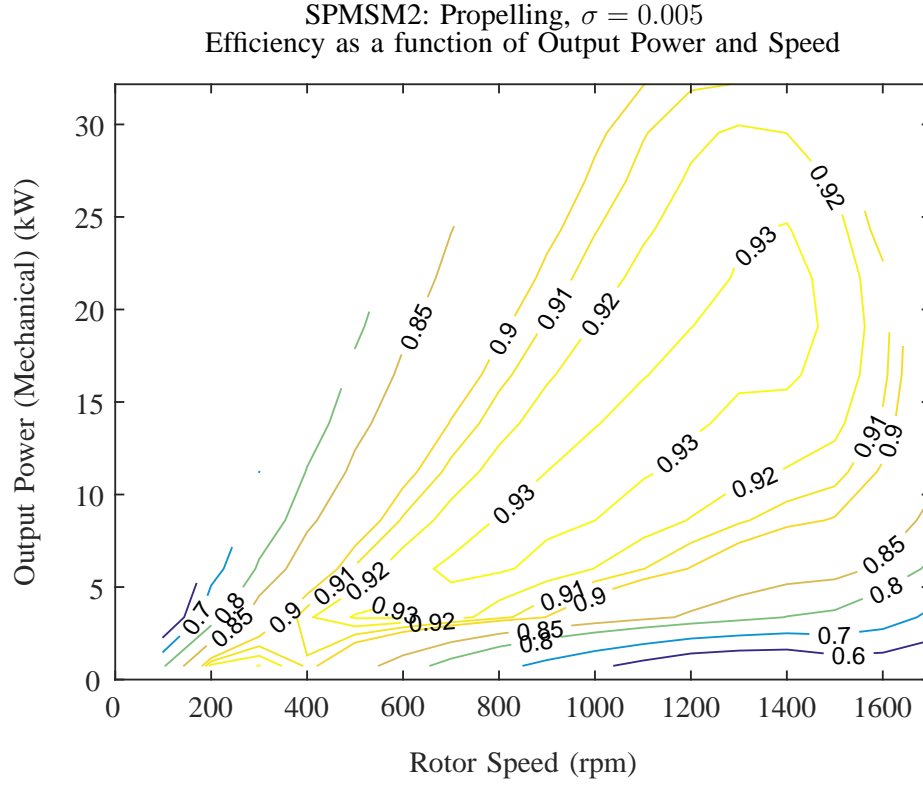


Fig. 19. Efficiency plot for SPMSM2 in propelling mode with degree of fault $\sigma = 0.005$ and parameters in Table V.

σ , the optimization problem is given by

$$\min_{I_d, I_q \in \mathbb{R}} I_d^2 + I_q^2 \quad (85)$$

subject to: (12), (78)-(84), and

$$P_L \geq P_L^* \text{ if propelling} \quad (86)$$

$$P_{inv} \leq P_{inv}^* < 0 \text{ if generating} \quad (87)$$

If there is no feasible solution for a given speed ω_{rm} , power command (P_L^* or P_{inv}), and degree of fault σ , then this operating point is excluded from the set of admissible power commands. The optimization problem in (85) is used to construct a table of feasible solutions, optimal I_d and I_q commands, and efficiency values for a family of speeds ω_{rm} , power commands P_L^* , and degrees of fault $\sigma \in \{0, 0.005, 0.01, 0.02, 0.05\}$. The efficiency curves for each degree of fault are contained in Figures 19-26.

Once the feasible controls are found, one can use approximate the surface of the efficiency curves to construct a simplified efficiency function $\eta_{SPMSM2,prop}$ or $\eta_{SPMSM2,gen}$ for supervisory level control, as

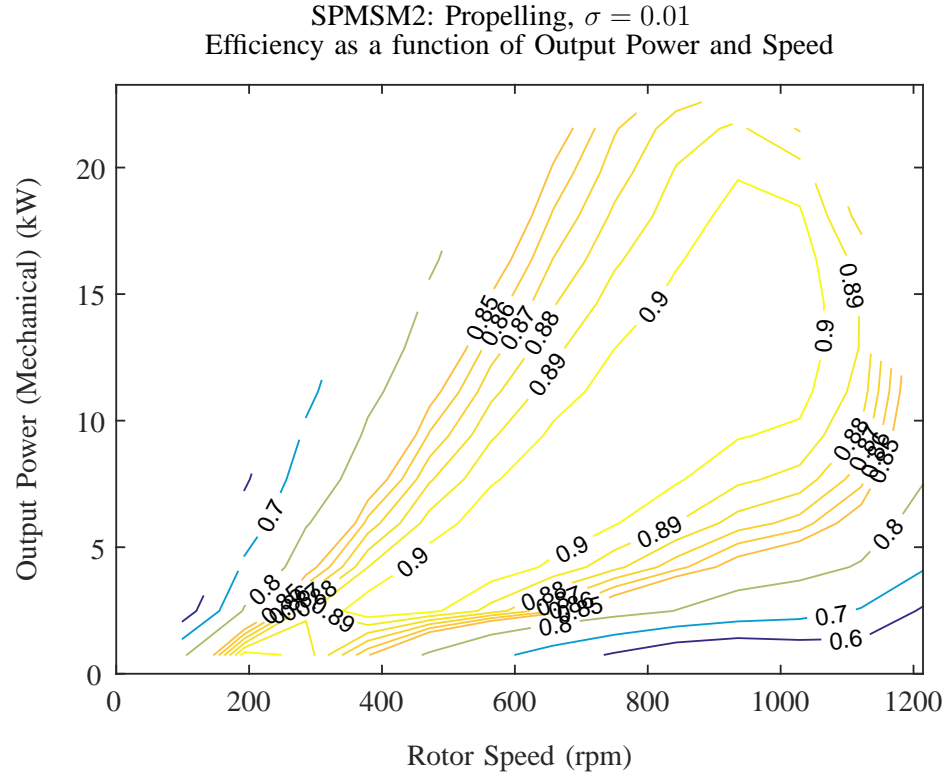


Fig. 20. Efficiency plot for SPMSM2 in propelling mode with degree of fault $\sigma = 0.01$ and parameters in Table V.

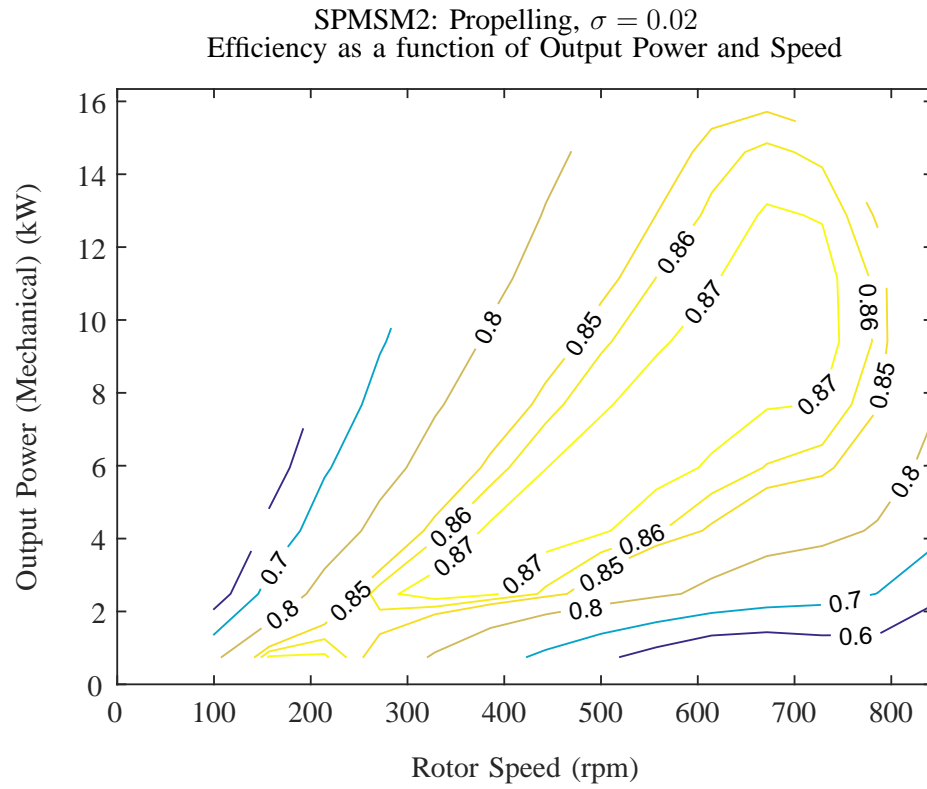


Fig. 21. Efficiency plot for SPMSM2 in propelling mode with degree of fault $\sigma = 0.02$ and parameters in Table V.

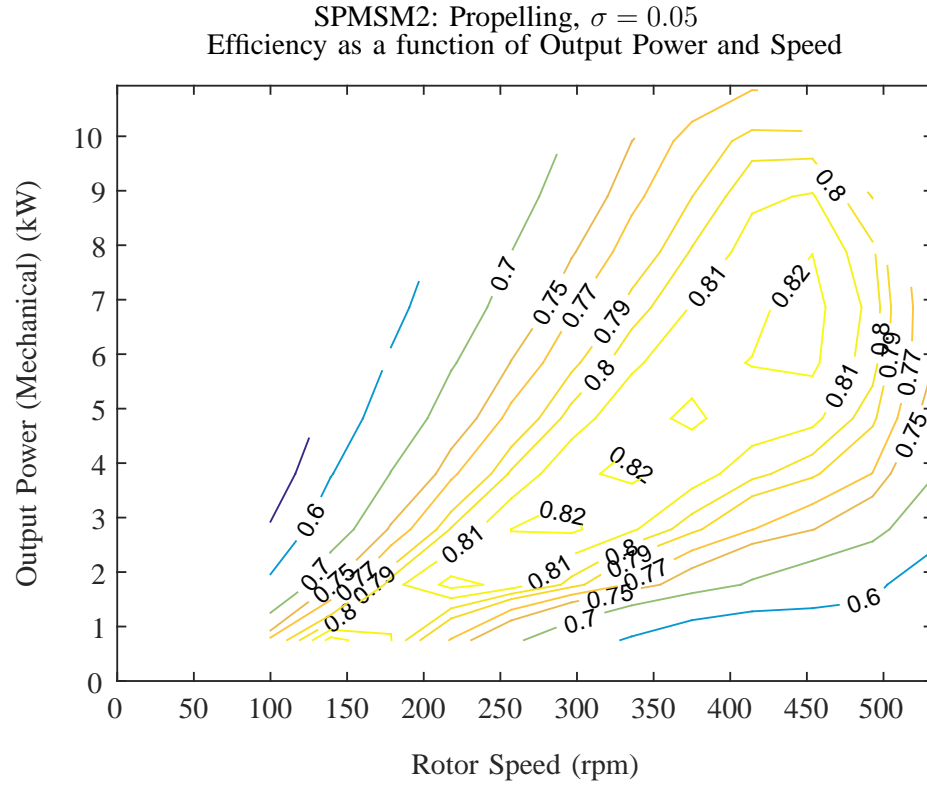


Fig. 22. Efficiency plot for SPMSM2 in propelling mode with degree of fault $\sigma = 0.05$ and parameters in Table V.

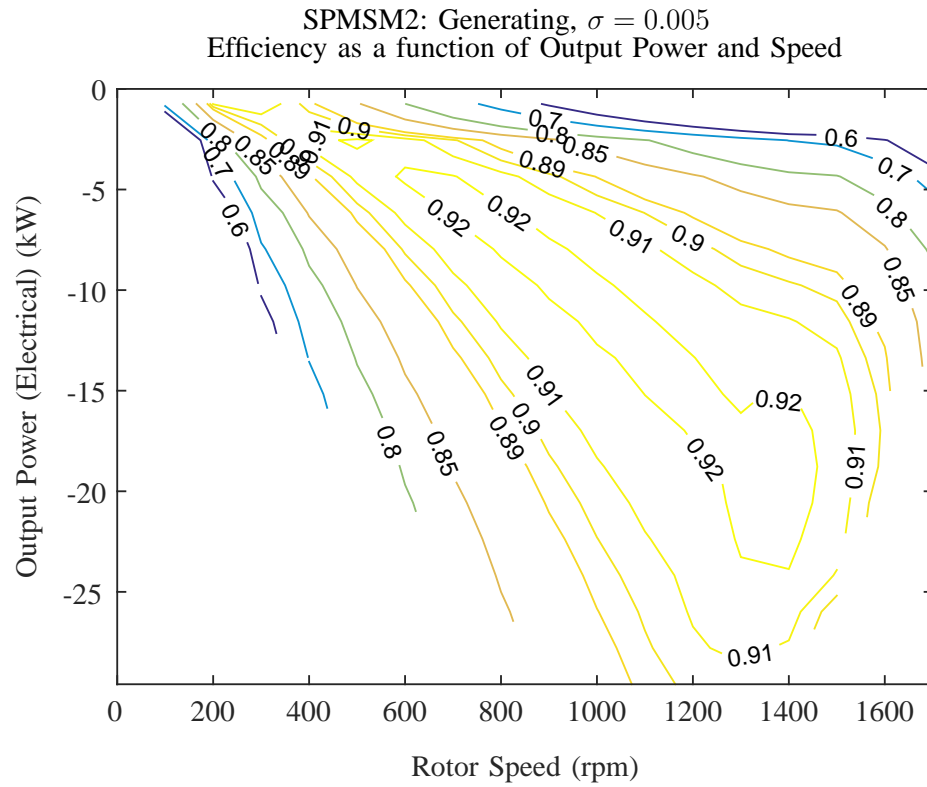


Fig. 23. Efficiency plot for SPMSM2 in generating mode with degree of fault $\sigma = 0.005$ and parameters in Table V.

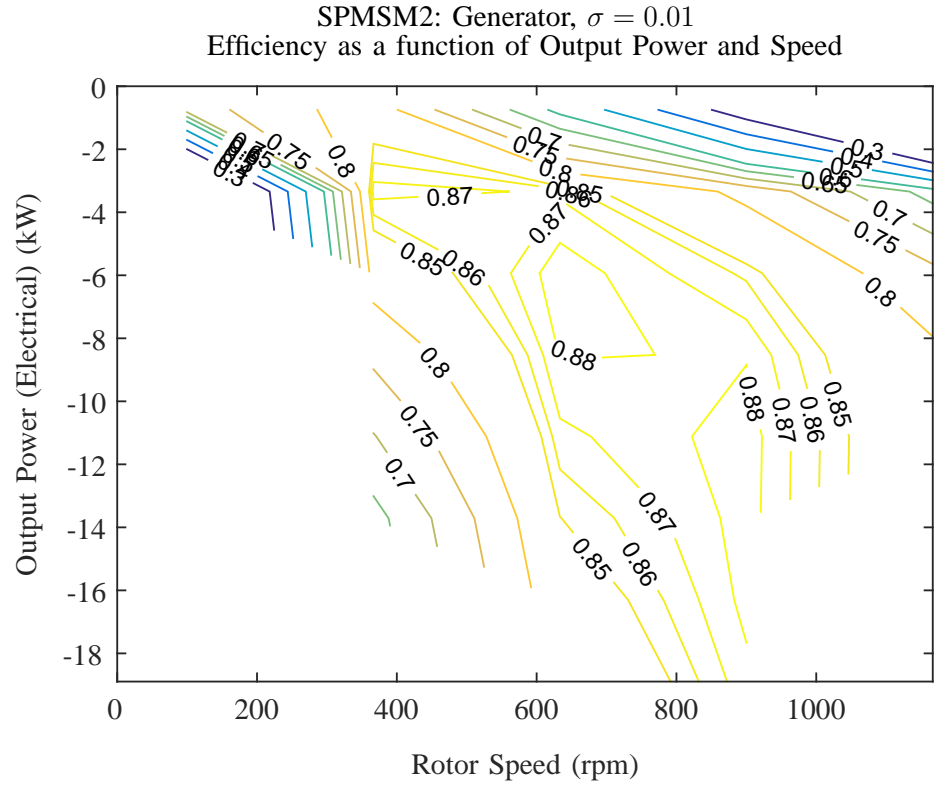


Fig. 24. Efficiency plot for SPMSM2 in generating mode with degree of fault $\sigma = 0.01$ and parameters in Table V.

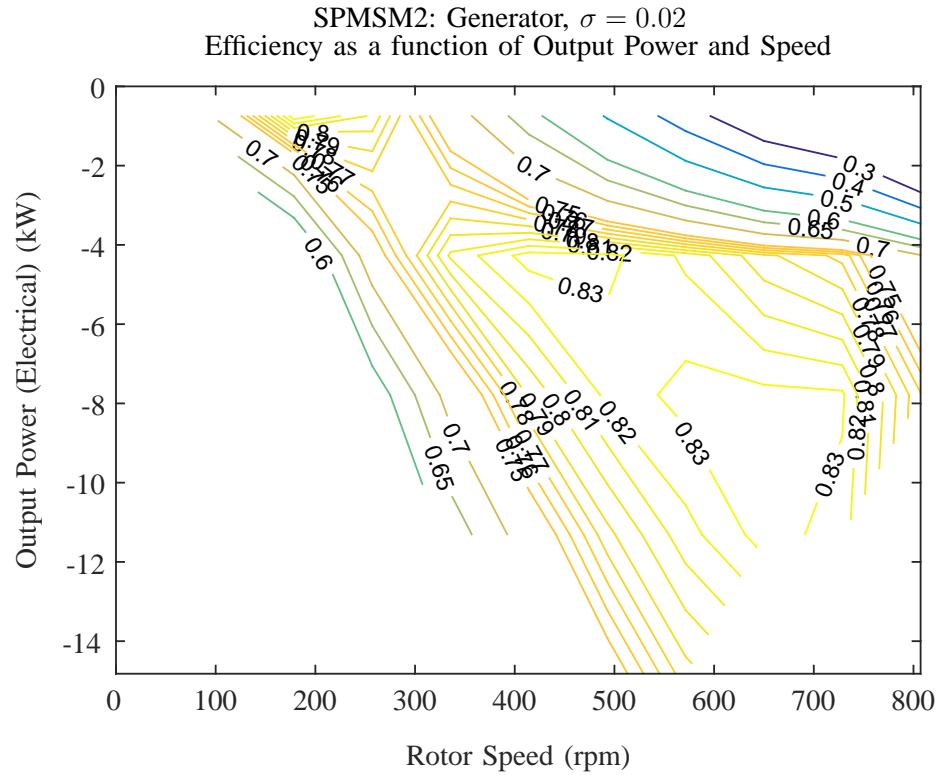


Fig. 25. Efficiency plot for SPMSM2 in generating mode with degree of fault $\sigma = 0.02$ and parameters in Table V.

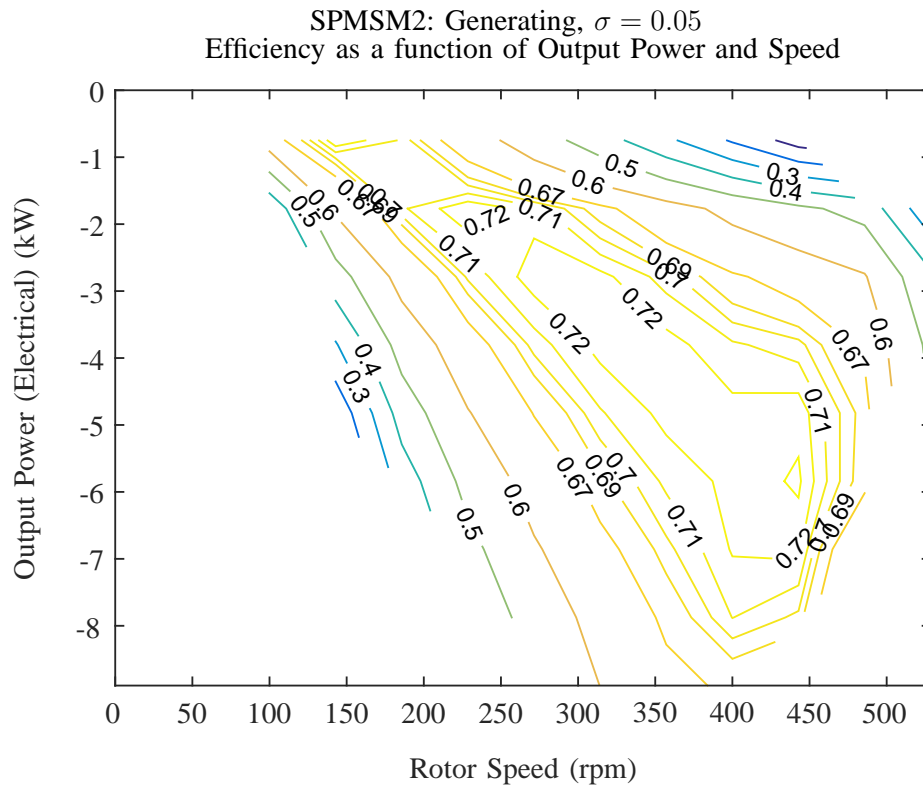


Fig. 26. Efficiency plot for SPMSM2 in propelling mode with degree of fault $\sigma = 0.05$ and parameters in Table V.

discussed in the preceding subsection. The feasible controls (I_d and I_q commands) can be stored in a lookup table for the local SPMSM control. The resulting optimal fit coefficients are included in Table VI.

Another important component to the efficiency curves in Figures 19-26 is the restricted speed range and power range for feasible controls. This restricted range of controls for both propelling and generating is approximated for the supervisory level power flow controller. The restricted power speed range is illustrated in Figures 27 and 28.

D. Supervisory Level Power Flow Optimization Problem

As mentioned previously, the supervisory level controller specifies power flows in and out of the subsystems/components. This is achieved by solving a dynamic hybrid optimization control problem. Specifically, the ingredients of this problem include a performance metric, a switched interconnected system dynamical model, and pertinent constraints. Similar ideas have been previously reported in [6], [8], [22]. Before describing the supervisory level optimization problem, we remind the reader of the modes of operation and set forth an appropriate notation.

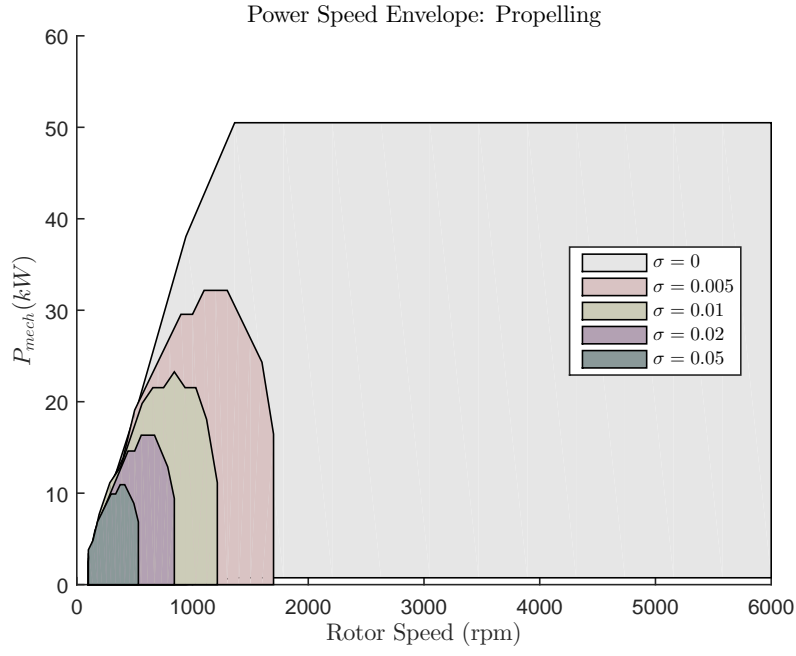


Fig. 27. The power envelope for SPMSM2 in propelling mode with degree of fault $\sigma = 0.005, 0.01, 0.02, 0.05$ and parameters in Table V.

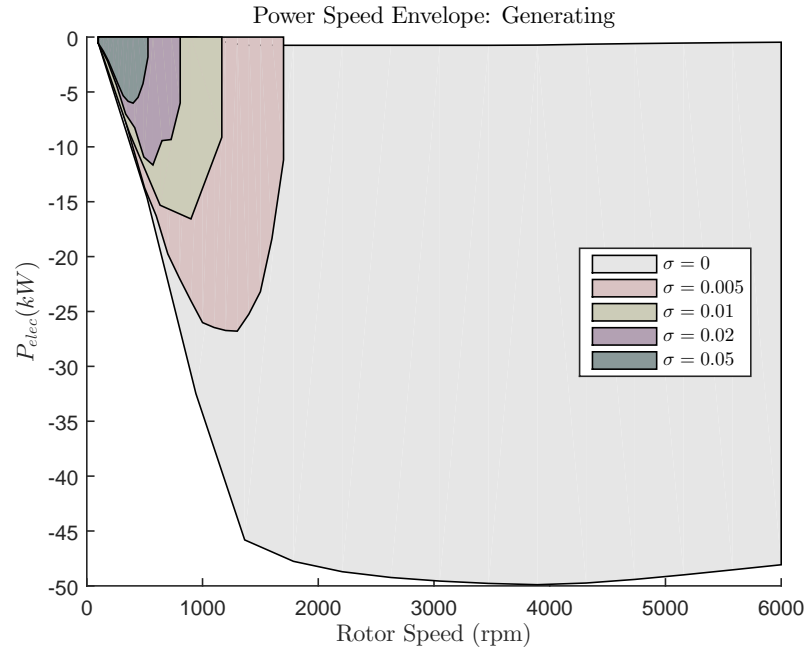


Fig. 28. The power envelope for SPMSM2 in generating mode with degree of fault $\sigma = 0.005, 0.01, 0.02, 0.05$ and parameters in Table V.

Recall the Prius powertrain herein has four modes of operation:

- 1) SPMSM1 propelling (ICE start-up)-SPMSM2 propelling-battery discharging-ICE off;
- 2) SPMSM1 generating-SPMSM2 propelling-battery discharging-ICE on;
- 3) SPMSM1 generating-SPMSM2 propelling-battery charging-ICE on;
- 4) SPMSM1 generating-SPMSM2 generating-battery charging-ICE on or off.

Notationally, let $\alpha_i \in \{0, 1\}$, $i = 1, 2, 3, 4$ denote the active ($\alpha_i = 1$) or non-active ($\alpha_i = 0$) state of each mode. Since only one mode can be physically active at a time, we impose the constraint

$$\alpha_1 + \alpha_2 + \alpha_3 + \alpha_4 = 1 \quad (88)$$

Further, we use $\alpha \in \{1, 2, 3, 4\}$ as a specific mode indicator.

Given the modes of operation defined above, the supervisory level optimization problem has the form

$$\min_{u^\alpha, \alpha} J(x_0, x_{ref}, t_{p,0}, x, u^\alpha, \alpha) \quad (89a)$$

$$\text{subject to } x(t_{p,0}) = x_0, \quad (89b)$$

$$\dot{x} = f_\alpha(t, x, u^\alpha) \quad (89c)$$

$$0 = h_\alpha(t, x, u^\alpha) \quad (89d)$$

$$0 \geq g_\alpha(t, x, u^\alpha) \quad (89e)$$

In the problem statement:

- $J(x_0, x_{ref}, t_{p,0}, t_{p,f}, x, u^\alpha, \alpha)$ is a convex performance index wherein x_0 is the initial state at time $t_{p,0}$, $t_{p,f}$ is the final prediction horizon time, $x(\cdot) \in \mathbb{R}^n$ is the supervisory-level state consisting of all pertinent dynamic subsystem variables, $x_{ref}(t)$ is a reference state trajectory to be tracked over $[t_{p,0}, t_{p,f}]$, $u^\alpha(\cdot) \in \mathbb{R}^m$ is the vector of mode specific continuous control inputs, and $\alpha(\cdot)$ is the modal vector defined above.
- $x = [P_{fuel}, P_{ice}, \Omega_{ice}, \overline{W}_{bat}, \Upsilon_v]^T$ is the state vector where P_{fuel} is the fuel power delivered to the engine, P_{ice} is the ICE output power, Ω_{ice} is the square of the ICE angular speed, \overline{W}_{bat} is the normalized battery state of charge (SOC), and Υ_v is an energy function equal to the square of the vehicle velocity. The speed variables are squared to represent energy, which is ordinarily proportional to the square of speed. Further details can be found in Appendix C.

- $u^\alpha = [u_{fuel}^\alpha, u_1^\alpha, u_2^\alpha, u_{brk}^\alpha]^T$ is the mode dependent continuous control input vector wherein u_{fuel}^α is the commanded normalized fuel in each mode of operation, u_1^α is the commanded fraction of maximum speed-dependent power for SPMSM1 in each mode of operation which is electrical in mode 1 and mechanical in the remaining modes, u_2^α is the commanded fraction of maximum speed-dependent power for SPMSM2 in each mode of operation which is electrical in modes 1, 2, 3 and mechanical in 4, and u_{brk}^α is the commanded fraction of maximum speed-dependent frictional braking power in each mode.
- The performance index (PI), $J(\cdot)$, is one of two expressions depending on whether the engine is on or off (note that the engine on or engine off is a fuel dependent control action and does not represent two distinct modes of operation):

$$J_{ice,off}(\cdot) = \int_{t_{p,0}}^{t_{p,f}} C_v (\Upsilon_v - \Upsilon_{v,ref})^2 + \sum_{i=1}^4 C_{brk}^i \alpha_i (P_{brk}^i)^2 + C_{u1} \sum_{i=1}^4 \alpha_i (u_1^i)^2 + C_{u2} \sum_{i=1}^4 \alpha_i (u_2^i)^2 dt \quad (90a)$$

and

$$J_{ice,on}(\cdot) = J_{ice,off}(\cdot) + \int_{t_{p,0}}^{t_{p,f}} C_{SOC} (\overline{W}_{bat} - \overline{W}_{bat,ref})^2 + C_{fuel} (P_{fuel})^2 dt \quad (90b)$$

where $\Upsilon_{v,ref}$ is the squared reference velocity or energy to track, $\overline{W}_{bat,ref}$ is the desired battery state of charge, C_v is the penalty weight on the vehicle energy error (and implicitly vehicle tracking error), C_{brk} is the penalty weight on frictional braking use to promote battery regenerative braking, C_{u1} and C_{u2} are the penalty weights on SPMSM1 and SPMSM2 usage to encourage bang-bang solutions in the numerical optimization described shortly⁶, C_{SOC} is the penalty weight on deviation of the battery state of charge from a desired value, and C_{fuel} is the penalty weight on ICE engine fuel consumption.

- $\dot{x} = f_\alpha(t, x, u^\alpha)$ represents a composite of the mode specific subsystem dynamics without intercon-

⁶This is similar to the penalty weight on electric drive system use to promote bang-bang solutions in [23].

nections. Specifically,

$$\begin{bmatrix} \dot{P}_{fuel} \\ \dot{P}_{ice} \\ \dot{\Omega}_{ice} \\ \dot{\bar{W}}_{bat} \\ \dot{\Upsilon}_v \end{bmatrix} = \sum_{i=1}^4 \alpha_i \begin{bmatrix} f_{fuel}^i(P_{fuel}, \Omega_{ice}, u_{fuel}^i) \\ f_{ice}^i(P_{fuel}, P_{ice}, \Omega_{ice}) \\ f_{\Omega_{ice}}^i(P_{ice}, P_{ice,psd}^i) \\ f_{bat}^i(\bar{W}_{bat}, P_{bat}^i) \\ f_v^i(P_{brk}^i, P_{whl,psd}^i, P_{2,L}^i, \Upsilon_v) \end{bmatrix} \quad (91)$$

wherein $P_{ice,psd}^i$ is the ICE power routed into the power split device in the i -th mode, P_{bat}^i is the i -th mode battery discharge or charge power, P_{brk}^i is the i -th mode frictional braking power, $P_{whl,psd}^i$ is the i -th mode power delivered to the drive wheels from the power split split device, and $P_{2,L}^i$ is the i -th mode SPMSM2 power to the drive wheels. Recall the sum of α_i 's is one and thus only one mode is operative at a time. The expanded dynamical expressions are developed in Appendix C and are summarized here:

– The engine dynamics are

$$\dot{P}_{fuel} = \sum_{i=1}^4 \alpha_i \left(\frac{-1}{\tau_{fuel}} P_{fuel} + \frac{1}{\tau_{fuel}} P_{fuel}^{max}(\omega_{ice}) u_{fuel}^i \right) \quad (92)$$

$$\dot{P}_{ice} = \frac{-1}{\tau_{ice}} P_{ice} + \frac{1}{\tau_{ice}} \eta_{ice}(P_{ice}, \omega_{ice}) P_{fuel} \quad (93)$$

$$\dot{\Omega}_{ice} = \frac{2}{J_{ice}} (P_{ice,psd} + P_{ice}) \quad (94)$$

– The battery dynamics are

$$\dot{\bar{W}}_{bat} = \sum_{i=1}^4 \alpha_i \left\{ - \left[-\ln(\bar{W}_{bat} + c_{b,1}^i) + c_{b,2}^i \frac{P_{bat}^i}{n_b} + c_{b,3}^i + c_{b,4}^i \left(\frac{P_{bat}^i}{n_b} \right)^2 \right] \frac{P_{bat}^i}{n_b W_{bat}^{max}} \right\} \quad (95)$$

– The vehicle dynamics are

$$\dot{\Upsilon}_v = \sum_{i=1}^4 \alpha_i \left[\frac{2}{m_v} (P_d(v) + P_{rr}(v, \theta_r) + P_b(\theta_r) + P_{whl,psd}^i + P_{2,L}^i - P_{brk}^i) \right] \quad (96)$$

- $0 = h_\alpha(t, x, u^\alpha)$ describes the interconnections of the subsystem models and any other equality constraints pertinent to the optimization problem. Specifically,

$$0 = \begin{bmatrix} h_{P_{1,e}}^\alpha(P_{1,e}^\alpha, P_{1,L}^\alpha, \omega_{1,m}, u_1^\alpha) \\ h_{P_{1,L}}^\alpha(P_{1,e}^\alpha, P_{1,L}^\alpha, \omega_{1,m}, u_1^\alpha) \\ h_{P_{2,e}}^\alpha(P_{2,e}^\alpha, P_{2,L}^\alpha, \omega_{2,m}, u_2^\alpha) \\ h_{P_{2,L}}^\alpha(P_{2,e}^\alpha, P_{2,L}^\alpha, \omega_{2,m}, u_2^\alpha) \\ h_{P_{ice,psd}}^\alpha(P_{1,L}^\alpha, \omega_{1,m}, \omega_{ice}) \\ h_{P_{whl,psd}}^\alpha(P_{1,L}^\alpha, v, \omega_{1,m}) \\ h_{P_{brk}}^\alpha(\Upsilon_v, u_{brk}^\alpha) \\ P_{bat}^\alpha - P_{1,e}^\alpha - P_{2,e}^\alpha \end{bmatrix} \quad (97)$$

In the above, $P_{1,e}^i$ is the i -th mode SPMSM1 electrical power, $P_{1,L}^i$ is the i -th mode SPMSM1 mechanical power, $\omega_{1,m}$ is the SPMSM1 rotor angular speed, $P_{2,e}^i$ is the i -th mode SPMSM2 electrical power, $P_{2,L}^i$ is the i -th mode SPMSM2 mechanical power, and $\omega_{2,m}$ is the SPMSM2 rotor angular speed. The above constraints are developed in Appendix C with the main results given below:

- The SPMSM1 electrical and mechanical constraints are

$$0 = P_{1,e}^\alpha - \begin{cases} P_{1,e}^{max}(\omega_{1,m})u_1^\alpha, & \alpha = 1 \\ \eta_{1,inv}\eta_{SPMSM1,gen}(P_{1,L}^\alpha, \omega_{1,m})P_{1,L}^\alpha, & \alpha = 2, 3, 4 \end{cases} \quad (98)$$

$$0 = P_{1,L}^\alpha - \begin{cases} \eta_{1,inv}\eta_{SPMSM1,prop}(P_{1,e}^\alpha, \omega_{1,m})P_{1,e}^\alpha, & \alpha = 1 \\ P_{1,L}^{max}(\omega_{1,m})u_1^\alpha, & \alpha = 2, 3, 4 \end{cases} \quad (99)$$

- The SPMSM2 electrical and mechanical constraints are

$$0 = P_{2,e}^\alpha - \begin{cases} P_{2,e}^{max}(\omega_{2,m})u_2^\alpha, & \alpha = 1, 2, 3 \\ \eta_{2,inv}\eta_{SPMSM2,gen}(P_{2,L}^\alpha, \omega_{2,m})P_{2,L}^\alpha, & \alpha = 4 \end{cases} \quad (100)$$

$$0 = P_{2,L}^\alpha - \begin{cases} \eta_{2,inv}\eta_{SPMSM2,prop}(P_{2,e}^\alpha, \omega_{2,m})P_{2,e}^\alpha, & \alpha = 1, 2, 3 \\ P_{2,L}^{max}(\omega_{2,m})u_2^\alpha, & \alpha = 4 \end{cases} \quad (101)$$

– The power split device mechanical power connections are

$$0 = P_{ice,psd}^\alpha - \frac{(r_s + r_r)}{r_s} \left(\frac{P_{1,L}^\alpha}{|\omega_{1,m}| + \epsilon_s} \right) \omega_{ice}, \quad \alpha = 1, 2, 3, 4 \quad (102)$$

$$0 = P_{whl,psd}^\alpha - \left(-\frac{r_r \gamma}{r_s} \left(\frac{P_{1,L}^\alpha}{|\omega_{1,m}| + \epsilon_s} \right) v \right), \quad \alpha = 1, 2, 3, 4 \quad (103)$$

– The frictional braking power interconnection equations are

$$0 = P_{brk}^\alpha - P_{brk}^{max}(\Upsilon_v) u_{brk}^\alpha, \quad \alpha = 1, 2, 3, 4 \quad (104)$$

The various efficiencies, designated by η 's, and other constants are set forth in Appendix C.

- $0 \geq g_\alpha(t, x, u^\alpha)$ represents inequality constraints pertinent to the optimization problem, for example, bounds on states, inputs, etc. Specifically,

$$0 \geq \begin{bmatrix} x_l - x \\ x - x_u \\ y_l - y^\alpha \\ y^\alpha - y_u \\ 0 - u^\alpha \\ u^\alpha - 1 \end{bmatrix} \quad (105)$$

where x_l is the vector of lower bounds on the states, x_u is the vector of upper bounds on the states, $y^\alpha = [P_{bat}^\alpha, P_{1,e}^\alpha, P_{1,L}^\alpha, P_{2,e}^\alpha, P_{2,L}^\alpha, P_{ice,psd}^\alpha, P_{whl,psd}^\alpha]^T$ is the vector of algebraic variables that depend upon states and continuous control inputs, y_l is the vector of lower bounds on the algebraic variables, y_u is the vector of upper bounds on the algebraic variables.

E. Comments on the Numerical Solution of the Optimization Problem

The minimization problem in (89) is numerically ill-conditioned since the optimization requires searching over all combinations of switching sequences. As discussed in [22], this is an NP-hard problem which exponentially increases with the number of modes. To avoid this complexity, the switched optimal control problem in (89) is replaced with the embedded optimal control problem (a partial relaxation of only the modes of operation) which has the form [19], [22]

$$\min_{\substack{u^i, \alpha_i \in [0,1] \\ i=1,\dots,r}} \sum_{i=1}^r \alpha_i J_\alpha(x_0, x_{ref}, t_{p,0}, t_{p,f}, x_e, u^i) \quad (106a)$$

$$\text{subject to } x(t_0) = x_0, \quad (106b)$$

$$\dot{x}_e = \sum_{i=1}^r \alpha_i f_i(t, x_e, u^i), \quad (106c)$$

$$0 = \sum_{i=1}^r \alpha_i, \quad \alpha_i \in [0, 1] \quad (106d)$$

$$0 = h_i(t, x_e, u^i), \quad i = 1, 2, 3, 4 \quad (106e)$$

$$0 \geq g_i(t, x_e, u^i) \quad i = 1, 2, 3, 4 \quad (106f)$$

Observe the embedded problem state is denoted as x_e to distinguish it from the original problem state. The distinguishing of the embedded optimization problem relative to the original optimization problem is (106d) where the requirement $\alpha_i \in \{0, 1\}$ is relaxed to $\alpha_i \in [0, 1]$. This relaxation transforms the original problem with combinatorial complexity into a traditional nonlinear optimization. When $\alpha_i = 1$, then the embedded problem solution in (106) reduces to the switched problem solution in (89). When $\alpha_i \in (0, 1)$ one must project the modal solution onto the nearest physically realizable mode of operation using techniques described in [19], [22], [23]. However, the basic idea is to project the embedded fractional value of α_i onto the nearest integer value, while maintaining the constraint (106d).

It was proven in [19] that the switched state trajectories of x of (89) are dense in the set of embedded system trajectories x_e in (106), so a given embedded trajectory can be approximated by a switched system trajectory. So solving (106) provides a numerically viable nonlinear optimization problem which can be used to generate approximate solutions to (89). For additional details concerning the embedded optimal control problem, we refer the reader to [19].

The specific numerical solution uses MATLAB's *fmincon*, which requires the optimization problem to be discretized. Briefly, the performance metric is discretized using trapezoidal numerical integration and the dynamics are discretized using collocation. The reader is referred to earlier works for details [23].

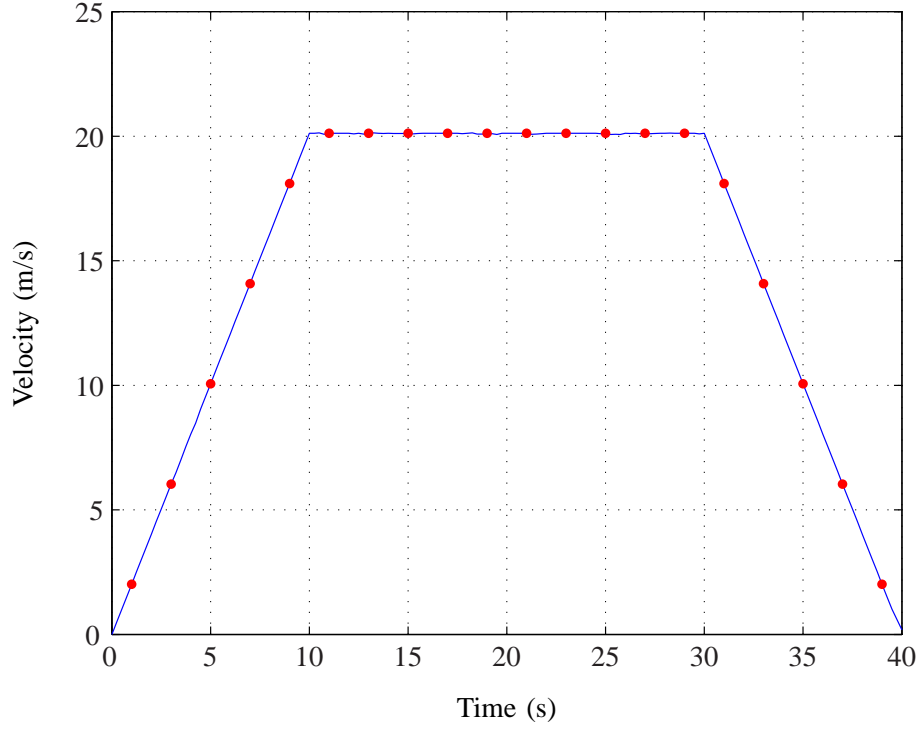


Fig. 29. Simulated Prius velocity tracking without fault: (—) simulated velocity, (•) commanded velocity.

F. Control and ITSC Fault Simulation Results

This section reviews the performance of the Prius with a 40 s trapezoidal drive profile subject to an ITSC fault at 20 s. The trapezoidal profile consists of (i) a constant acceleration increase in velocity from rest to 20.12 m/s (45 mph) over [0,10]s, (ii) constant velocity over [10,30]s, and (iii) constant deceleration to rest over [30,40]s. Figure 29 shows the commanded trapezoidal and the simulated unfaulted vehicle response with $\theta_v = 0$ (the road angle).

Drive profile control simulations are performed using techniques set forth in [23]. The optimization problem is discretized with a $T_c = 0.25$ s interval time partition according to the methods in [23]. In the PI, (90), the prediction horizon is 0.5 s (2 partitions) and the penalty weights are $C_v = 100$, $C_{brk}^i = 1000/(50)^2$ for $i = 1, 2, 3$, $C_{brk}^4 = 100/(50)^2$, $C_{u1} = 2$, $C_{u2} = 2$, $C_{fuel} = 10/(383.5)^2$, and $C_{SOC} = 1000$ when $\overline{W}_{bat} < \overline{W}_{bat,ref} = 0.58$ and zero otherwise.

We note that the vehicle cannot change velocity instantaneously, thus a velocity reference obtained from the operator at kT_c becomes the commanded velocity to achieve at $(k+1)T_c$, i.e., $v_{ref}((k+1)T_c)$. In the optimization, at time kT_c , the present, the desired velocity at $(k+1)T_c$ is known. The value at $(k+2)T_c$

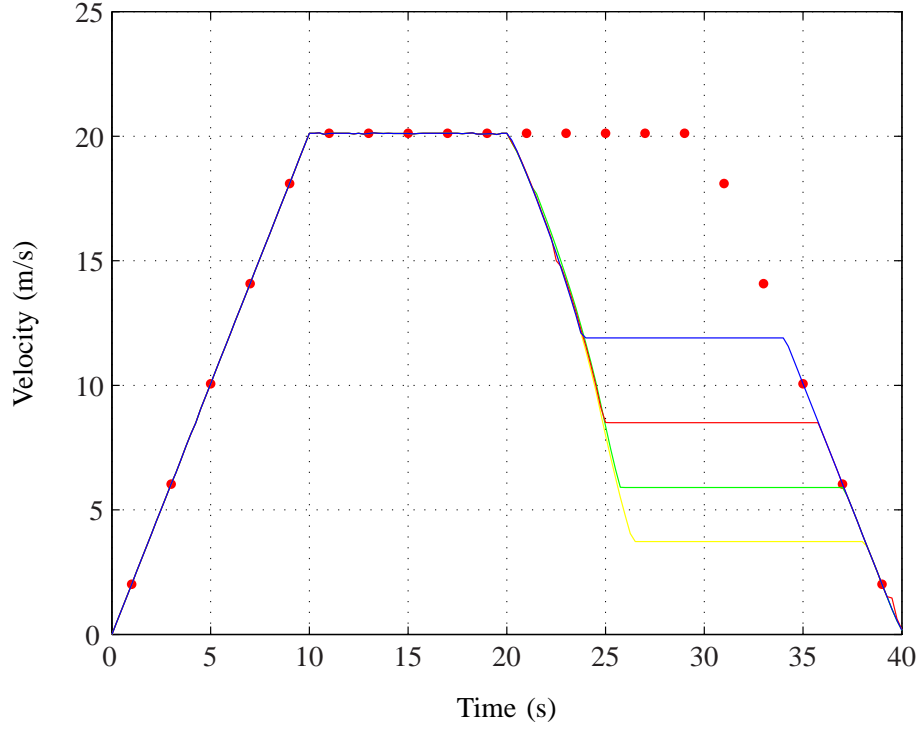


Fig. 30. Simulated Prius velocity tracking with ITSC faults of 0.5%, 1%, 2%, and 5%: (—) 0.5% fault, (—) 1% fault, (—) 2% fault, (—) 5% fault, (•) commanded velocity.

is unknown and is estimated linearly as

$$v_{ref,est}((k+2)T_c) = v_{ref}((k+1)T_c) + T_c \left[\frac{v_{ref}((k+1)T_c) - v_{ref}(kT_c)}{T_c} \right] \quad (107)$$

Thus,

$$\Upsilon_{v,ref}(kT_c) = [v_{ref}(kT_c)]^2 \quad (108)$$

$$\Upsilon_{v,ref}((k+1)T_c) = [v_{ref}((k+1)T_c)]^2 \quad (109)$$

$$\Upsilon_{v,ref,est}((k+2)T_c) = [v_{ref,est}((k+2)T_c)]^2 \quad (110)$$

The reference velocity is extrapolated from known current and past values which leads to the extrapolated reference, $\Upsilon_{v,ref,est}$, as in (110). We use extrapolated values because we do not assume that future values of the drive profile are known. This linear extrapolation assumption is meant to approximate a driver but does add a small error to the tracking of reference signals that are non-piecewise linear or have “corners”.

The Prius model is simulated again over the trapezoidal drive profile now with ITSC faults of 0.5%, 1%, 2%, and 5% occurring at 20 s. Figure 30 shows the vehicle velocity tracking achieved for each fault level. Every fault is considered to have been detected by the observer of Section V at $t = 20$ s. At 20 s, $\Upsilon_{v,ref}$

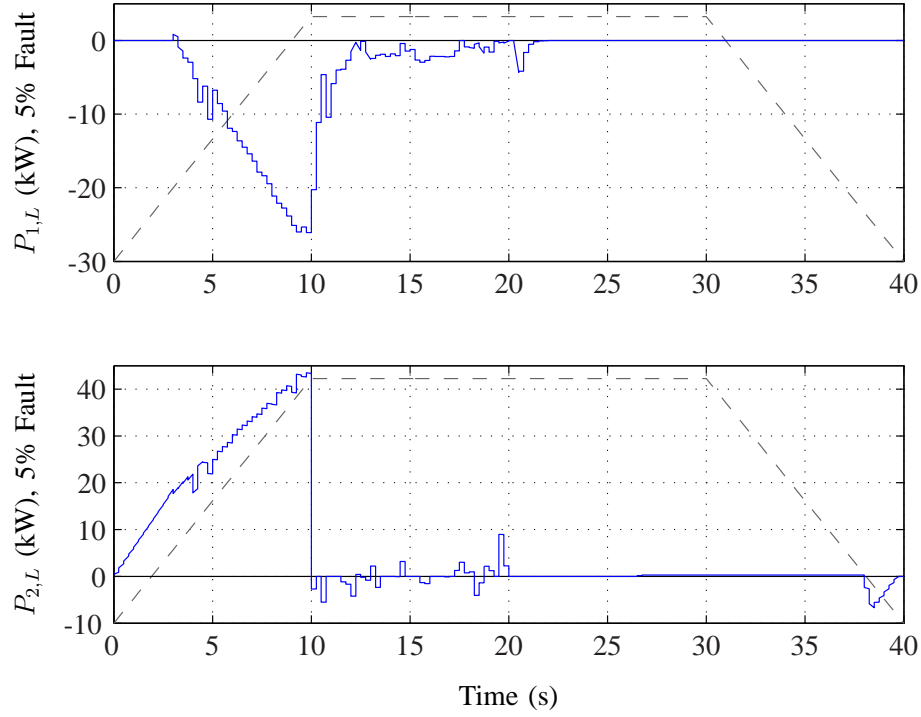


Fig. 31. Simulated Prius SPMSM1 (generator) and SPMSM2 (traction) mechanical powers with a 5% ITSC fault: (—) power, (---) superimposed commanded velocity.

is chosen to decelerate the vehicle at -2 m/s^2 until $\Upsilon_{v,ITSC,max}$ (the square of 95% of the maximum fault operation velocity) is reached. Then the reference is the minimum of $\Upsilon_{v,ref}$ and $\Upsilon_{v,ITSC,max}$ until the fault is removed. During the deceleration phase, SPMSM2 is unpowered to avoid exacerbating thermal runaway and hence unsafe operating conditions. This velocity modification behavior during faults is exhibited in Figure 30 for all of the fault cases.

Figure 31 shows the mechanical power (positive if propelling and negative if generating) of SPMSM1 and SPMSM2 over the drive profile with the 5% ITSC fault. Similar SPMSM1 and SPMSM2 responses are displayed with the other fault levels. SPMSM1 is off until it is used to start the engine from 3 to 3.5 s. Thereafter SPMSM1 is driven by the ICE and sends power to the electrical bus to drive SPMSM2 and recharge the battery. After the fault occurs, SPMSM1 is on for the next 2 s while the vehicle speed decreases and then remains off for the remainder of the drive profile. We note from 20.25 s onward that the ICE is off as well. SPMSM1 is still able to provide battery charge power from 20.25 to 22 s, during which the ICE is off, by consuming the ICE inertia energy. SPMSM2 propels the vehicle during the initial commanded acceleration from 0 to 10 s and both propels and recharges the battery from 10 to 20 s during

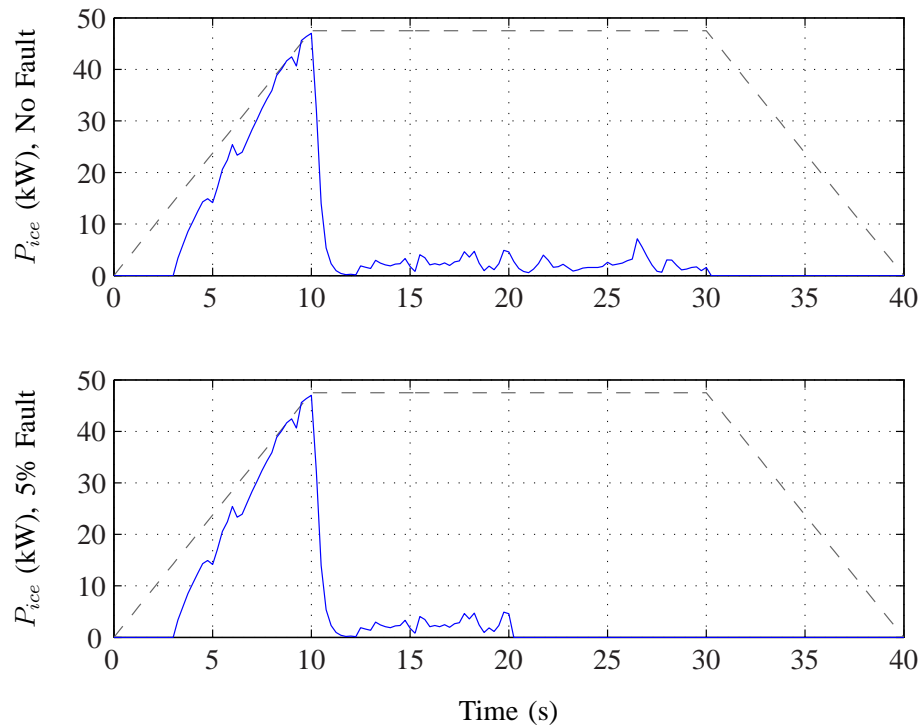


Fig. 32. Simulated Prius engine power for no fault and 5% fault level: (—) superimposed drive profile.

the commanded constant velocity. Upon the detection of the fault, SPMSM2 is off while the vehicle speed is decreased to the maximum safe fault operation velocity. Next, the drive is used to propel the vehicle at constant velocity from 26.5 s until the commanded deceleration to rest is encountered at 38 s, then the drive provides battery regenerative braking to 39.75 s.

For reference, the ICE output power for the unfaulted and 5% fault level cases are provided in Figure 32. In addition, the projected mode selections are given in Figure 33.

VIII. APPLICATION: HEAVY HYBRID VEHICLES

According to Harrington and Krupnick at Resources for the Future, the National Highway Traffic Safety Administration mandated the first-ever federal requirements for improving fuel economy in heavy-duty commercial vehicles in 2011 [24]. The focus on reducing fuel consumption in heavy vehicles on the highway has also had an impact in the off-road heavy vehicle industry. Leading companies of off-road vehicles, such as Caterpillar and John Deere, have released hybrid versions of off-road construction and forestry equipment. Although fuel prices have dropped in the past few years, the environmental, economic,

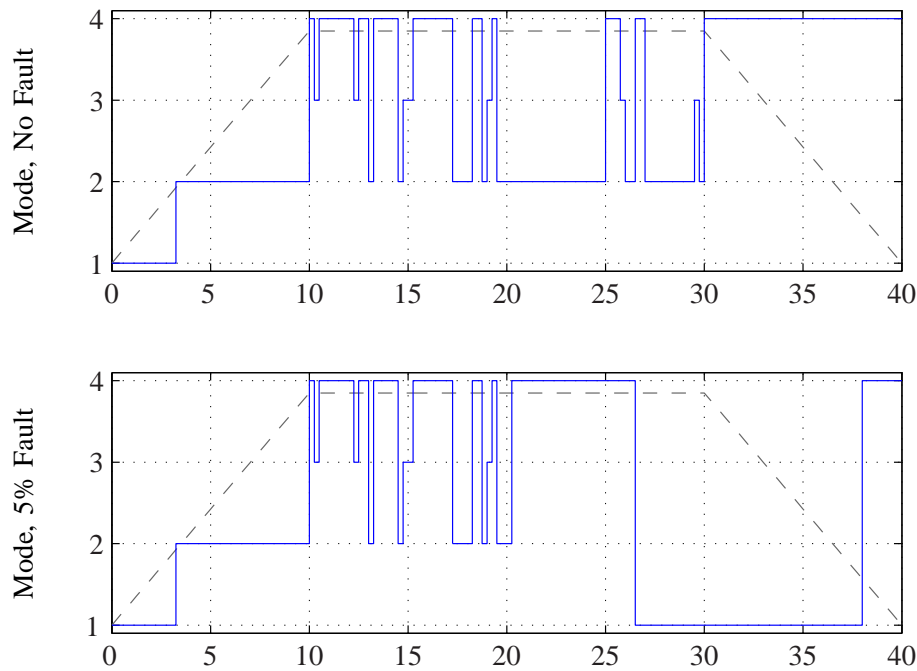


Fig. 33. Projected modes for the Prius simulation: (—) superimposed commanded velocity.

and regulatory influences on heavy vehicle design promise continued growth in the area of heavy hybrid technology.

Electric machines are a common component in heavy hybrid vehicles, such as the Caterpillar D7E Dozer [25] and the John Deere 644k Hybrid Wheel Loader [26]. The Deere 644k Hybrid Wheel Loader uses two permanent-magnet synchronous machines (PMSM), one primarily as a generator and the other as a transmission drive. Due to the tough working conditions of these vehicles, the areas of safety, robust performance, and reduced repair costs are key marketable features. In the event of a fault within the electric machine, fault detection, and fault-tolerant control in the heavy hybrid vehicles can improve each of these marketable features. The detection of an inter-turn short circuit (ITSC) fault in the stator windings of the PMSM is critical to maintaining the safe operation of these vehicles. In this section we outline the impact of this work on ITSC fault detection in PMSM to the industry of heavy hybrid vehicles.

A. Increased Scale

The simulation in Section VI demonstrates the effective use of the ITSC fault detection scheme using an embedded moving horizon observer (EMHO). The surface PMSM (SPMSM) explored in Section VI has a maximum power of about 30kW. Heavy hybrid drivetrains require motors on the scale of hundreds

of kilowatts. Fortunately, the size of the motors does not effect the structure of the mathematical model for SPMSM or the structure of the EMHO used to detect ITSC faults. As such, the same techniques developed for ITSC fault detection for SPMSM can be applied directly to SPMSM in heavy hybrid vehicles.

B. Interior PMSM

Many heavy hybrid vehicle manufacturers prefer interior PMSM (IPMSM) over the surface mounted counterparts. Although the control of SPMSM is simpler, the IPMSM has manufacturing advantages as well as some additional control techniques. The magnets in the IPMSM are embedded in the rotor laminations. This allows for permanent magnets which are rectangular and easier to produce in addition to avoiding the problem of attaching magnets to the surface of the rotor. Another key advantage to the IPMSM, is that the iron in the rotor can be magnetized between the magnetic poles and provide the so-called reluctance torque. The reluctance torque is especially useful at producing power at high speeds when the bus voltage limits the output power. Despite the advantages of the IPMSM, stators in IPMSM and SPMSM are similar and can suffer from the same ITSC winding faults. In this subsection, we will introduce a stator voltage model from the IPMSM and discuss the applications of the SPMSM fault detection work.

The unfaulted interior PMSM (neglecting leakage inductance for simplicity) can be modeled by [1]

$$v_{abc} = R_s i_{abc} + \frac{d}{dt} [L_{AB}(\theta_r) i_{abc}] + e_{abc} \quad (111)$$

where $v_{abc} = [v_{as}, v_{bs}, v_{cs}]^\top$, $i_{abc} = [i_{as}, i_{bs}, i_{cs}]^\top$, R_s denotes the stator resistance in each coil, θ_r and ω_r are the electrical position and speed of the rotor, the back emf e_{abc} satisfies

$$e_{abc} = \begin{bmatrix} e_a \\ e_b \\ e_c \end{bmatrix} = \lambda_m \omega_r \begin{bmatrix} \cos(\theta_r) \\ \cos(\theta_r - 2\pi/3) \\ \cos(\theta_r + 2\pi/3) \end{bmatrix}, \quad (112)$$

and the inductance matrix $L_{AB}(\theta_r)$ has the form

$$L_{AB} = \begin{bmatrix} L_A + L_B \cos 2\theta_r & -\frac{1}{2}L_A + L_B \cos 2(\theta_r - \frac{\pi}{3}) & -\frac{1}{2}L_A + L_B \cos 2(\theta_r + \frac{\pi}{3}) \\ -\frac{1}{2}L_A + L_B \cos 2(\theta_r - \frac{\pi}{3}) & L_A + L_B \cos 2(\theta_r - \frac{2\pi}{3}) & -\frac{1}{2}L_A + L_B \cos 2(\theta_r + \pi) \\ -\frac{1}{2}L_A + L_B \cos 2(\theta_r + \frac{\pi}{3}) & -\frac{1}{2}L_A + L_B \cos 2(\theta_r + \pi) & L_A + L_B \cos 2(\theta_r + \frac{2\pi}{3}) \end{bmatrix}. \quad (113)$$

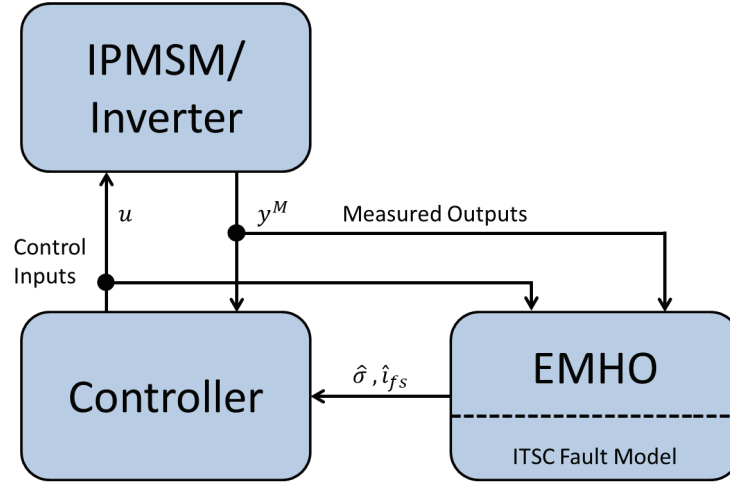


Fig. 34. Fault detection scheme for IPMSM with estimated degree of fault $\hat{\sigma}$ and estimated fault current \hat{i}_{fs} .

In the case of the SPMSM, the sinusoidal inductance terms $L_B \cos(\cdot)$ is zero.

Modeling an IPMSM with ITSC faults is an area of future research. From the developments in Section III, we expect that the back emf e_{abc} and the inductance matrix $L_{AB}(\theta_r)$ will become functions of the degree of fault $\sigma \in [0, 1]$. The key difference is modeling how L_A and L_B change after a fault has occurred. Despite the current lack of an ITSC fault model for the IPMSM, the fault detection framework and observer structure can be extended to the IPMSM pending the model for the ITSC faults. The structure for the IPMSM ITSC fault detection problem is shown in Figure 34.

C. Fault-Tolerant Control

After an ITSC fault has occurred, the eddy loop acts as an induction heater within the stator windings. For heavy vehicles, oil-cooled stator windings improve the ability to cool the stator windings after an ITSC fault and may allow for a reduced operating condition for short periods of time. This reduced operating condition, or “limp-home” mode, can allow vehicles in remote work sites to reach a safe location for repairs. Since off-road heavy vehicles can spend considerable time in remote locales, the ability to “limp home” provides a significant advantage.

Similar to the fault-tolerant scheme for the Prius, we propose using the ITSC fault model of the PMSM (whether surface or interior magnets) to generate fault-tolerant controls, operating limits, and efficiency curves at various degrees of fault σ . The method for constructing these efficiency curves and fault-tolerant

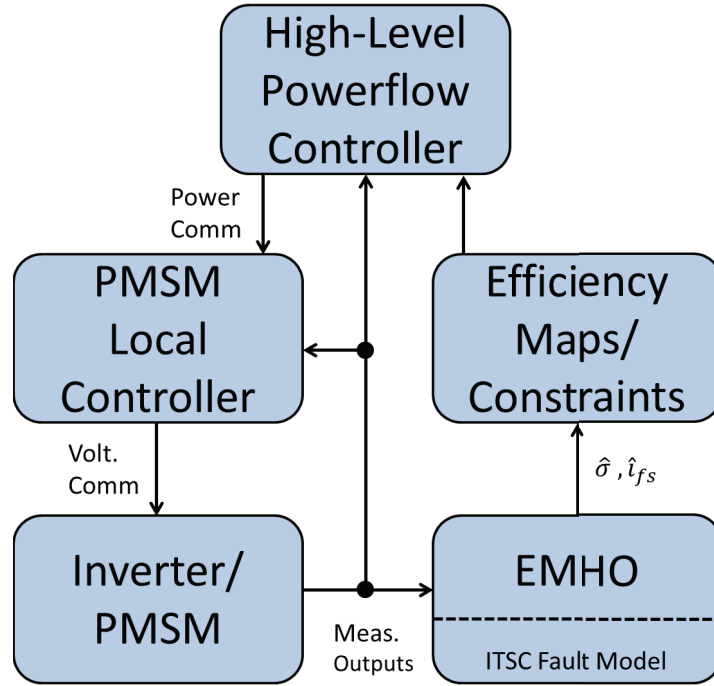


Fig. 35. Fault-tolerant control scheme with estimated degree of fault $\hat{\sigma}$ and estimated fault current \hat{i}_{fs} .

controls are discussed in Section III, Section VII, and [27]. The basic structure for the fault tolerant control with a high-level power flow controller is shown in Figure 35.

IX. CONCLUDING REMARKS AND FUTURE WORK

In this work, we have developed a moving horizon observer to detect ITSC faults in surface permanent magnet synchronous machines. A simplified version of the observer is validated through simulation. Applications to supervisory control and heavy hybrid vehicles are also developed.

The development of an ITSC fault model for interior permanent magnet synchronous machines is an area of future research. With this model, a moving horizon observer can be developed to detect ITSC faults in much the same manner as presented in this paper. Another area of future research is validating the fault models and fault detection scheme in physical devices. The model validation of the fault model for surface permanent magnet machines was started in [13], but verification of the interior permanent magnet machine fault model is still incomplete.

Optimizing the computational time for the moving horizon observer is also an area of future work. In part, this requires optimizing the number of horizons, horizon width, and the search algorithm. This is a

dual formulation to the problem in model predictive control of determining optimal horizon parameters. As computational power in vehicles continues to increase and processor prices decrease, we expect that using moving horizon observers for fault detection will become an increasingly attractive solution to improving electric machine safety, reliability, and repair costs.

ACKNOWLEDGMENTS

This work was partially supported by the Department of Energy, Award No. DE-EE0005568. The authors would also like to acknowledge the support of Greg Shaver and the Hoosier Heavy Hybrid Center of Excellence.

APPENDIX A

When an ITSC fault occurs in two phases simultaneously, say phase-a and phase-b, there exists fault currents i_{fs}^a and i_{fs}^b within each of the two fault loops. The degree of fault in each phase is denoted σ_a and σ_b . For ease of notation we define $\tau_a = 1 - \sigma_a$ and $\tau_b = 1 - \sigma_b$. The stator voltage model is given by

$$v_{abcf} = R_f(\sigma_a, \sigma_b)i_{abcf} + L_f(\sigma_a, \sigma_b)\frac{d}{dt}i_{abcf} + e_{abcf}(\sigma_a, \sigma_b),$$

where

$$v_{abcf} = \begin{bmatrix} v_{as} & v_{bs} & v_{cs} & 0 & 0 \end{bmatrix}^\top, \quad i_{abcf} = \begin{bmatrix} i_{as} & i_{bs} & i_{cs} & i_{fs}^a & i_{fs}^b \end{bmatrix}^\top,$$

$$R_f(\sigma_a, \sigma_b) = \begin{bmatrix} \tau_a R_s & 0 & 0 & 0 & 0 \\ 0 & \tau_b R_s & 0 & 0 & 0 \\ 0 & 0 & R_s & 0 & 0 \\ 0 & 0 & 0 & \sigma_a R_s & 0 \\ 0 & 0 & 0 & 0 & \sigma_b R_s \end{bmatrix},$$

$$L_f(\sigma_a, \sigma_b) = \begin{bmatrix} \tau_a^2 L & \tau_a \tau_b M & \tau_a M & \tau_a \sigma_a L & \tau_a \sigma_b M \\ \tau_a \tau_b M & \tau_b^2 L & \tau_b M & \tau_b \sigma_a M & \tau_b \sigma_b L \\ \tau_a M & \tau_b M & L & \sigma_a M & \sigma_b M \\ \tau_a \sigma_a L & \tau_b \sigma_a M & \sigma_a M & \sigma_a^2 L & \sigma_a \sigma_b M \\ \tau_a \sigma_b M & \tau_b \sigma_b L & \sigma_b M & \sigma_a \sigma_b M & \sigma_b^2 L \end{bmatrix},$$

and

$$e_{abcf}(\sigma_a, \sigma_b) = \lambda_m \omega_r \begin{bmatrix} \tau_a \cos(\theta_r) \\ \tau_b \cos(\theta_r - 2\pi/3) \\ \cos(\theta_r + 2\pi/3) \\ \sigma_a \cos(\theta_r) \\ \sigma_b \cos(\theta_r - 2\pi/3) \end{bmatrix}$$

An ITSC fault occurs in all three phases, there is an additional fault current i_{fs}^c and degree of fault σ_c . The stator voltage model extends is an extension of the two-phase stator voltage model. The electromechanical power couples the electrical and mechanical components of the SPMSM as per the following equation

$$T_e \omega_{rm} = P_a + P_b + P_c + P_f^a + P_f^b = J \omega_{rm} \dot{\omega}_{rm} + B \omega_{rm}^2 + T_L \omega_{rm},$$

where $P_f^a = \sigma_a \lambda_m \omega_r i_{fs}^a \cos(\theta_r)$, $P_f^b = \sigma_b \lambda_m \omega_r i_{fs}^b \cos(\theta_r - 2\pi/3)$, and $P_\zeta = e_\zeta i_{\zeta s}$ for $\zeta = a, b, c$. The total inverter power, $P_{inv} = P_{inv,a} + P_{inv,b} + P_{inv,c}$, is given by

$$P_{inv} = \tau_a R_s i_{as}^2 + \tau_b R_s i_{bs}^2 + R_s i_{cs}^2 + \sigma_a R_s (i_{fs}^a)^2 + \sigma_b R_s (i_{fs}^b)^2 \\ + \frac{d}{dt} \Upsilon_f(\sigma_a, \sigma_b) + P_a + P_b + P_c + P_f^a + P_f^b,$$

where $\Upsilon_f(\sigma_a, \sigma_b) = i_{abcf}^\top L_f(\sigma_a, \sigma_b) i_{abcf}$.

APPENDIX B

For the LTV system

$$\dot{x}(t) = A(t)x(t) + B(t)u(t) \quad (114)$$

$$y(t) = C(t)x(t) + D(t)u(t), \quad (115)$$

the output $y(t)$ can be expressed as a function of the initial state x_0 and input $u(t)$ as per

$$y(t) = C(t)\Phi(t, t_0)x_0 + C(t) \int_{t_0}^t \Phi(t, q)B(q)u(q)dq + D(t)u(t), \quad (116)$$

where $\Phi(t, t_0)$ is the state transition matrix [28]. Using (116), the left-hand side of the strong observability condition in (26) can be expressed as

$$\begin{aligned} \int_{t-T}^t \|y(x(t), u(t)) - y(x'(t), u(t))\|^2 dt &= \int_{t-T}^t \|C(q)\Phi(q, t-T)x_0 - C(q)\Phi(q, t-T)x'_0\|^2 dq \\ &= (x_0 - x'_0)^\top W_O(t, t-T)(x_0 - x'_0) \\ &\geq \lambda_{\min}(W_O(t, t-T))\|x_0 - x'_0\|_2^2 \end{aligned}$$

where $W_O(t, t-T)$ is the observability Grammian for (114). The LTV system (114) is observable over $[t-T, t]$ if and only if the observability Grammian $W_O(t, t-T)$ is positive definite, i.e., if and only if $\lambda_{\min}(W_O(t, t-T)) > 0$ [28]. Setting $\gamma = \lambda_{\min}(W_O(t, t-T))$, the strong observability condition in (26) is thus equivalent to observability for LTV systems.

APPENDIX C

In this section, details of the 2004 Toyota Prius ICE, battery pack, vehicle dynamics, mechanical power split device, maximum drive power, and electrical bus component models are described.

A. Internal Combustion Engine

The 2004 Toyota Prius powertrain has a 57 kW ICE with operating range between 1000 and 5000 rpm [29]. Broadening the power flow modeling ideas in [30], [31], the power dynamics are represented by two first-order lag equations:

$$\frac{dP_{fuel}}{dt} = \frac{-1}{\tau_{fuel}}P_{fuel} + \frac{1}{\tau_{fuel}}P_{fuel}^{max}(\omega_{ice})u_{fuel} \quad (117)$$

$$\frac{dP_{ice}}{dt} = \frac{-1}{\tau_{ice}}P_{ice} + \frac{1}{\tau_{ice}}\eta_{ice}(P_{ice}, \omega_{ice})P_{fuel}. \quad (118)$$

Equation (117) describes the fuel delivery dynamics with P_{fuel} the engine fuel power, $P_{fuel}^{max}(\omega_{ice})$ is the maximum available fuel power for a given engine angular velocity ω_{ice} where the control $u_{fuel} \in [0, 1]$ modulates $P_{fuel}^{max}(\omega_{ice})$, and τ_{fuel} is the fuel delivery system lag [30], [31]. In (118), P_{ice} is the engine mechanical output power, τ_{ice} is the average engine power lag due to combustion delay and crankshaft and flywheel inertias [30]–[32]; $\eta_{ice}(P_{ice}, \omega_{ice})$ is the combined efficiency of the combustion and engine

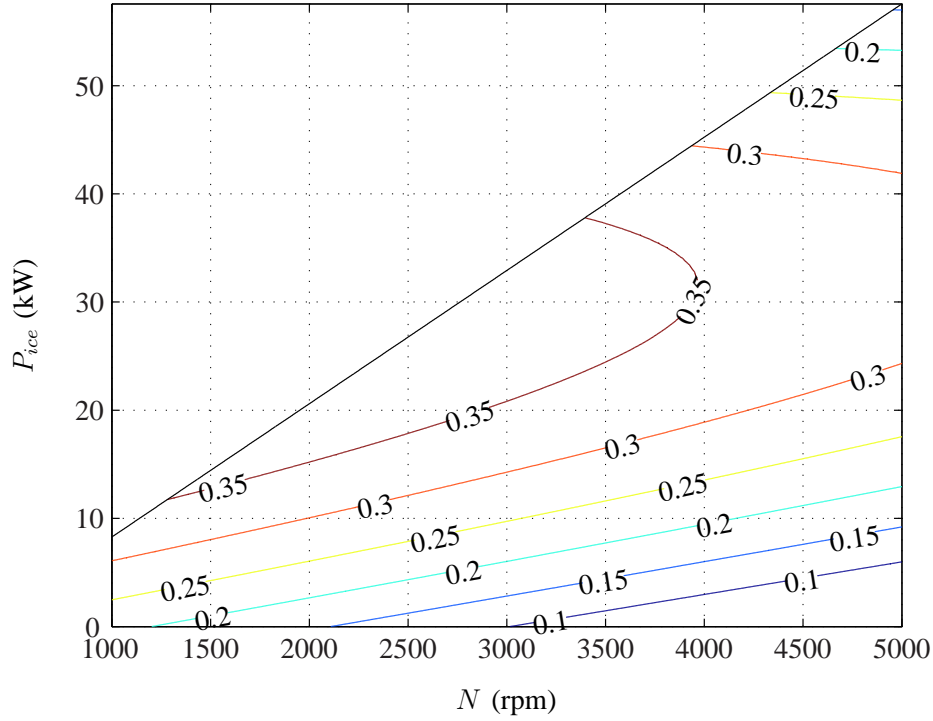


Fig. 36. Prius ICE power output versus speed with fuel efficiency regions.

mechanical power delivery in which $\eta_{ice}(P_{ice}, \omega_{ice})P_{fuel}(\omega_{ice})$ represents the indirectly commanded engine output power through the operation of the fuel delivery system. It follows that

$$P_{fuel}^{max}(\omega_{ice}) = \frac{P_{ice}^{max}(\omega_{ice})}{\eta_{ice}(P_{ice}^{max}, \omega_{ice})} \quad (119)$$

completes the specification of the variables. Values for P_{ice}^{max} and η_{ice} are determined by least squares fits of appropriate engine data in [29]. Here, the functions

$$P_{ice}^{max}(\omega_{ice}) = \alpha_1 \bar{\omega}_{ice} + \alpha_0 \quad (120)$$

$$\eta_{ice}(P_{ice}, \omega_{ice}) = \beta_{20} \bar{P}_{ice}^2 + \beta_{11} \bar{P}_{ice} \bar{\omega}_{ice} + \beta_{10} \bar{P}_{ice} + \beta_{01} \bar{\omega}_{ice} + \beta_{00} \quad (121)$$

are sufficient where $\bar{\omega}_{ice} = \omega_{ice} / \max(\omega_{ice})$ and $\bar{P}_{ice} = P_{ice} / \max(P_{ice}^{max})$ are normalized by their maximum values for numerical solution purposes. Table VII lists the fit coefficients.

Further, the ICE angular velocity is expressed using $\Omega_{ice} = \omega_{ice}^2$ by the conservation of power equation:

$$\frac{1}{2} J_{ice} \frac{d\Omega_{ice}}{dt} = P_{ice,psd} + P_{ice} \quad (122)$$

Note $\Omega_{ice} = \omega_{ice}^2$ defines a Lyapunov energy function $P_{ice,psd}$ is the soon to be developed power routed through the power split device, and $J_{ice} = 0.13 \text{ kg}\cdot\text{m}^2$ [33] is the estimated rotational inertia of the engine; $\omega_{ice} = +\sqrt{\Omega_{ice}}$ because the engine turns in only one direction.

TABLE VII
TOYOTA PRIUS ENGINE MAXIMUM OUTPUT POWER AND EFFICIENCY FIT COEFFICIENTS.

Parameter	Value
α_1	61.609
α_0	-4.0470
β_{20}	-0.98686
β_{11}	0.25973
β_{10}	0.88661
β_{01}	-0.27567
β_{00}	0.26627

B. Battery

The Prius powertrain has a 21 kW discharge/charge power NiMH battery pack that provides a secondary power source and allows the capture and storage of excess vehicle kinetic energy via regenerative braking. The battery's state of charge (SOC), \overline{W}_{bat} , dynamics are represented with a validated empirical formula [34], which has been modified [23] to include an additional quadratic power term to more accurately represent the 7.2 V 6.5 Ah 6-cell NiMH modules [35], [36] used herein:

$$\frac{d\overline{W}_{bat}}{dt} = - \left[-\ln(\overline{W}_{bat} + c_{b,1}^{v_b}) + c_{b,2}^{v_b} \frac{P_{bat}^{v_b}}{n_b} + c_{b,3}^{v_b} + c_{b,4}^{v_b} \left(\frac{P_{bat}^{v_b}}{n_b} \right)^2 \right] \frac{P_b^{v_b}}{n_b W_{bat}^{max}} \quad (123)$$

In (123), P_{bat} is the battery power input, W_{bat}^{max} is the battery's maximum rated storage energy; n_b is the number of battery modules in the pack; $v_b = d$, $P_{bat}^d \geq 0$, for discharge; $v_b = c$, $P_{bat}^c \leq 0$, for charge; and $c_{b,i}^d/c_{b,i}^c$, $i = \{1, 2, 3, 4\}$ are discharge/charge coefficients obtained by the least-squares fit of instantaneous power efficiencies produced using NiMH module battery data in [35], [36] and efficiency relationships in [37]. Table VIII lists the battery model parameters. Further, the Prius battery state of charge is restricted to $\overline{W}_{bat} \in [0.4, 0.8]$ [38].

C. Vehicle

Vehicle dynamics have been described with a point-mass, linear motion dynamical model [23], [31]. However, when this model has an input of power, a singularity occurs at zero velocity. To eliminate this singularity and develop a vehicle dynamics model consistent with our power flow approach, a Lyapunov

TABLE VIII
TOYOTA PRIUS NIMH BATTERY PACK MODEL PARAMETERS.

Parameter	Discharge ($v_b = d$)	Charge ($v_b = c$)
W_b^{max}	1.6848×10^2 kJ	1.6848×10^2 kJ
n_b	28	28
$c_{b,1}^{v_b}$	4.5077	49.511
$c_{b,2}^{v_b}$	-0.84091	0.29369
$c_{b,3}^{v_b}$	2.7023	4.9132
$c_{b,4}^{v_b}$	3.6526	0.10087

energy function is defined, $\Upsilon_v = v^2$ where v is velocity. Thus, the conservation of power to vehicle motion results in the power flow dynamical model

$$\begin{aligned}
\frac{1}{2}m_v \frac{d\Upsilon_v}{dt} &= P_d(v) + P_{rr}(v, \theta_r) + P_b(\theta_r) \\
&\quad + P_{2,L} + P_{whl,psd} - P_{brk} \\
P_d(v) &= v \cdot (-0.5\rho_{air}A_{fr}C_d v^2 \text{sgn}(v)) \\
P_{rr}(v, \theta_v) &= v \cdot (-C_{rr}m_v g \cos(\theta_v) \text{sgn}(v)) \\
P_b(\theta_v) &= v \cdot (-m_v g \sin(\theta_v))
\end{aligned} \tag{124}$$

where $v = +\sqrt{\Upsilon_v}$ considering only forward motion, $P_d(v)$ is the drag force power, P_{rr} is the rolling resistance, P_b is the body force power due to gravity, $P_{whl,psd}$ is the wheel power from/to the power split device defined shortly, P_{brk} is the frictional braking power, ρ_{air} is the ambient air density, m_v is the total vehicle mass, A_{fr} is the vehicle frontal area, C_d is the drag coefficient, C_{rr} is the tire rolling resistance coefficient, and θ_v is the road grade angle. Table IX lists the Prius vehicle parameters.

The frictional braking power, P_{brk} , is equal to a maximum velocity-dependent braking power modulated by $u_{brk} \in [0, 1]$; the maximum braking power depends upon a smooth function that increases with velocity until a maximum of 50 kW braking power is achieved. Specifically,

$$P_{brk} = P_{brk}^{max}(\Upsilon_v)u_{brk} = 50 \tanh\left(\frac{\sqrt{\Upsilon_v}}{5}\right)u_{brk} \tag{125}$$

TABLE IX
TOYOTA PRIUS VEHICLE DYNAMICS MODEL PARAMETERS.

Parameter	Value
A_{fr}	2.33 m ² [38]
C_d	0.26 [38]
C_{rr}	0.00475 [39]
m_v	1469 kg ⁷ [38]
ρ_{air}	1.225 kg/m ³

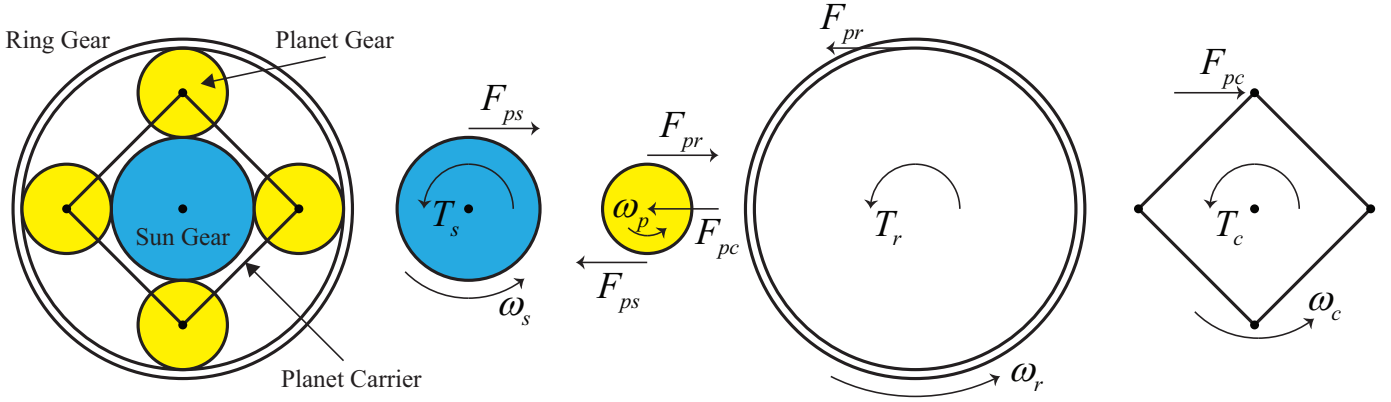


Fig. 37. Mechanical power split device sun-planet-ring gear system.

D. Mechanical Power Split Device

The power split device (PSD) mechanically connects the ICE, generator electric drive (SPMSM1), and traction electric drive system (SPMSM2) via a planetary gear system, displayed in Figure 37, to propel the vehicle, charge the battery, and startup the ICE. Specifically, the planetary carrier is affixed to the output of the ICE; the generator electric drive system, SPMSM1, rotor is attached to the sun gear; and the ring gear is connected to the traction electric drive system, SPMSM2, rotor, which is linked (via additional gears) to the the drive wheels. The planetary gear system dynamics are analyzed to develop the aforementioned $P_{ice,psd}$ and $P_{whl,psd}$ in (122) and (124), respectively:

$$P_{ice,psd} = \frac{(r_s + r_r)}{r_s} \left(\frac{P_{1,L}}{|\omega_{1,m}| + \epsilon_s} \right) \omega_{ice} \quad (126)$$

$$P_{whl,psd} = - \frac{r_r \gamma}{r_s} \left(\frac{P_{1,L}}{|\omega_{1,m}| + \epsilon_s} \right) v \quad (127)$$

where r_s is the sun gear radius, r_r is the radius of the ring gear, $\omega_{1,m}$ is the angular velocity of the sun gear and SPMSM1 (which are directly coupled), ϵ_s is a small constant $\ll 1$ to prevent division by zero,

and γ relates the vehicle velocity to the ring gear angular velocity, i.e., $\omega_r = \gamma v$. To begin developing (126) and (127), the dynamics of the PSD with the ring gear connected to the drive wheels are set forth in the context of Figure 37 where the four planet gears are assumed to experience the same forces and thus can be replaced with a single planet gear with combined mass and inertia:

$$J_s \frac{d\omega_{1,m}}{dt} = T_s - F_{ps} r_s \quad (128)$$

$$4J_p \frac{d\omega_p}{dt} = -F_{pr} r_p - F_{ps} r_p \quad (129)$$

$$4m_p \frac{dv_p}{dt} = F_{ps} - F_{pr} + F_{pc} \quad (130)$$

$$J_c \frac{d\omega_c}{dt} = -(r_s + r_p) F_{pc} + T_c \quad (131)$$

$$m_v \frac{dv}{dt} = r_r \gamma F_{pr} + \frac{P_d + P_{rr} + P_b + P_{2,L} - P_{brk}}{v} \quad (132)$$

The torque from/to SPMSM1 is denoted by T_s ; T_c is the torque supplied by the ICE; J_s , J_p , and J_c are the rotational inertias of the sun gear, planet gear, and planet carrier, respectively; ω_p and v_p are the planet gear angular and translational velocities, respectively; and F_{ps} , F_{pr} , and F_{pc} are the forces at the interface of the sun and planet gears, ring and planet gears, and carrier and planet gear, respectively. Equation (132) is based on knowledge that the force transferred to the ring gear is that which propels the vehicle (along with SPMSM2) and the assumption that the ring gear inertia is negligible compared to the overall vehicle. We note (i) $r_p = (r_r - r_s)/2$, (ii) the planet carrier has the same angular velocity as the ICE, i.e., $\omega_c = \omega_{ice}$, and (iii) the planet carrier inertia includes the carrier itself plus that of the ICE since they are joined together and we assume that the planet inertia is small compared to that of the engine, thus totality can be described with J_{ice} . Further, we take J_p , m_p , J_s as negligible compared to the vehicle inertia and planetary carrier/ICE inertia. After applying the previous and algebraic manipulations, we obtain

$$J_{ice} \frac{d\omega_{ice}}{dt} = \frac{r_r + r_s}{r_s} T_s + T_c \quad (133)$$

$$m_v \frac{dv}{dt} = \frac{-r_r \gamma}{r_s} T_s + \frac{P_d + P_{rr} + P_b + P_{2,L} - P_{brk}}{v} \quad (134)$$

Next, we relate the sun gear torque to the SPMSM1 power applied using $T_s = P_{1,L}/(|\omega_{1,m}| + \epsilon_s)$; $P_{1,L}$ is divided by the absolute value of $\omega_{1,m}$ to obtain the expected response of the ICE and vehicle given that both $P_{1,L}$ and $\omega_{1,m}$ can take positive and negative values. For example, (i) if $P_{1,L}$ is negative, power

TABLE X
TOYOTA PRIUS MECHANICAL POWER SPLIT DEVICE MODEL PARAMETERS.

Parameter	Value
r_r	78 teeth [40]
r_s	30 teeth [40]
γ	14.2097 rad·s/(m·s) [40]

is being consumed by SPMSM1 and one expects the ICE speed to go down regardless of the sign of $\omega_{1,m}$ (assuming T_c is constant), and (ii) if $P_{1,L}$ is positive, SPMSM1 is starting the ICE and its speed is expected to increase regardless of the sign of $\omega_{1,m}$. Finally, applying the expression for T_s , recognizing $T_c\omega_c = P_{ice}$, recasting (133) and (134) into power flow equations, and employing Lyapunov energy functions, $\Omega_{ice} = \omega_{ice}^2$ and $\Upsilon_v = v^2$, results in

$$\begin{aligned} \frac{1}{2}J_{ice}\frac{d\Omega_{ice}}{dt} &= \frac{(r_r + r_s)}{r_s} \left(\frac{P_{1,L}}{|\omega_{1,m}| + \epsilon_s} \right) \omega_{ice} + P_{ice} \\ &= P_{ice,psd} + P_{ice} \end{aligned} \quad (135)$$

$$\begin{aligned} \frac{1}{2}m_v\frac{d\Upsilon_v}{dt} &= -\frac{r_r\gamma}{r_s} \left(\frac{P_{1,L}}{|\omega_{1,m}| + \epsilon_s} \right) v + P_d + P_{rr} + P_b + P_{2,L} - P_{brk} \\ &= P_{whl,psd} + P_d + P_{rr} + P_b + P_{2,L} - P_{brk} \end{aligned} \quad (136)$$

verifying $P_{ice,psd}$ and $P_{whl,psd}$ in (126) and (127), respectively.

Additionally, an expression for $\omega_{1,m}$ is needed to determine $P_{ice,psd}$ and $P_{whl,psd}$. Gears sharing a point of contact have the same tangential velocity at that point, thus $\omega_{1,m}$ is available from

$$r_s\omega_{1,m} + r_r\gamma v = (r_r + r_s)\omega_{ice} \quad (137)$$

Table X displays the PSD parameters used herein. The PSD gear radii are given in terms of number of gear teeth rather than length because the gear pitch is unknown and the pitch cancels out of the $P_{ice,psd}$ and $P_{whl,psd}$ expressions under the assumption all the gears have the same pitch.

E. SPMSM1 and SPMSM2

Sections VII-B and VII-C provided the SPMSM1 and SPMSM2 efficiency maps development, respectively, for power flow modeling. In addition, expressions for maximum power are also needed.

1) *SPMSM1 Maximum Power*: To complete the supervisory level power flow model for SPMSM1 started in Section VII-B, expressions for the maximum mechanical and electrical power are needed. The maximum mechanical power during propelling and generating is modeled from given maximum torque versus angular velocity information with the maximum power modified by mildly extending the zero speed power to 1 kW so engine start up is possible from zero speed and adding a curve segment centered at the torque region boundary at 60π rad/s to obtain a continuous first derivative function of $\omega_{1,m}$:

$$P_{1,L}^{max}(\omega_{1,m}) = \begin{cases} 0.1547\omega_{1,m} + 1, & 0 \leq \omega_{1,m} \leq 1798\pi/30 \text{ rad/s} \\ 1.061 \times 10^{-7}\omega_{1,m}^3 - 0.1847\omega_{1,m}^2 \\ + 69.68\omega_{1,m} - 6.544 \times 10^3, & 1798\pi/30 < \omega_{1,m} \leq 1802\pi/30 \text{ rad/s} \\ 30.16, & 1802\pi/30 < \omega_{1,m} \leq 1000\pi/3 \text{ rad/s} \end{cases} \quad (138)$$

The maximum electrical power during propelling (generating is not needed in the supervisory level model) is obtained from the efficiency and maximum mechanical power:

$$P_{1,inv}^{max}(\omega_{1,m}) = \frac{P_{1,L}^{max}(\omega_{1,m})}{\eta_{SPMSM1,prop}(P_{1,L}^{max}(\omega_{1,m}), \omega_{1,m})} \quad (139)$$

2) *SPMSM2 Maximum Power*: To complete the supervisory level power flow model for SPMSM2 started in Section VII-C, expressions for the maximum mechanical and electrical power are needed for the no fault and ITSC faulted cases. When there is no fault, the maximum mechanical power during propelling and generating is modeled from given maximum torque versus angular velocity information where the maximum power is modified by mildly extending the zero speed power to 3 kW so vehicle movement is possible from zero speed and adding a curve segment centered at the torque region boundary at 40π rad/s to obtain a continuous first derivative function of $\omega_{2,m}$:

$$P_{2,L}^{max}(\omega_{2,m}) = \begin{cases} 0.3761\omega_{2,m} + 3, & 0 \leq \omega_{2,m} \leq 1198\pi/30 \text{ rad/s} \\ -8.2869 \times 10^{-5}\omega_{2,m}^3 - 0.4783\omega_{2,m}^2 \\ + 124.3\omega_{2,m} - 7.853 \times 10^3, & 1198\pi/30 < \omega_{2,m} \leq 1202\pi/30 \text{ rad/s} \\ 1.848 \times 10^{-5}\omega_{2,m}^2 - 2.927 \times 10^{-2}\omega_{2,m} + 53.65, & 1202\pi/30 < \omega_{2,m} \leq 200 \text{ rad/s} \end{cases} \quad (140)$$

TABLE XI
SPMSM2 MAXIMUM MECHANICAL POWER CURVE FIT COEFFICIENTS

Deg of fault σ	a	b	c	d
0.005	4.663×10^{-10}	0.3241	1.048×10^{-3}	-1.272×10^{-5}
0.01	1.985×10^{-9}	0.3057	2.105×10^{-3}	-2.956×10^{-5}
0.02	5.445×10^{-9}	0.2713	3.862×10^{-3}	-6.438×10^{-5}
0.05	0.7528	0.2301	7.251×10^{-3}	-1.685×10^{-4}

Maximum mechanical power data at each ITSC fault level is obtained from the control simulations in Section VII-C1. This maximum power data at each fault level is approximated using a cubic equation with coefficients determined via a least-squares data fit:

$$P_{2,L}^{max}(\omega_{2,m}, \sigma) = a(\sigma) + b(\sigma)\omega_{2,m} + c(\sigma)\omega_{2,m}^2 + d(\sigma)\omega_{2,m}^3 \quad (141)$$

where Table XI lists the fit coefficients found for each fault level.

The maximum electrical power during propelling (generating is not needed in the supervisory level model) is obtained from the efficiency and maximum mechanical power:

$$P_{2,inv}^{max}(\omega_{2,m}) = \frac{P_{2,L}^{max}(\omega_{2,m})}{\eta_{SPMSM2,prop}(P_{2,L}^{max}(\omega_{2,m}), \omega_{2,m})} \quad (142)$$

F. Electrical Bus

The battery pack, SPMSM1, and SPMSM2 electrical power flows come together in the DC-Inverter. Both of the drives electrical power values include the inverter efficiency, which is assumed to also include an electrical bus losses. Thus the electrical bus is taken as having loss-less power transfer efficiency, resulting in

$$P_{bat} = P_{1,e} + P_{2,e} \quad (143)$$

G. Interconnection Equations

Interconnection equations are constraints for each mode that relate the states, algebraic variables, and continuous control inputs. First, the SPMSM1 electrical and mechanical connections are

$$P_{1,e}^i = \begin{cases} P_{1,e}^{max}(\omega_{1,m})u_1^i, & i = 1 \\ \eta_{1,inv}\eta_{SPMSM1,gen}(P_{1,L}^i, \omega_{1,m})P_{1,L}^i, & i = 2, 3, 4 \end{cases} \quad (144)$$

$$P_{1,L}^i = \begin{cases} \eta_{1,inv}\eta_{SPMSM1,prop}(P_{1,e}^i, \omega_{1,m})P_{1,e}^i, & i = 1 \\ P_{1,L}^{max}(\omega_{1,m})u_1^i, & i = 2, 3, 4 \end{cases} \quad (145)$$

with $\omega_{1,m}$ available from (137) and inverter efficiency, $\eta_{1,inv}$, of 0.98. Note that the maximum electrical power here is the inverter power divided by the inverter efficiency, i.e., $P_{1,e}^{max}(\cdot) = P_{1,inv}^{max}(\cdot)/\eta_{1,inv}$.

Next, the SPMSM2 electrical and mechanical connections are

$$P_{2,e}^i = \begin{cases} P_{2,e}^{max}(\omega_{2,m})u_2^i, & i = 1, 2, 3 \\ \eta_{2,inv}\eta_{SPMSM2,gen}(P_{2,L}^i, \omega_{2,m})P_{2,L}^i, & i = 4 \end{cases} \quad (146)$$

$$P_{2,L}^i = \begin{cases} \eta_{2,inv}\eta_{SPMSM2,prop}(P_{2,e}^i, \omega_{2,m})P_{2,e}^i, & i = 1, 2, 3 \\ P_{2,L}^{max}(\omega_{2,m})u_2^i, & i = 4 \end{cases} \quad (147)$$

where the inverter efficiency is $\eta_{2,inv} = 0.98$. Note that the maximum electrical power here is the inverter power divided by the inverter efficiency, i.e., $P_{2,e}^{max}(\cdot) = P_{2,inv}^{max}(\cdot)/\eta_{2,inv}$.

The electrical bus connections for each mode are

$$P_{bat}^i = P_{1,e}^i + P_{2,e}^i \quad (148)$$

The power split device mechanical power connections are

$$P_{ice,psd}^i = \frac{(r_s + r_r)}{r_s} \left(\frac{P_{1,L}^i}{|\omega_{1,m}| + \epsilon_s} \right) \omega_{ice}, \quad i = 1, 2, 3, 4 \quad (149)$$

$$P_{whl,psd}^i = -\frac{r_r\gamma}{r_s} \left(\frac{P_{1,L}^i}{|\omega_{1,m}| + \epsilon_s} \right) v, \quad i = 1, 2, 3, 4 \quad (150)$$

Finally, the frictional braking power interconnection equations are

$$P_{brk}^i = P_{brk}^{max}(\Upsilon_v)u_{brk}^i, \quad i = 1, 2, 3, 4 \quad (151)$$

H. Engine Operation

The Prius ICE is not always on when the vehicle is operating. The engine is started if the reference velocity is nonzero and nondecreasing and any of the following conditions are met:

ES1) The battery SOC is below a threshold at $t_{p,0}$:

$$\overline{W}_{bat}(t_{p,0}) < \overline{W}_{bat,ice-on} = 0.50 \quad (152)$$

ES2) The estimated wheel power needed to meet the reference velocity is greater than what can be supplied by the traction motor, SPMSM2, alone from $t_{p,0}$ to $t_{p,f}$:

$$P_{2,L}^{max}(\omega_{r,ref}(t_{p,0} + \Delta t)) < \hat{P}_{whl}(t_{p,0} + \Delta t) \quad (153)$$

where $\Delta t \in [0, t_{p,f} - t_{p,0}]$ and $\omega_{r,ref}(t_{p,0} + \Delta t) = \gamma v_{ref}(t_{p,0} + \Delta t)$. The estimated power, \hat{P}_{whl} , is assumed to be piecewise-constant over $[t_{p,0}, t_{p,f}]$. Values are chosen using the shooting method such that the output of (124) tracks the square of the reference velocity within a negligible error.

ES3) The estimated electrical power needed by SPMSM2 exceeds that which can be supplied by the battery alone over $[t_{p,0}, t_{p,f}]$:

$$P_{2,e}(\omega_{r,ref}(t_{p,0} + \Delta t)) > P_{bat}^{d,max} = 21 \text{ kW} \quad (154)$$

The engine is turned off if all of the following conditions are satisfied:

EO1) Either the battery SOC has reached the nominal value,

$$\overline{W}_{bat}(t_{p,0}) \geq \overline{W}_{bat}^{nom} = 0.58, \quad (155)$$

or the reference velocity is decreasing at a rate below a threshold over a time interval,

$$\frac{dv_{ref}(t_{p,0} + \Delta t)}{dt} < a_{ice-off} = -0.5 \text{ m/s}^2, . \quad (156)$$

EO2) The estimated power needed to meet the reference velocity is less than or equal to what can be supplied by SPMSM2 over a time interval:

$$P_{2,L}^{max}(\omega_{r,ref}(t_{p,0} + \Delta t)) \geq \hat{P}_{whl}(t_{p,0} + \Delta t). \quad (157)$$

EO3) The estimated electrical power needed by SPMSM2 is less than or equal to what can be supplied by the battery alone over a time interval:

$$P_{2,e}(\omega_{r,ref}(t_{p,0} + \Delta t)) \leq P_{bat}^{d,max} = 21 \text{ kW}. \quad (158)$$

Practically, when the engine is off, only modes 1 and 4 are possible; modes 2 and 3 should be unavailable until the engine has finished start up and is on. Further, when the engine is off no fuel usage or power output is expected, thus

$$\alpha_2, \alpha_3 = 0 \quad (159)$$

$$u_{fuel}, P_{fuel}, P_{ice} = 0 \quad (160)$$

Upon the above conditions being met to start the engine, the ICE is driven up to speed by requiring that it have the minimum ICE operating speed of $100\pi/3$ rad/s after a certain time, $\Delta_{ice,start}$, i.e.,

$$\Omega_{ice}(t_{ice}) \geq \left(\frac{100\pi}{30}\right)^2, \quad t_{ice} \geq t_{p,0} + \Delta_{ice,start}, \quad \Delta_{ice,start} = 0.25 \text{ s}, \quad (161)$$

and allowing $u_{fuel}, P_{fuel}, P_{ice} \geq 0$. Once the engine has started and reached minimum operating speed, mode 1 is no longer permitted, $\alpha_1 = 0$, until the engine is off again.

Consequent to the ICE off, $u_{fuel}, P_{fuel}, P_{ice} = 0$. The power values immediately go to zero because the fuel from which power is derived is no longer input.

REFERENCES

- [1] P. Krause, O. Wasynczuk, S. Sudhoff, and P. Pekarek, *Analysis of Electric Machinery and Drive Systems*, 3rd ed. Piscataway, NJ: Wiley-IEEE Press, 2013.
- [2] C. Lai, A. Balamurali, V. Bousaba, K. L. V. Iyer, and N. C. Kar, "Analysis of stator winding inter-turn short-circuit fault in interior and surface mounted permanent magnet traction machines," in *2014 IEEE Transp. Electr. Conf. Expo.* IEEE, June 2014, pp. 1–6.
- [3] A. Gandhi, T. Corrigan, and L. Parsa, "Recent advances in modeling and online detection of stator interturn faults in electrical motors," *IEEE Trans. Ind. Electron.*, vol. 58, no. 5, pp. 1564–1575, 2011.
- [4] L. Romeral, J. C. Urresty, J. R. Riba Ruiz, and A. Garcia Espinosa, "Modeling of surface-mounted permanent magnet synchronous motors with stator winding interturn faults," *IEEE Trans. Ind. Electron.*, vol. 58, no. 5, pp. 1576–1585, 2011.
- [5] H. Michalska and D. Mayne, "Moving horizon observers and observer-based control," *IEEE Trans. Automat. Contr.*, vol. 40, no. 6, pp. 995–1006, jun 1995. [Online]. Available: <http://ieeexplore.ieee.org/lpdocs/epic03/wrapper.htm?arnumber=388677>
- [6] R. Meyer, R. DeCarlo, P. Meckl, C. Doktorcik, and S. Pekarek, "Hybrid model predictive power flow control of a fuel cell-battery vehicle," in *Am. Control Conf.*, 2011, pp. 2725–2731[1]. [Online]. Available: <http://ieeexplore.ieee.org/stamp/stamp.jsp?tp=&arnumber=5991428&isnumber=5989965>
- [7] R. T. Meyer, R. A. DeCarlo, and S. Pekarek, "Hybrid model predictive power management of a battery-supercapacitor electric vehicle," *Asian Journal of Control*, vol. 18, no. 1, pp. 150–165, 2016, asjc.1259. [Online]. Available: <http://dx.doi.org/10.1002/asjc.1259>
- [8] K. Uthaichana, R. DeCarlo, S. Benga, S. Pekarek, and M. Zefran, "Hybrid optimal theory and predictive control for power management in hybrid electric vehicle," *J. Nonlinear Syst. Appl.*, vol. 2, no. 1-2, pp. 96–110, 2011.

- [9] R. Vidal, A. Chiuso, S. Soatto, and S. Sastry, "Observability of Linear Hybrid Systems," in *Hybrid Syst. Comput. Control*. Springer Berlin/Heidelberg, 2003, pp. 526–539.
- [10] S. C. Johnson, R. A. DeCarlo, and M. Zefran, "Set-transition observability of switched linear systems," in *2014 Am. Control Conf.* IEEE, jun 2014, pp. 3267–3272. [Online]. Available: <http://ieeexplore.ieee.org/lpdocs/epic03/wrapper.htm?arnumber=6858960>
- [11] M. Babaali and G. J. Pappas, "Observability of switched linear systems in continuous time," *Hybrid Syst. Comput. Control*, vol. 3414, no. March, pp. 103–117, 2005. [Online]. Available: <http://www.springerlink.com/index/150UC4MJQW7AJAE9.pdf>
- [12] D. Gomez-Gutierrez, A. Ramirez-Trevino, J. Ruiz-Leon, and S. Di Gennaro, "On the Observability of Continuous-Time Switched Linear Systems Under Partially Unknown Inputs," *IEEE Trans. Automat. Contr.*, vol. 57, no. 3, pp. 732–738, mar 2012. [Online]. Available: <http://ieeexplore.ieee.org/lpdocs/epic03/wrapper.htm?arnumber=6007052>
- [13] K.-H. Kim, D.-U. Choi, B.-G. Gu, and I.-S. Jung, "Fault model and performance evaluation of an inverter-fed permanent magnet synchronous motor under winding shorted turn and inverter switch open," *IET Electr. Power Appl.*, vol. 4, no. 4, p. 214, 2010.
- [14] D. Luenberger, *Introduction to dynamic systems: theory, models, and applications*, 1979.
- [15] A. Alessandri, M. Baglietto, G. Battistelli, and V. Zavala, "Advances in moving horizon estimation for nonlinear systems," *49th IEEE Conf. Decis. Control*, pp. 5681–5688, dec 2010. [Online]. Available: <http://ieeexplore.ieee.org/lpdocs/epic03/wrapper.htm?arnumber=5718126>
- [16] Y. Guo and B. Huang, "Moving horizon estimation for switching nonlinear systems," *Automatica*, vol. 49, pp. 3270–3281, 2013.
- [17] G. Ferrari-Trecate, D. Mignone, and M. Morari, "Moving horizon estimation for hybrid systems," *IEEE Trans. Automat. Contr.*, vol. 47, pp. 1663–1676, 2002.
- [18] S. Bengea, K. Uthachana, M. Žefran, and R. DeCarlo, "Optimal Control of Switching Systems via Embedding into Continuous Optimal Control Problem," in *Control Syst. Handbook, Second Ed.*, W. S. Levine, Ed. CRC Press 2011, 2010, ch. 31, pp. 31–1–31–23.
- [19] S. C. Bengea and R. a. DeCarlo, "Optimal control of switching systems," *Automatica*, vol. 41, no. 1, pp. 11–27, jan 2005. [Online]. Available: <http://linkinghub.elsevier.com/retrieve/pii/S0005109804002237>
- [20] M. Bodson, J. Chiasson, and R. Novotnak, "A systematic approach to selecting flux references for torque maximization in induction motors," *IEEE Trans. Control Syst. Technol.*, vol. 3, no. 4, pp. 388–397, 1995. [Online]. Available: <http://ieeexplore.ieee.org/lpdocs/epic03/wrapper.htm?arnumber=481963>
- [21] O. Wasynczuk, S. Sudhoff, K. Corzine, J. Tichenor, P. Krause, I. Hansen, and L. Taylor, "A maximum torque per ampere control strategy for induction motor drives," *IEEE Trans. Energy Convers.*, vol. 13, no. 2, pp. 163–169, jun 1998. [Online]. Available: <http://ieeexplore.ieee.org/lpdocs/epic03/wrapper.htm?arnumber=678980>
- [22] R. T. Meyer, M. Zefran, and R. A. DeCarlo, "A Comparison of the Embedding Method With Multiparametric Programming, Mixed-Integer Programming, Gradient-Descent, and Hybrid Minimum Principle-Based Methods," *IEEE Trans. Control Syst. Technol.*, vol. 22, no. 5, pp. 1784–1800, sep 2014. [Online]. Available: <http://ieeexplore.ieee.org/lpdocs/epic03/wrapper.htm?arnumber=6733440>
- [23] R. Meyer, R. DeCarlo, and P. Meckl, "Hybrid Model Predictive Power Management of a Fuel-Cell Battery Vehicle," *Asian Journal of Control*, vol. 15, no. 2, pp. 363–379, March 2013.
- [24] W. Harrington and A. Krupnick, "Improving fuel economy in heavy duty vehicles," Issue Brief 12-01. Resources for the Future, Tech. Rep., 2012.
- [25] Caterpillar, "D7E." [Online]. Available: http://www.cat.com/en_US/products/rental/equipment/dozers/medium-dozers/18429156.html

- [26] Deere & Company, “644K Hybrid Wheel Loader.” [Online]. Available: https://www.deere.com/en_US/products/equipment/wheel_loaders/644k_hybrid/644k_hybrid.page
- [27] R. T. Meyer, S. C. Johnson, R. A. DeCarlo, and S. Pekarek, “Supervisory powerflow control of Toyota Prius subject to stator winding faults,” *In Preperation*, 2016.
- [28] R. A. DeCarlo, *Linear Systems: A State Variable Approach with Numerical Implementation*. Englewood Cliffs, New Jersey: Prentice Hall, 1989.
- [29] K. Muta, M. Yamazaki, and J. Tokieda, “Development of New-Generation Hybrid System THS II-Drastic Improvement of Power Performance and Fuel Economy,” *SAE Paper 2004-01-0064*, 2004.
- [30] K. Uthaichana, “Modeling and Control of a Parallel Hybrid Electric Vehicle,” Ph.D. dissertation, Purdue University, 2006.
- [31] K. Uthaichana, R. A. DeCarlo, S. C. Benga, S. Pekarek, and M. Žefran, “Hybrid optimal theory and predictive control for power management in hybrid electric vehicle,” *Journal of Nonlinear Systems and Applications*, vol. 2, no. 1 -2, pp. 96–110, 2011.
- [32] L. Guzzella and A. Amstutz, “Control of Diesel Engines,” *IEEE Control Systems Magazine*, vol. 18, no. 5, pp. 53–71, 1998.
- [33] C. Mansour and D. Clodic, “Dynamic Modeling of the Electro-Mechanical Configuration of the Toyota Hybrid System Series/Parallel Power Train,” *International Journal of Automotive Technology*, vol. 13, no. 1, pp. 143–166, 2012.
- [34] V. Agarwal, K. Uthaichana, R. A. Decarlo, and L. H. Tsoukalas, “Development and validation of a battery model useful for discharging and charging power control and lifetime estimation,” *IEEE Transactions on Energy Conversion*, vol. 25, no. 3, pp. 821–835, 2010. [Online]. Available: <http://dx.doi.org/10.1109/TEC.2010.2043106>
- [35] V. Johnson, “Battery Performance Models in ADVISOR,” *Journal of Power Sources*, vol. 110, pp. 321 – 329, 2002.
- [36] T. Markel, A. Brooker, T. Hendricks, V. Johnson, K. Kelly, B. Kramer, A. O’Keefe, S. Sprick, and K. Wipke, “Advisor: a systems analysis tool for advanced vehicle modeling,” *Journal of Power Sources*, vol. 110, no. 2, pp. 255–266, August 2002. [Online]. Available: [http://dx.doi.org/10.1016/S0378-7753\(02\)00189-1](http://dx.doi.org/10.1016/S0378-7753(02)00189-1)
- [37] H. L. N. Wiegman and A. J. A. Vandenput, “Battery State Control Techniques for Charge Sustaining Applications,” *SAE Paper 981129*, 1998.
- [38] E. Nam, “Advanced Technology Vehicle Modleing in PERE,” United States Environmental Protection Agency, EPA420-D-04-002, March 2004.
- [39] J. Meisel, “An Analytic Foundation for the Toyota Prius THS-II Powertrain with a Comparison to a Strong Parallel Hybrid-Electric Powertrain,” *SAE Paper 2006-01-0666*, no. 2006-01-0666, 2006.
- [40] R. Staunton, C. Ayers, L. Marlino, J. Chiasson, and T. Burrell, “Evaluation of 2004 Toyota Prius Hybrid Electric Drive System,” Oak Ridge National Laboratory, ORNL/TM-2006/423, May 2006.